Single-cell time course analysis of metabolic switching in inducible gene regulatory networks

Sonja Westermayer

München 2016

Single-cell time course analysis of metabolic switching in inducible gene regulatory networks

Sonja Westermayer

Dissertation
an der Fakultät für Physik
der Ludwig–Maximilians–Universität
München

vorgelegt von
Sonja Westermayer
aus München

München, den 25. Mai 2016

Erstgutachter: Prof. Dr. Joachim Rädler
Zweitgutachter: Prof. Dr. Ulrich Gerland
Tag der mündlichen Prüfung: 11. Juli 2016

Contents

Zusammenfassung

Die Optimierung der Zuckerverwertung ist für Bakterien insbesondere unter variablen Umweltbedingungen essentieller Teil ihrer Überlebensstrategien. Bei zwei konkurrierenden und fluktuierenden Nahrungsangeboten stellt sich die Frage, ob eine homogene oder heterogene Anpassung optimal ist. Um solche Anpassungsmechanismen zu verstehen, wurde metabolisches Schaltverhalten anhand von Genexpression mit Hilfe von Reportergenen sowie zeitaufgelöster Fluoreszenz-Mikroskopie auf Einzelzellebene in *Escherichia coli* untersucht. Da Genexpression ein inhärent stochastischer Prozess ist, können ausgeprägte Unterschiede zwischen einzelnen Zellen auftreten. Diese Expressionsunterschiede können Teil komplexer Überlebensstrategien sein. In dieser Arbeit wird das Schaltverhalten in Antwort auf eine Nährstoffänderung in direkter bakterieller Umgebung sowie das Umschalten zwischen verschiedenen Verwertungsstrategien als Reaktion auf die Zugabe zweier unterschiedlicher Nährstoffe in verschiedenen Konzentrationen analysiert.

Im ersten Teil dieser Arbeit wird das Schaltverhalten im Arabinose-Verwertungssystem untersucht. Hier wurde gezeigt, dass das Abschalten der Genexpression nach Entfernen der induzierend wirkenden Arabinose in allen Zellen innerhalb kurzer Zeit, also homogen abläuft, im Gegensatz zum heterogenen Anschalten. Da die Genexpression in induzierbaren Zuckerverwertungssystemen stark vom Wert der intrazellulären Konzentration des induzierenden Zuckers abhängt, muss zum Abschalten der Genexpression dieser Konzentrationswert unter das zur Induktion nötige Niveau sinken. Ein Absinken der internen Zuckerkonzentration kann entweder über Abbau oder Export des Zuckers geschehen. Innerhalb der hier möglichen Zeitauflösung wurde mit Hilfe einer Mutante, der das Abbauenzymgen *araBAD* fehlt, keine Abhängigkeit des zeitlichen Abschaltverhaltens von diesem Enzym gefunden. Zusätzlich ist das Abschalten unabhängig von der Expression eines potenziellen Exportproteins des Arabinosesystems. Daher ist möglicherweise ein bisher unbekannter nicht-kanonischer Abbau- oder Exportweg für das schnelle und homogene Abschalten der Genexpression verantwortlich.

Der zweite Teil dieser Arbeit beschäftigt sich mit dem Schaltverhalten im Phosphotransferase System, das die Aufnahme zahlreicher Zucker an die Verfügbarkeit von Phosphorgruppen innerhalb der Zelle koppelt. Erstmals wurden quantitative Messungen zum Schaltverhalten des PTS für zwei ausgewählte Zuckerverwertungssysteme, N-acetyl-glucosamine (NAG) und Sorbitol, durchgeführt. Der konkurrierende Prozess um die importlimitierende Ressource Phosphor wurde durch Messung der Genexpression der Systeme

sowie durch den konzentrationsabhängigen Einfluss der Zucker auf die Wachstumsrate analysiert. Abhängig von der externen NAG Konzentration zeigten sich zwei Verhaltensweisen: Hohe NAG Konzentrationen führen zu hierarchischem Verwerten der Zucker in Übereinstimmung mit theoretischen Vorhersagen, bei niedrigen Konzentrationen hingegen werden die metabolischen Gene beider Systeme simultan angeschaltet. Mit Hilfe eines mathematischen Modells, das asymmetrische Zuckerqualität sowie variable Kopplung implementiert, kann das gemessene Phasendiagramm der Genexpression reproduziert werden. Daher ist es plausibel, dass die simultane Expression der beiden Systeme unter Bedingungen eines nicht-limitierenden Phosphorflusses von einer Entkopplung der Zuckerverwertungssysteme rührt.
Die Tatsache, dass die Zellen für das PTS zwei Schaltverhalten kennen, weist auf eine effiziente Regulation mittels Beschränkung des Phosphorflusses hin und könnte insbesondere bei der Anpassung der metabolischen Überlebensstrategie einer Zelle an vorherrschende Umweltbedingungen ebenso von Nutzen sein wie ein schnelles Abschalten der Genexpression nach Entfernen der externen Arabinose.

Summary

Bacteria essentially need to optimize their strategies for survival under fluctuating environmental conditions. One possible strategy is adaptation, but it is unclear if homogeneous or heterogeneous adaptation is optimal in the presence of two fluctuating substrates, which are competing for basic resources in the cell. To elucidate such adaptation mechanisms, metabolic switching of *Escherichia coli* on the single-cell level was studied by means of reporter genes and fluorescent time-lapse microscopy. Due to the inherent stochasticity of gene expression processes, significant cell-to-cell variation occurs, which can be part of complex survival strategies. In this work, metabolic switching triggered by a change of nutrient in the environment as well as switching between different metabolic strategies is studied in response to several concentrations of two nutrients provided at the same time.

The first part of this work investigates metabolic switching in the arabinose utilization system. In the course of this work, the OFF-switching of gene expression was found to be homogeneous and fast in all cells after removal of external arabinose, in contrast to the heterogeneous ON-switching. In inducible utilization systems, gene expression largely depends on the intracellular concentration of the inducing substrate. For a transition of the induced ON state to the uninduced OFF state, this internal concentration needs to drop under the threshold level of induction. Decrease can be achieved either by degradation or by export. Within the time resolution of this work, the transition was found to be independent of the canonical pathway of arabinose degradation as probed with a mutant lacking *araBAD*, which is the gene encoding the catabolic protein of the arabinose utilization system. Apparently, the OFF-switching of the arabinose system is also independent of the expression of a potential export protein of the arabinose system. Thus, some non-canonical metabolic pathways or modes of arabinose export might underlie the fast and homogeneous transition into the uninduced state after a downshift of the external arabinose concentration.

The second part explores the Phosphotransferase System (PTS), a global sugar utilization system governing the import and metabolism of various sugars in dependence of the availability of phosphor groups within a cell. For the first time, competition of two sugar utilization systems part of the PTS, the N-acetyl-glucosamine (NAG) and the sorbitol system, has now been analyzed by measuring gene expression of these systems and the concomitant impact of sugar utilization on growth rates. Two distinct regimes of sugar utilization were found: one of hierarchical usage of the carbohydrates at high NAG con-

centrations in accordance with theoretical predictions, and one of co-expression of the metabolic genes at low NAG concentrations. Computational simulations of a mathematical model incorporating asymmetric sugar quality reproduced this metabolic phase diagram, suggesting that under conditions of non-limiting phosphate flux, co-expression is due to uncoupling of the two sugar utilization systems.
Hence, the fact that the cells exhibit two different metabolic switching behaviors for the PTS indicates that flux-limitation in the PTS could serve as an efficient way of regulation to adapt the cells' metabolic strategy to prevailing environmental conditions just as fast OFF-switching of gene expression after depletion of external arabinose.

1. Introduction

Numerous sectors of our everyday life are highly influenced by the use of genetically modified microorganisms. For example, microbes are used as "cell factories" to produce pharmaceutics such as antibiotics or insulin, food supplements, plastics, and biofuels. Likewise, they are a useful tool for bioremediation to clean waste water or toxic soils. Recently, the discovery of a bacterium which is able to degrade polyethylene terephtalate (PET), a widely used plastic which has accumulated within the environment all over the globe, even promises solutions for biological recycling and environmental remediation of PET waste products [1].

However, the efficiency of all these applications highly depends on the content of the primary biomass. If the biomass contains several different nutrients, regulation processes in microorganisms, which for example prioritize the usage of carbon sources, often result in a conflict of interest between optimal physiology for survival of the microorganism and economic viability in terms of maximal generation of the desired product [2]. Thus, the understanding of the fundamental working principles of cells is a prerequisite for designing desired properties in microorganisms and for manipulating existing processes in order to optimize the efficiency of their applications.

Systems biology devises mathematical models and uses quantitative data on molecular interactions in order to derive design principles of a system and to make predictions of a system's behavior [3]. Then based on the system-level understanding, strategies can be determined to modify and construct biological systems with desired features.
In this context, it is essential to understand bacterial strategies for growth and survival, especially under fluctuating environmental conditions. Adaptation, which is one major strategy, needs extracellular signals to trigger intracellular responses such as the up- or down-regulation of specific genes. This signal transduction is often subject to complex regulatory networks in which frequently occurring patterns, so called motifs, have been identified. One common motif is positive autoregulation, the stimulated expression of a gene by its own gene product, which can implement a switch-like behavior by enhancing fluctuations in the protein production rate [4, 5]. Such fluctuations are ubiquitous in gene regulatory networks. Here, stochasticity plays a major role due to the low numbers in which many molecules are present in a cell [6]. The high impact of stochasticity on the behavior of cells is visible in significant cell-to-cell variations: Genetically identical cells within one population have been found in completely different physiological states [7].

For a long time this stochasticity, generally called noise, was considered as an unavoidable disturbance, but lately, stochasticity has been recognized as part of a regulatory strategy [7]. In a purely deterministic world without any noise, all cells in an isogenetic population would be in the exactly same state and would just be identical in their reaction to external triggers. But the cells' environment is not purely deterministic, in contrast unpredictable fluctuations are likely to occur. Hence, it would be highly favorable for a population to spread their possibilities of reactions and thus their risk of getting extinct. Then, by producing a distribution of states in a population, the inherent stochasticity increases the chance of survival of the population, especially in changing environments [7, 8, 9].
The development of tools for single-cell analysis, such as flow cytometry or time-lapse microscopy in combination with techniques of bio-compatible immobilization of single cells, facilitated the analysis of heterogeneity within cellular populations. In addition, studies of gene expression *in vivo* have highly benefited from the discovery of fluorescent proteins [10]. The genes encoding fluorescent proteins are frequently used as reporter genes and can be introduced into microorganisms under the control of a transcriptional regulatory network. Then, insight into the expression of other genes under the same transcriptional regulatory network can be gained indirectly by following the fluorescence signal of individual cells over time.

During the past decades, many fundamental questions concerning gene regulation have been addressed, such as the role of noise and the generation of bi-stability in steady-state for various sugar utilization systems [7, 11]. Heterogeneous timing in the switching from the uninduced OFF to the induced ON state has been studied for the arabinose utilization system, which is the model system of positive autoregulation in *Escherichia coli* (*E. coli*) [12]. However, while the dynamics of the induction process has been studied in detail for the arabinose utilization system, the dynamics of the switching from the ON state back into the OFF state has not yet been analyzed. Certainly, this process is equally crucial to understand the strategy of adaptation of a cellular population in reaction to fluctuations of nutrients in the environment and will be studied in this work.

In recent years, a novel strategy of metabolic regulation via the sensing of metabolic fluxes was proposed, contrary to the sensing of metabolic concentrations [13, 14]. It was argued that a cell could minimize expenses for the sensing of concentrations of individual carbon sources and for the regulation of the involved enzymes by responding to the general, glycolytic flux [15]. For systems which compete for a limited flux inside the cell, existing theoretical work predicts a winner-take-all outcome of metabolic switching [16]. So far, experimental data on this prediction is missing. Likewise, the switching of utilization strategies especially in pluri-nutrient environments is not well studied to date.

In this thesis, bacterial regulation of sugar utilization systems is analyzed at the single-cell level in response to switches of sugar concentrations in the environment. After an intro-

duction of basic concepts such as gene regulation, fluorescence and mixed substrate growth in Chapter 2, fundamental experimental methods as well as technical advancements are presented in Chapter 3. Chapter 4 examines the kinetics of phenotypic switching of the arabinose utilization system from the induced into the uninduced state in single *E. coli* cells. Theoretical predictions of metabolic switching behavior under flux-limited competition are probed experimentally for two sugar utilization systems, part of the Phosphotransferase System (PTS), by analyzing growth and gene expression in response to different concentrations of external inducer (see Chapter 6). Then, a theoretical model is introduced which reproduces the experimental data and predicts that the switching between the observed strategies of hierarchical winner-take-all and stochastic co-expression behavior depends on the available phosphate flux. Maturation times of the two fluorescent reporters, mVenus and mCerulean, used for this study are characterized and discussed in Chapter 5.

2. Basic concepts

This Chapter gives basic information on gene expression, gene regulation and noise in gene expression. Furthermore, modes of sugar utilization in mixtures are discussed and the green fluorescent protein is introduced.

2.1. Gene expression in the model system E. coli

The prokaryote *E. coli* is one of the most frequently used model systems for gram-negative proteobacteria in scientific work. The rod-sized bacteria are about one µm wide and about five µm long. Storage at −80 °C is possible for over ten years. Due to their natural habitat of mammalian intestines, they are cultivated best at a temperature of 37 °C [17].

The cell wall of *E. coli* consists of several layers, starting with lipopolysaccharides covering the outer membrane, which is separated from the inner, phospholipid-composed membrane by the intermediate periplasmic layer, which contains mainly peptidoglycans besides different proteins, see Fig. 2.1A [18]. This structure and especially the outer layer allows the fixation of *E. coli* to surfaces covered with the cationic polymer poly-L-lysine (PLL). Although this method is widely used, it also has some constraints. Some studies investigated the effects of PLL on attached bacteria and found non-negligible effects on bacterial physiology as for example on the cell wall [19, 20].
Genetic information in *E. coli* cells is stored on the chromosome and additionally on plasmids, which are small double-stranded deoxyribonucleic acid (DNA) loops, see Fig. 2.1B. Via the inclusion of antibiotic resistance genes in addition to further mutations, selection for bacteria carrying the resistance is possible and allows to study effects of the mutations of interest. The genetic code is translated into proteins in the process of gene expression in several steps following the "central dogma of molecular biology" [21] (see Fig. 2.1C): First, polymerases transcribe the DNA into messenger ribonucleic acid (mRNA). Second, this mRNA is translated into a linear chain of amino acids by ribosomes. While being constructed, the linear chain already begins to fold into its characteristic three-dimensional structure. Sometimes, the correctly folded protein, the so-called native protein, still is not fully functional but requires final maturation processes such as cyclization or oxidation steps [22, 23].

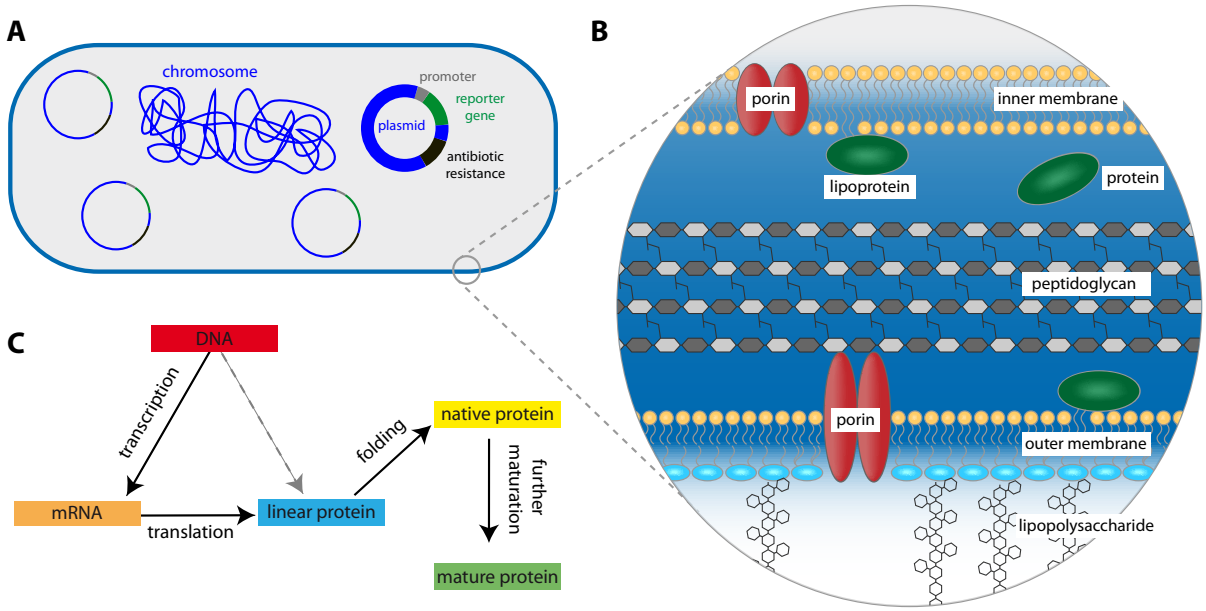

Figure 2.1.: Schematic representation of a cell, of the cell wall and of the steps in gene expression.
A) Genetic information of a cell is stored on the chromosome and on plasmids. Plasmids are often used to integrate specific genes such as genes encoding for reporters or for antibiotic resistances into cells. **B)** The cell wall of a gram-negative bacterium such as *E.coli* consists of an outer membrane coated with lipopolysaccharides and an inner membrane. The periplasmatic space in between both membranes contains a peptidoglycan layer as well as membrane-bound or freely diffusing proteins. Porins in both layers passively or actively transport substrates in or out of the cell. **C)** Gene expression follows the "central dogma of molecular biology" where DNA is transcribed into mRNA which is translated into protein, sometimes followed by further steps of maturation.

2.2. Fluorescent proteins

The discovery of fluorescent proteins revolutionized the observation of gene expression processes *in vivo*. Luminescence of the green fluorescent protein (GFP), naturally occurring in the jellyfish *Aequorea victoria*, originates from its molecular structure: A chromophore is embedded in a β-barrel with an α-helix along its axis (see Fig. 2.2) [10, 24, 25].
Until now, variable mutants have been engineered, whose different excitation and emission wavelengths cover the visible spectrum [26]. They are widely used as tracers when attached to a target of interest or as reporters for gene expression: A gene encoding for one of these fluorescent proteins is put under the control of the desired promoter and is integrated in the genome. Then, all transcription factors which affect the original gene will affect the reporter gene in the same way. Thus, if the gene under this chosen promoter is expressed, the fluorescent protein is expressed in parallel. By following the level of fluorescence, information on the expression level of the gene of interest can be gained. The reporter gene can be integrated directly in the chromosome or via plasmids (see Fig. 2.1A).

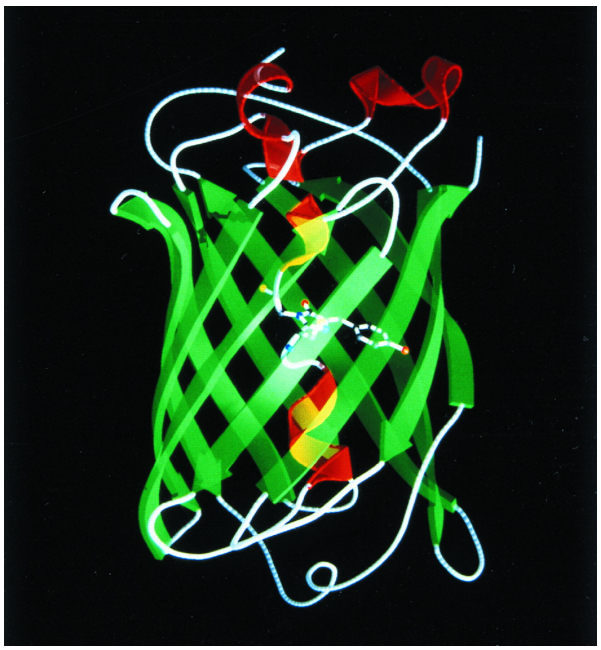

Figure 2.2.: Molecular structure of the green fluorescent protein.
Eleven β-strands form a barrel with an α-helix running along its axis. The chromophore, responsible for fluorescence, is located in the well protected center of the barrel. Figure taken from [25], ©1997 by National Academy of Sciences.

The later method produces higher fluorescence signals when high copy number plasmids are used but at the same time it produces a greater cell-to-cell variability. This variability is unwanted in most cases, especially when the inherent heterogeneity of a population is of interest. As most fluorescent proteins are non-toxic, their presence in low amounts usually does not harm the cell. But of course, the production of additional proteins is energy and resource consuming and has its impact on the whole cellular system. Often, this impact is negligible but it should be kept in mind.

Like all proteins, fluorescent proteins are expressed according to the pattern illustrated in Fig. 2.1C with the particularity that the fully folded proteins need additional steps of maturation. For GFP, the rate limiting step of maturation was reported to be an oxidation, which can take more than an hour in wild type GFP [22]. As real-time observation of processes on a faster time-scale needs shorter maturation times, mutants have been developed for technical use. These mutants are characterized by much shorter maturation times and also by excitation maxima at longer wavelengths than the wild type (395 nm) (see Fig. 2.3 for the spectra of several GFP mutants). So, detrimental effects of fluorescence illumination are reduced, which are in general more pronounced for higher energetic wavelengths. One detrimental effect originates in photobleaching, which is the permanent loss of fluorescence of a fluorescent protein after a number of excitation-deexcitation cycles. Then, free radicals can be released, which might have toxic effects *in vivo*. Photobleaching

depends among others on the specific mutant of the fluorophore and on external conditions and can be reduced by adequate experimental conditions [27, 28, 29].

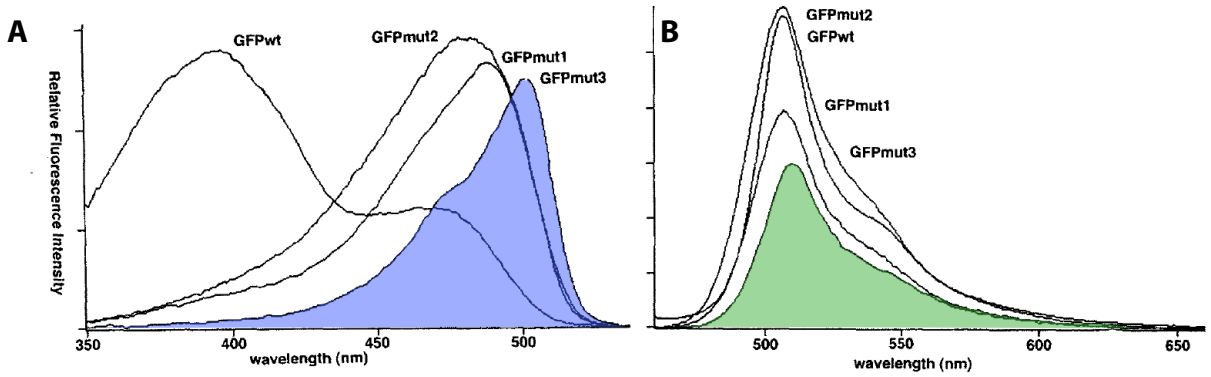

Figure 2.3.: Excitation A) and emission spectra B) of several GFP mutants. In this work, the mutant GFPmut3, which is highlighted, is employed. The emission maximum of this mutant is found at considerably longer wavelengths than that of the wild type (GFPwt). Figure adapted from [30] with permission from Elsevier.

For this work, three fluorescent proteins have been employed. The GFP mutant GFPmut3 was used to study the arabinose utilization system. This fluorescent protein has a maturation time of $\tau_m = 6.5\,\text{min}$ [12] and shows maxima of excitation and emission at 501 nm and 511 nm, respectively, see Fig. 2.3. A yellow fluorescent mutant, which is called mVenus due to its brightness, shows excitation and emission spectra with maxima at 515 nm and 528 nm, respectively, see Fig. 2.4 [31]. In the cyan regime, the mutant mCerulean, characterized by optimized quantum yield, was chosen, which shows excitation and emission spectra with maxima at 433 nm and 475 nm, respectively, see Fig. 2.4 [32]. The maturation times of mVenus and mCerulean *in vivo* have been measured within this study (see Chapter 5). Due to their spectra, the two fluorescent proteins mVenus and mCerulean are well suited to be used together. In this work, both were used to study the PTS.

2.3. Mixed substrate growth

Pure single sugar environments of common experimental conditions are rather artificial. As complex mixtures of carbon sources often appear in natural environments, strategies for growth and survival under these conditions are essential for bacteria. Thus, microorganisms have evolved to survive under conditions of mixed carbon sources. How a mixture of substrates is metabolized exactly depends on many factors, such as on the specific organism, on the distinct carbon sources, and on their concentrations [34, 35, 36]. In general, two different utilization strategies can be distinguished: a strategy of hierarchical utilization of the available energy sources and a strategy of simultaneous utilization. Both strategies will be discussed in detail in the following.

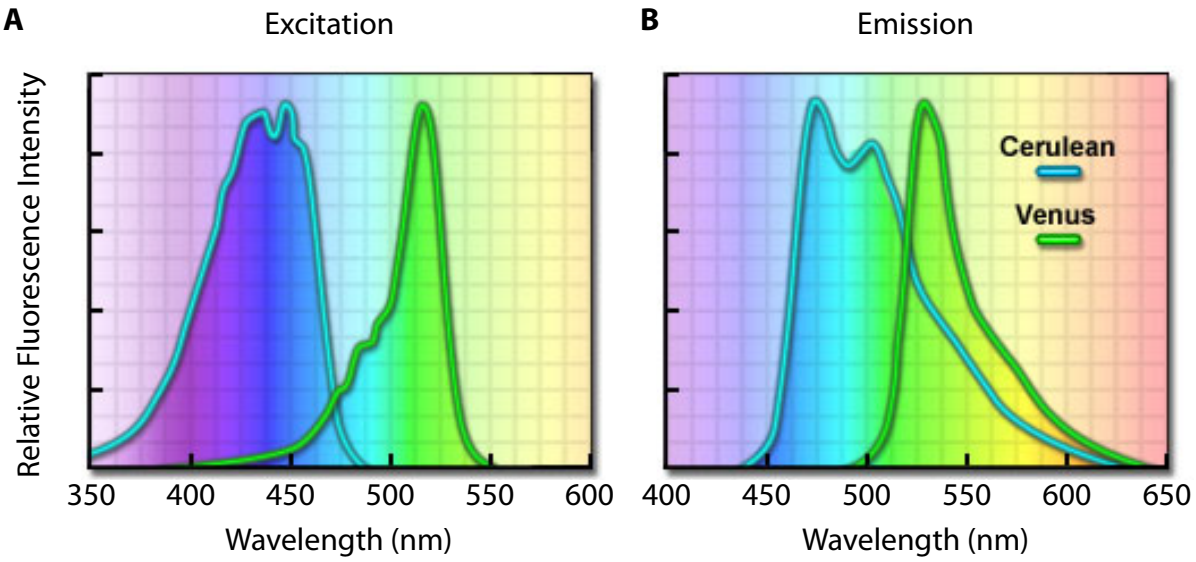

Figure 2.4.: Excitation A) and emission spectra B) of Venus and Cerulean. Both mutants have been used together in this work due to their compatibility with each other. When appropriate filter sets are chosen, crosstalk can be avoided. Figure taken from [33] is reprinted with permission from Nikon, Inc.

2.3.1. Simultaneous utilization

Recently, the case of co-utilization was characterized in *E. coli* by a growth-rate composition law that was experimentally verified for several pairs of co-utilized carbon sources [37]. Depending on their entry into the glycolysis pathway, carbon substrates were divided into upper and lower substrates and a combination of an upper with a lower substrate, such as glucose with pyruvate, in millimolar concentrations resulted in co-utilization with a growth rate, which was higher than the ones for each of the substrates alone [37].
Especially, in the natural environment of aqueous microorganisms, mixtures of nutrients occur where each single nutrient is present only in low concentrations. In these ecosystems, simultaneous utilization is thought to be the rule rather than the exception [38]. This oligotrophic behavior can explain the relatively high growth which is observed in these nutrient-poor environments [38].

2.3.2. Hierarchical utilization

Already in 1940, Jacques Monod studied bacterial growth in mixtures of carbon sources. His pioneering studies led to great progress in the understanding of sequential usage of distinct carbon sources [39].
J. Monod studied the growth of *E. coli* in the presence of several pairs of carbohydrates as for example of glucose and fructose or of glucose and arabinose (see Fig. 2.5). By recording optical density over time, he recognized two types of growth curves, smooth ones

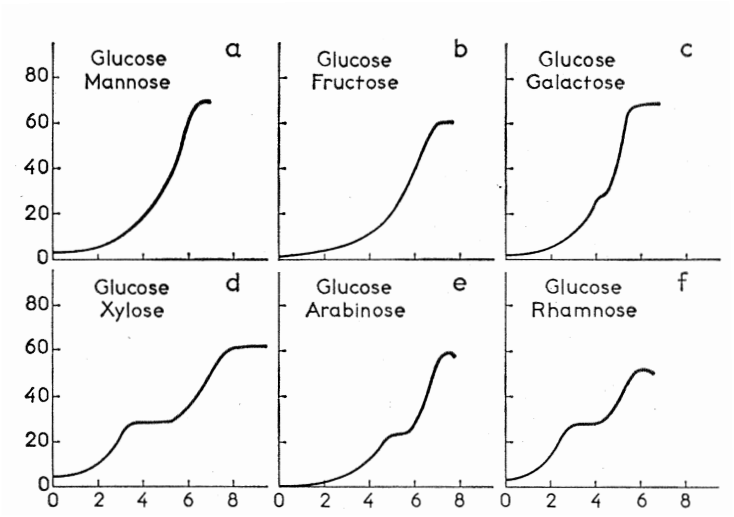

Figure 2.5.: Growth curves on different pairs of sugars.
When *E. coli* was grown in the presence of two carbon sources, J. Monod discovered differences in the form of the growth curves. Some growth curves, which he called normal, were smooth while others, which he called diauxic, showed step-like forms with various step sizes. Image source: [40].

which he associated with "normal" growth (glucose with fructose in Fig. 2.5b) and curves showing a step-like form (glucose with arabinose in Fig. 2.5e). These second ones with the sometimes more, sometimes less pronounced plateau of growth arrest were associated with "diauxic" growth. Among other things, Monod grew *E. coli* in mixtures of glucose and sorbitol of various concentrations to elucidate the process of diauxic growth. By recording the culture's optical density, he found a correlation between glucose concentration and total growth during the first growth cycle up to the plateau [39]. By studying diauxie in combination with the lactose system, regulation by allosteric transitions was discovered [41]. Monod also recognized that the process of diauxie was closely related to the "glucose effect", which has already been discovered in yeast in 1900 by Frédéric Dienert [41, 42]. It was found that such hierarchical effects require a mechanism of suppression of the expression or the activity of sugar-specific catabolic enzymes, later called carbon catabolite repression (CCR) [35, 43].

2.4. Molecular mechanisms of gene regulation

Monod's studies on the *lac* operon mark the beginning of endless discoveries in the field of gene regulation, especially on the level of transcription factors. But also functional roles of noise have been studied in detail [7].

2.4.1. Transcription factors

Gene expression is highly controlled by an interplay of transcription factors and signaling molecules. By their presence on operator sites, transcription factors such as activators and inhibitors facilitate or hinder the binding of the RNA-polymerase to the promoter and thus increase or reduce the transcription rate. In turn, binding affinity of the activator or inhibitor itself is often modulated by messenger molecules, such as specific metabolites, or by second messengers, such as cyclic adenosine monophosphate (cAMP). Thus, the production of a protein is commonly controlled by a whole transcription network [44]. Within such regulatory networks, certain patterns can be identified, which occur frequently and most probably guarantee some selective advantage [4]. Such a pattern is autoregulation, which is the regulation of its own gene by a regulator, with the potential to produce a direct feedback loop. When it is negative, autoregulation has the ability to speed up the response time of gene circuits [4]. Gene regulation networks can be modeled by ordinary differential equations within thermodynamic models in order to make quantitative predictions [45]. However, even the prediction of qualitative features of a gene regulation network often requires the input of quantitative observations of the transcriptional regulation of key genes [46].

2.4.2. Noise in gene expression

Although gene expression is highly controlled by all these transcription factors, it is inherently noisy. Biochemical reactions are subject to the binding probabilities of the interacting components. For example, a transcription factor which inhibits by its presence on the DNA the binding of the polymerase still has a certain probability to unbind the DNA, even in the absence of any ligand, which induces unbinding. Such an event gives rise to a short burst of mRNA production, which is followed by multiple translation of each mRNA molecule. Hence, production of proteins is not a uniform process but rather occurs in stochastic bursts every time the promoter is in the ON state (see Fig. 2.6A) [47, 48]. Then, a stochastic model for the expression of a single gene predicts the noise strength for a protein expression level p with its mean $< p >$ and standard deviation σ_p to be

$$\frac{\sigma_p^2}{< p >} = 1 + b \tag{2.1}$$

and thus to be only dependent on the burst size b, which is defined as the average number of proteins which are synthesized per mRNA [47]. As the lifetime of a protein is in general longer than the lifetime of an mRNA, the bursts of expression are time-averaged [7]. Thus, the variability caused by bursts of mRNA is only partly propagated to the protein concentration.

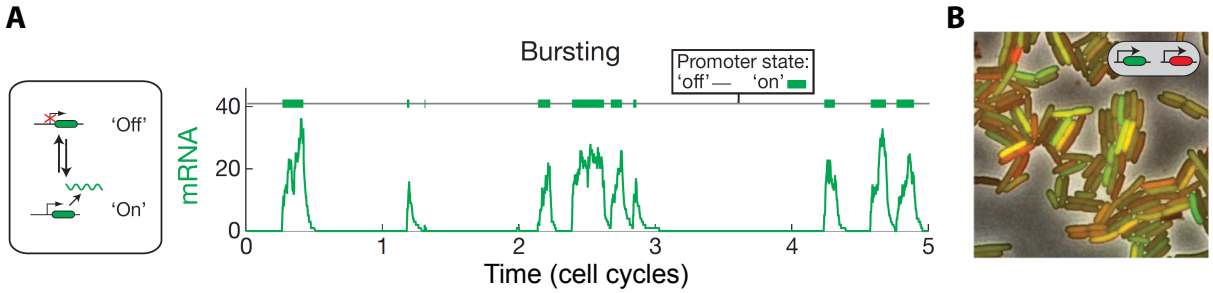

Figure 2.6.: Stochasticity in gene expression.
A) Noise raises from bursting of gene expression: When the promoter is in the ON state, many mRNA molecules are produced in one burst. **B)** Gene expression in *E. coli* is shown for two identical promoters driving two different fluorescent protein (shown in green and red). Due to noise, the ratio of green and red differs from cell to cell. Figure taken from [7] is reprinted with permission from Macmillan Publishers Ltd.

Due to this intrinsic noise, even absolutely identical cells with respect to their genes and to the concentration or the state of their components can display different phenotypes [48]. This effect can be further enhanced by fluctuations in concentration or state of cellular components, called extrinsic noise [48]. Fig. 2.6B illustrates the effect of noise in a population of *E. coli* cells. Here, the genes of two different fluorescent proteins are integrated behind two copies of the same promoter. Without noise, all cells would show the same color as a consequence of identical ratio of both fluorescent proteins. But due to noise, this ratio varies from cell to cell and is distributed over the population [7]. Feedback systems such as negative autoregulation can reduce noise to some extent, positive feedback systems act in a noise-enhancing way and can even cause bimodality [4, 49].
For a long time, noise was thought to be parasitic in general. But nowadays, stochasticity in gene regulation is even understood to be exploited by cells as a strategy of adaptation in the presence of environmental changes [9]. Unlike under controlled laboratory conditions, cells in a natural environment often face random fluctuations of the extracellular conditions. As even one stochastic single molecule event can trigger switching between phenotypes [50], noise gains significant importance even as a survival strategy. In sufficiently fast switching environments, the stochastic switching of bacteria between different states was predicted to be more advantageous than the sustention of an apparatus to sense the environment [51]. Experimentally, such a prediction was confirmed in yeast by using a mutant which randomly transitions between two states differing in galactose metabolism [8].
Also in combination with heterochronic gene expression in the arabinose system, the question has been discussed, whether this behavior is beneficial under fluctuating environments [12]. Therefore, it was considered that the expression of a gene costs energy before it can gain energy via the catabolism of its specific substrate. Depending on this amortization time and the duration of a pulse of nutrient, switching was predicted to be detrimental, when the total energy balance is negative [52]. Then, a distribution of response times,

which is broader than the amortization time, would minimize the risk of a population to get extinct [52]. Thus, such a mixed strategy spreads the chances of survival for the whole population.

2.5. Heterogeneous timing in the arabinose utilization system

Recently, the phenomenon of heterogeneous timing has been discovered in the arabinose utilization system of *E. coli* [12]. After having induced single cells with external arabinose, gene expression of the reporter gene gfp integrated after the P_{BAD} promoter (see Fig. 4.1) was recorded by measuring the fluorescence signal of single cells over time. Several different concentrations of external arabinose have been tested [12].

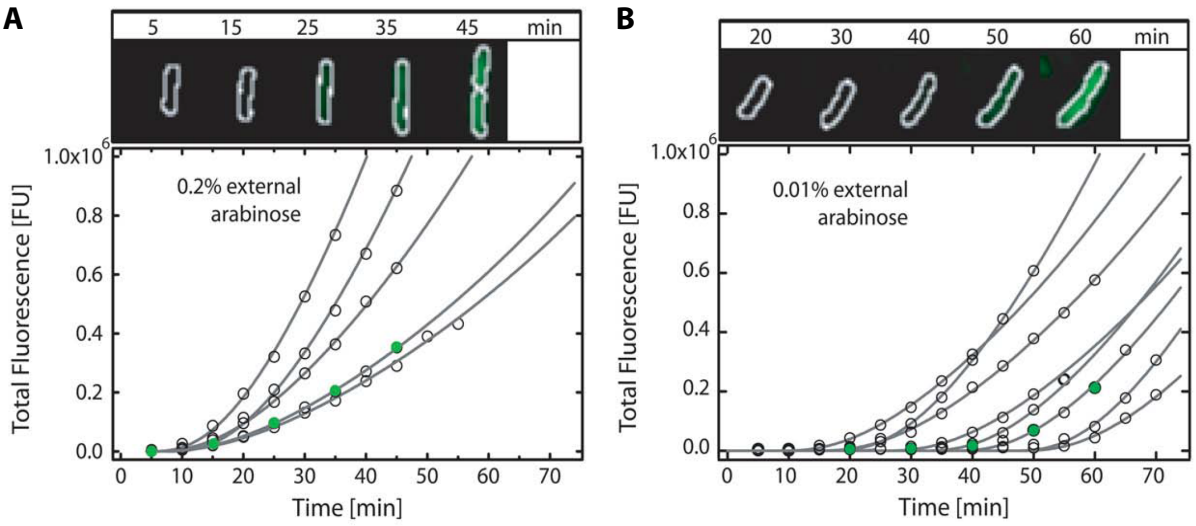

Figure 2.7.: Single-cell induction kinetics of the arabinose utilization network. Cells were induced at $t = 0$ min with **A)** 0.2% arabinose and with **B)** 0.01% arabinose (open circles). The traces were analyzed up to the first cell division, which results in different numbers of data points in the traces. Fits of the deterministic gene expression function in Eq. 2.2 to the data are shown as solid lines. The image panels in **A)** and **B)** correspond to the fluorescence traces marked with green circles, respectively. The total fluorescence was determined as described in Section 3.3. Figure taken from [12] is reprinted with permission from Elsevier.

For all concentrations, smooth and deterministic time-traces appeared after induction with arabinose [12]. Such time-traces are shown in Fig. 2.7 for induction with two concentrations of arabinose, 0.2% and 0.01%. Interestingly, the authors found a huge difference in the variation between single-cell curves with the external arabinose concentration. At the high concentration of 0.2% arabinose, almost all curves start rising after approximately 10 min with little variation between different single-cell curves. However, at the lower

concentration of 0.01% arabinose, a huge variation between the single-cell curves can be observed and was termed heterogeneous timing [12].

Stochastic mathematical description by Monte-Carlo simulations of arabinose uptake and transporter expression were used to illustrate the emergence of cell-to-cell variations in the delay time [12]. Within the model, internal arabinose accumulates approximately linearly in time until the effective arabinose threshold of $a_0^{int} \approx 50\mu M$ is reached. At this threshold, activation of the gene expression of the arabinose-dependent promoters starts. Then, arabinose accumulation accelerates due to the production of new import proteins. The time delay τ_D is the time which is required until internal arabinose concentration has reached this threshold level a_0^{int}. If a cell initially only has one import protein, the time to reach the threshold level would be given by $\tau_0 = a_0^{int}/\nu_0$, where the uptake rate per protein ν_0 depends on the concentration of external arabinose. Then, the delay time is inversely proportional to the current number of uptake proteins n, i.e. $\tau_D = \tau_0/n$ because the threshold concentration of internal arabinose is reached the earlier, the more uptake proteins are engaged in the process of import.

Based on the assumption of a step-like increase of the transcription rate of *gfp* from its basal to its maximal value after a delay time τ_D, the time-evolution of the total number of fluorescent GFP molecules in a cell, $Z(\tau)$, is given by

$$Z(\tau) = \alpha_p \left(\frac{(\gamma + \lambda_x)e^{-\tau/\tau_m}}{(\gamma + \tau_m^{-1})(\lambda_x + \tau_m^{-1})} + \frac{\tau_m^{-1} e^{-\lambda_x \tau}}{\lambda_x(\tau_m^{-1} - \lambda_x)} + \frac{\tau_m^{-1} e^{\gamma\tau}}{\gamma(\gamma + \tau_m^{-1})} \right) - Z_0 \qquad (2.2)$$

where the time $\tau = t - \tau_D$ is the time after transcription is switched on, α_p is the protein synthesis rate in fluorescence units per minute [FU/min], γ is the cell-doubling rate, τ_m^{-1} is the GFP maturation rate, and λ_x is the mRNA degradation rate [12]. Z_0 is the initial state constant. Within the model, transcription is assumed to starts when the internal arabinose concentration reaches a certain threshold. The internal arabinose concentration is modeled as a step function and causes gene expression to switch from the OFF to the ON state after the delay time τ_D. By fitting the model to single-cell experimental trajectories (solid lines in Fig. 2.7), the delay time τ_D was extracted for each cell [12].
Fig. 2.8 shows the distributions of the delay times extracted by fitting the fluorescence time series with the model Eq. 2.2 [12]. Two observations are made: The mean of these distributions shifts towards higher values for lower concentrations of external arabinose and the distributions themselves become broader. Data in Fig. 2.8 was fitted with a delay time distribution, which was derived from the steady-state distribution of the number of uptake proteins n [12]. Due to the excellent agreement of the shape of the fitted distributions with the measured data, the authors suggest that the observed variations in delay times can indeed be explained by the distribution of the number of pre-induction uptake proteins.
The lifetime of the uptake proteins is with typically 70 min much larger than the aver-

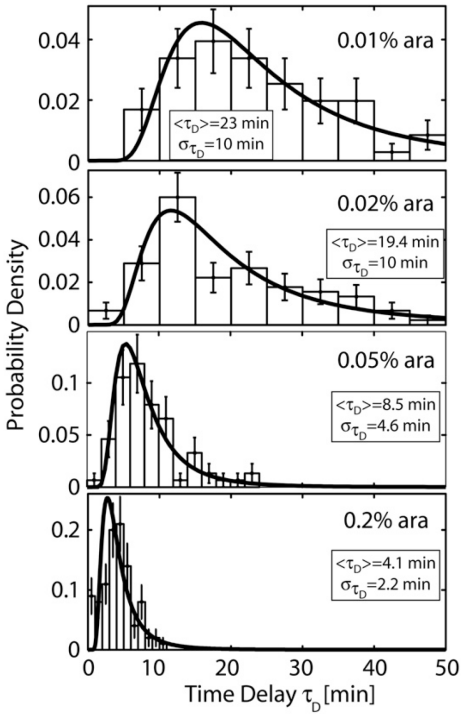

Figure 2.8.: Distributions of the delay times for various external arabinose concentrations.
Histograms of the time delay τ_D are shown for various external arabinose concentrations, as determined from the fits of Eq. 2.2 to the fluorescence time series. The mean $< \tau_D >$ as well as the standard deviation σ_{τ_D} gradually decrease for increasing arabinose levels. The distributions were fitted with an analytical delay time distribution (solid lines). Figure taken from [12] is reprinted with permission from Elsevier.

age delay times [12]. Then, the assumption of n being constant during the delay time is sufficiently accurate and the mean and variance of the delay time distribution can approximately be written as

$$< \tau_D > \approx \frac{\tau_0}{\mu b}(1 + \frac{1}{\mu}) \tag{2.3a}$$

$$\delta\tau_D^2 = (\frac{\tau_0}{\mu b})^2 \frac{1}{\mu} \tag{2.3b}$$

with the burst size b (see Eq. 2.1) and the burst frequency μ, which can be interpreted as the number of bursts within the lifetime of a protein [12].
All in all, the behavior of heterogeneous timing could be a random outcome of the evolution of the arabinose utilization system in *E. coli*, but it could also be part of a favorable strategy. In this sense, a population could spread its risk of investigating in the costly synthesis of the arabinose system in the presence of random fluctuations of arabinose in the environment. Then, a temporal distribution of the start of gene induction could provide selective advantage for the population as a whole.

2.6. Modeling gene expression

Mathematical models are the most powerful tool to understand experimental data. On the one hand, they allow for interpretation of existing experiments and help in understanding global principles underlying the studied mechanisms. On the other hand, predictions can be made for existing and even for new systems, which then can be tested via experiments again. Due to the enormous complexity of living systems, the development of models of cellular functions is challenging and various approaches exist. Very detailed models include every known molecular and biochemical detail of a process, while very abstract models simplify processes and for example describe gene regulation as a two-state system [53, 54]. Some approaches are purely deterministic, but others include a certain degree of stochasticity.
In general, the time evolution of biochemical reactions is modeled by rate equations of the form

$$\frac{dX}{dt} = \nu - \lambda \cdot X, \tag{2.4}$$

which connect mean particle numbers X with reaction rates such as transcription rate ν and degradation rate λ

Hill models*
Gene regulation mediated by transcription factors can be modeled via ligand-receptor binding. When the receptor can simultaneously bind multiple ligands, and binding of one ligand enhances the affinity for further binding, switch-like behavior can emerge. Especially for all-or-nothing responses, where it is important to be either ON or OFF, a switch-like binding curve would be preferable. One example of such a process without any in-between state is apoptosis: The cell either receives signals to stay alive or to die.
Let's assume that binding and unbinding of n transcription factors TF to promoter sites Pr follows the chemical reaction

$$Pr + n \cdot TF \leftrightarrow PrTF. \tag{2.5}$$

Then, using the dissociation constant K from the law of mass action

$$K^n = \frac{[TF]^n[Pr]}{[PrTF]}, \tag{2.6}$$

the probability that the promoter will have bound transcription factor develops as

$$p_{bound} = \frac{[PrTF]}{[Pr] + [PrTF]} = \frac{[TF]^n}{K^n + [TF]^n} \tag{2.7}$$

and results in the Hill equation with Hill coefficient n. This curve gets steeper with higher values of n, which can be assigned to the cooperativity of the binding. Thus, switch-like

*See the textbook [55] for a more detailed derivation.

behavior can emerge from cooperative binding. The induction of gene expression by the binding of transcription factors to the promoter site can be one way of implementing a switch-like behavior.

Michaelis-Menten theory *

For the description of enzymatic reactions, Michaelis-Menten kinetics is the classical tool. The basic idea in the Michaelis-Menten theory is that the reaction of product formation by enzymes is separable into two steps. First, an intermediate complex of enzyme E and substrate S is formed reversibly with the forward rate constant k_+ and the backward rate constant k_-. Second, the product P is formed from this intermediate complex ES in an irreversible reaction with rate constant r. From this reaction

$$E + S \underset{k_-}{\overset{k_+}{\rightleftharpoons}} ES \xrightarrow{r} S + P \tag{2.8}$$

rate equations for every component can be derived. Under the assumption that the concentration of the intermediate complex is in steady-state, $d[ES]/dt = 0$, a new constant K_M can be introduced

$$\frac{[E][S]}{[ES]} = \frac{k_- + r}{k_+} = K_M. \tag{2.9}$$

When all enzymes are bound to substrate, the maximum rate of reaction can be written as $V_{max} = r[E_{tot}]$ with the total concentration of enzymes $[E_{tot}] = [E] + [ES]$. Then, the rate of product formation derives as

$$\frac{d[P]}{dt} = r \cdot [ES] = V_{max} \frac{[S]}{K_M + [S]} \tag{2.10}$$

which is generally referred to as Michaelis-Menten kinetics. Within this simplifying Michaelis-Menten framework, each enzyme can be characterized by two parameters, the maximum turnover rate V_{max} and the substrate concentration K_M, which is required to operate at half its maximal rate.

2.7. Flux-limited regulation

The common view of gene regulation is based on the sensing of concentrations, either by the binding of extracellular substrates to membrane-bound ligands or by the binding of intracellular substrates to membrane-bound or freely diffusing receptors. Information on these concentrations will then be transferred towards the regulatory machinery to activate a response [56, 57]. Instead of concentrations, a cell can also sense metabolic fluxes and transfer these flux-signals to the regulatory machinery. Recently, a flux-sensor was

*See the textbook [55] for a more detailed derivation.

experimentally described in *E. coli*, which is able to measure the glycolytic flux in the cell and initiate regulatory processes [15]. Similarly, a flux-sensor was described, which is involved in the regulation of antibiotic resistance in *Bacillus subtilis* (*B. subtilis*) [58]. Here, the flux-sensing mechanism couples the regulation of transporter production with the detection of transporter activity, which represents the cell's current capacity to export the detrimental antibiotic. This produce-to-demand strategy is proposed to be a cost-efficient way of gene regulation, because it can precisely be adjusted to the cell's current needs [58].

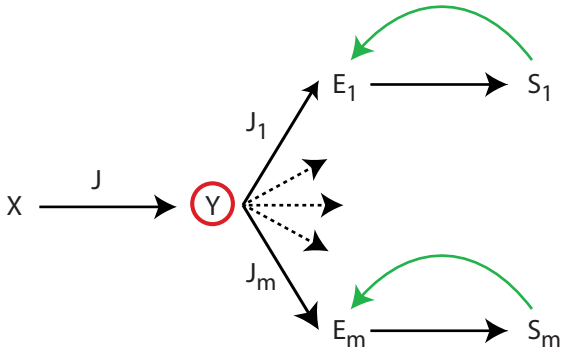

Figure 2.9.: Model of regulation by flux-limitation.
A general flux J coming from component X branches into specific fluxes at component Y (red circle). Via each specific flux J_i, $i \in \{1, ..., m\}$, component E_i is enabled to augment substrate S_i, for example by active import. By the positive feedback (green arrow) of S_i on E_i, the demand of J_i will be enhanced which negatively influences all other specific fluxes. Figure adapted from [16] with permission from Elsevier.

Furthermore, regulation via fluxes was proposed as a powerful way of controlling many systems in parallel. Instead of using numerous one-to-one interactions with specific regulatory enzymes, transcription factors and regulatory mechanisms, one global flux could control the activity of several different systems following the principle depicted in Fig. 2.9 [16]. Here, a flux J of an essential intracellular component divides into several smaller fluxes J_i ($i \in \{1, ..., m\}$) at a certain branching point Y. The target enzyme E_i of flux J_i can, when reached by J_i, import substrate S_i, which positively influences the amount of E_i. If the total flux J is limited, this positive feedback can lead to the dominance of J_i and in turn to the extinction of all other J_j, $j \in \{1, ..., m\}$, $j \neq i$. Thus, a winner-take-all type network is created by local enhancement of E_i in combination with global attenuation of E_j, $j \in \{1, ..., m\}, j \neq i$ [16].

3. Experimental methods

The following Chapter provides information on the techniques used in this work. Observation of bacteria in microfluidic environments was done by time-lapse fluorescence microscopy. Furthermore, analysis of bright field and fluorescence images is explained and technical development for fixation of bacteria on a surface is reported.

3.1. Time-lapse fluorescence microscopy

Resolution of the microscopical observation by a classic light source is limited by the diffraction limit to about 0.2 µm, approximated by Ernst Abbe more than 100 years ago. Within this resolution limit, light microscopy is based on the contrast between signal and background. Various techniques have been developed to maximize the ratio of signal to noise. An appropriate technique for the observation of *E. coli* is phase-contrast microscopy, which was invented by Frits Zernike in the early 1930s. When scattered by a specimen, the phase of light usually is shifted. In phase-contrast microscopy, this shift is converted into changes in brightness, and thus becomes visible. If the observed specimen is fluorescent, the contrast between signal and noise can become very pronounced as well [59].
The experimental setup used in this work is a fully automated inverted microscope (Axiovert 200M, Zeiss, Oberkochen, Germany) with a motorized stage (Prior Scientific, Cambridge, UK). Fig. 3.1 shows the schematic setup with two different ways of how to illuminate the sample: bright field or fluorescence illumination. As *E.coli* grows best at 37 °C, the whole setup is constantly tempered at 37 °C. Due to the structure of the inverse microscope, light from a halogen lamp (HAL 100W with mercury vapor short arc lamp HBO 103 W/2) for bright field illumination first passes through an orange filter to minimize photodamage caused by high energetic wavelengths, then passes through the condenser and a phase ring until it reaches the sample. Afterward, it is collected by the oil-immersion 100x phase-contrast objective (NA 1.3, PH3, Zeiss, Oberkochen, Germany) and is guided into a highly sensitive CCD camera (iXon DV885, Andor, Belfast, UK). In epifluorescence illumination, light (X-cite120 light source, EXFO, Quebec, Canada) passes through an appropriate filter according to the excitation wavelength of the reporter protein and then through the condenser after which it reaches the objective and the sample via a dichroic mirror. The emission light passes through the dichroic mirror as well, then through the emission filter, and is detected by the CCD camera. Three different filter sets are to observe fluorescence of the three different fluorescent reporters used in this work, GFP, mVenus, and mCerulean. The precise sets of excitation filter, beam splitter, and emission

filter are: 470/40 nm 495 nm 525/50 nm (filter set 38HE, Zeiss, Oberkochen, Germany) for GFP, 500/24 nm, 520 nm, 542/27 nm (filter set F36-528, AHF Analysentechnik, Tübingen, Germany) for mVenus and 438/24 nm, 458 nm, 483/32 nm for mCerulean (filter set F36-544, AHF Analysentechnik, Tübingen, Germany).

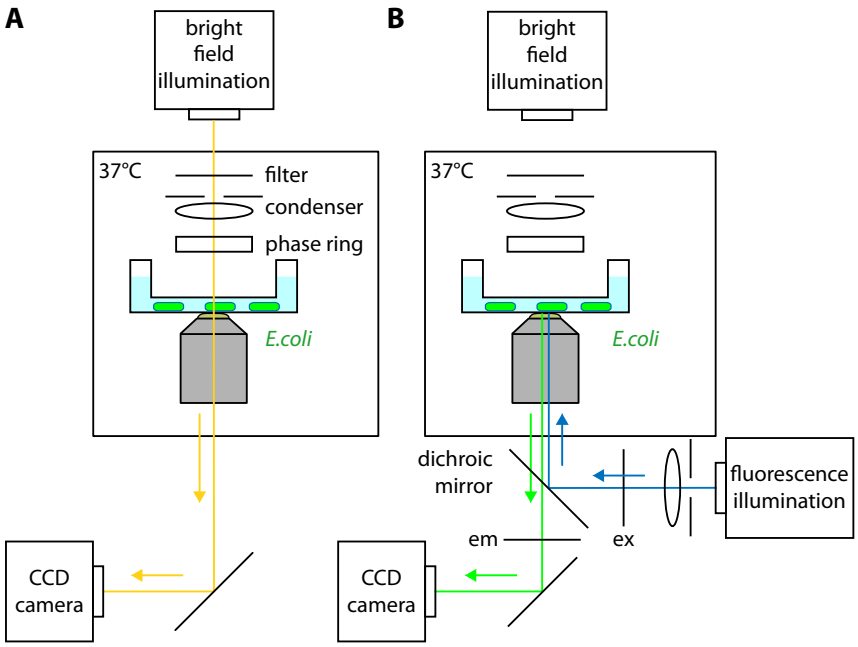

Figure 3.1.: Experimental setup with an inverse microscope.
A) In bright field illumination, light from a halogen lamp reaches the sample after passing through the optics of filter, condenser and phase ring, is collected by the objective and is guided to the CCD camera. **B)** In fluorescence illumination, light is selected by an appropriate filter for excitation ex, reaches the sample and is guided to the CCD camera through an appropriate filter for emission em.

Time-lapse microscopy provides the possibility to track single cells over time and to observe variability between cells as well as dynamic processes such as growth or the expression of a few genes, which allows to elucidate the physiological function of gene circuits [60]. Depending on the time scale of the processes of interest, individual pictures of the time-lapse movie are taken with spacing between seconds up to hours. A prerequisite for following single cells over longer periods of time is that they are fixed on a surface and stay in focus. To keep them in focus, hardware or software based autofocus options are available, but sometimes manually corrections are still required. In this work, most of the correction of the shift in z-direction due to thermal drift was done by a software-based autofocus implemented in μManager, the software which was used to control all measuring devices [61]. Depending on how bacteria are immobilized, another limiting aspect of imaging living cells is their growth out of the focal plane. After one or two cell divisions, *E. coli* cells, which are fixed to the surface by PLL, often only stick with one end to the surface and

protrude into the open space above. Then, especially the analysis of area based growth is not possible anymore. For further details on fixation methods, see Section 3.4.
For the analysis of the arabinose, the NAG, and the sorbitol utilization network, *E. coli* cells were fixed to the surface of a channel of a $\mu-$SlideVI$^{0.4}$ ibidi chamber (ibidi, Martinsried, Germany) coated with PLL (Biochrom GmbH, Berlin, Germany).

3.2. Microfluidic system

A flow system was used to provide a constant sugar concentration in the bacterial environment during the whole experiment (Fig. 3.2). A syringe pump (TSE syringe pump 540100, Modell Infusion, TSE Systems GmbH, Bad Homburg, Germany), filled with medium of the desired sugar concentration, was connected via flexible tubes to one end of a channel of the microfluidic device in which the cells were immobilized on the surface. The other end of the channel was coupled to a waste box. To guarantee ideal growth conditions for *E.coli*, the sample was heated to 37 °C and the medium was pre-heated as well to assure that it is also at 37 °C when reaching the sample.

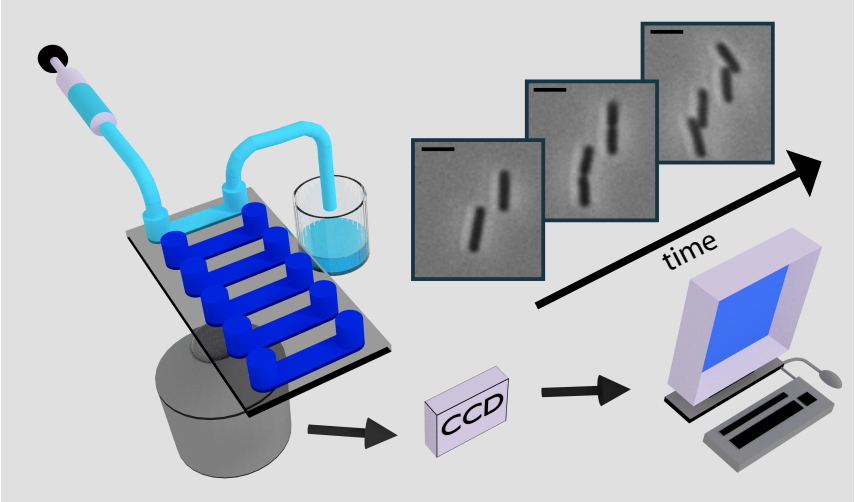

Figure 3.2.: Flow system to provide homogeneous external conditions over time. A constant flow of 1 ml/h is maintained by a syringe pump, which flushes the medium of desired composition through a channel of the microfluidic device where bacteria are fixed on the bottom. Afterwards, the medium is collected in a waste box. When installed within an inverted microscope, data of the progression of the fixed bacteria can be acquired. Exemplary pictures show growing bacteria over time. Scale bar: 2 µm. Figure taken from [62] is reprinted with permission from John Wiley & Sons, Inc.

During the preparation of the sample, air bubbles inside the flow system should be avoided. Once inside the system, they not only lead to unusable pictures when in focus, but also hamper the growing bacteria by temporarily cutting them off from nutrient supply. To

avoid air bubbles, all air was removed after the syringe had been filled with pre-warmed medium and had been connected with the flexible tube. Then, all non-adherent bacteria were eliminated by flushing the chamber manually, a metal rack was put around the channel for temperature stabilization and the empty waste tube was connected to one side of the channel. The resulting displacement of medium produced a meniscus on the other side of the channel, which was used to carefully connect the tube with the fresh medium to the other side of the channel, while the excessive medium was collected with a pipette. The rate of the syringe pump could be regulated in a range from 0.1 ml/h up to 400 ml/h. To avoid shear stress for *E.coli*, a moderate velocity of 1 ml/h was used [63].

3.3. Image analysis

Time-lapse movies were acquired automatically with the freeware µManager in order to gain information on cell growth or on gene expression. Image analysis was done with ImageJ (Wayne Rasband, National Institutes of Health, USA) supplemented with the plug-in CellEvaluator [64].

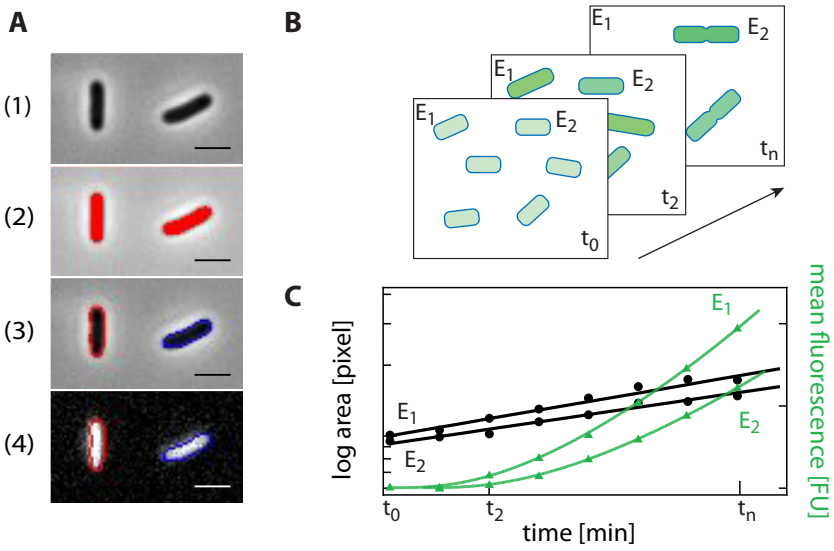

Figure 3.3.: Image processing.
A) For the image analysis, the normalized bright field images (1) are thresholded (2) to create the cells' outlines (3), which then are transferred to the fluorescent image (4). **B)** By following single bacteria E_1 and E_2 over time, information on cell growth and fluorescence is obtained. **C)** Tracking of the cells' area over time yields single-cell growth curves (black circles). Accordingly, the temporal evolution of fluorescence can be measured for single cells (green triangles). Scale bar: 2 µm.

After normalization to compensate for fluctuations of the background due to intensity changes of the halogen lamp, a threshold was applied to the inverted bright field images, which separates the cells from the background (see Fig. 3.3A). Then, this threshold was

used to determine the outlines of the cells. Single cells can be tracked throughout the whole stack (see Fig. 3.3B). Information on growth is obtained by following the development of the area of a cell over time (see Fig. 3.3C). Similarly, information on gene expression via intensity values is received by transferring the tracked outlines to the fluorescence images, which have been background-corrected before (see Fig. 3.3A, C). Mean fluorescence values are obtained by normalization of the sum of intensities of all pixels within the outline of one cell by the number of these pixels, which represents the area.
While growing, cells do not always fully stay in the focal plane but partly grow out of it. These cells have to be eliminated from the analysis, because skewness biases the area measurement. Furthermore, growth out of the focal plane limits the observation time. Further data analysis was performed with IgorPro 6.3 (WaveMetrics, Lake Oswego, OR) as well as with OriginPro 9.1 (OriginLab Corporation, Northampton, MA).

3.4. Techniques for fixation of bacteria on a surface

Fixation of *E. coli* on the PLL-coated surface of the ibidi channels works well within certain constraints. One limiting aspect is the duration of a measurement, which is limited to one to few doubling times. After this time, daughter cells start to lift off of the surface and hinder further data analysis. Another aspect is shear stress, which the cells suffer especially when medium is switched quickly. Last, PLL fixation does not work for gram-positive microorganisms like *B. subtilis* due to the composition of their cell membrane which differs from the cell membrane of gram-negative bacteria (shown in Fig. 2.1B). To meet these constraints, several alternative ways of fixation have been developed over the past few years. Among these are multilayer soft lithography and elastomechanical fixation [65, 66].
Especially, mechanical fixation of microorganisms under a thin hydrogel was further investigated within this work. One major advantage of this method is the spacial separation of bacteria and flow of medium, avoiding any shear induced detachment of bacteria. At the same time, bacteria which are fixed under the thin hydrogelic membrane are supplied with nutrients which diffuse through the membrane. Then, exchange of medium is possible without disturbing the fixed bacteria. However, the hydrogelic membrane has to be fixed as well to avoid aquaplaning, which would again mobilize the bacteria on the surface. The goal of this work, was to integrate such an elastomeric fixation into the commercially available ibidi channels.

To this end, polyethylene glycol-diacrylate (PEGDA) based microstructuring, a technique established for eukaryotic motility assays [67] was combined with elastomeric fixation of prokaryotes. PEGDA structures were used to stabilize a hydrogel lying on top of the bacteria on a cover slip. Agarose and poly-acrylamid (PA) are both suitable materials for the hydrogel. PA should be used for well-defined growth measurements, as most microor-

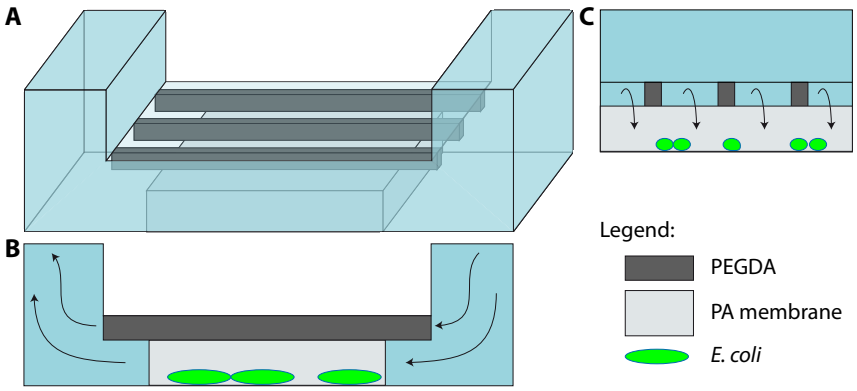

Figure 3.4.: Elastomechanical fixation of cells.
A) The general structure of the setup consists of a PA membrane (light gray) and several PEGDA structures (dark gray), which stick to the ceiling of the microfluidic device. **B)** The side view of the setup shows cells growing under a hydrogelic membrane, which is kept in place by PEGDA walls. Medium supply (blue) of the bacteria (green) is provided by diffusion through the hydrogel. **C)** The front view of the setup illustrates how medium flows between the PEGDA walls and diffuses through the PA membrane towards the bacteria.

ganisms cannot metabolize PA in contrast to agarose.
The general setup of the elastomechanical fixation is shown in Fig. 3.4A. several walls (dark gray) of 150 µm thickness are bound to the ceiling of a microfluidic device and keep a hydrogelic membrane (light gray) fixed to the floor. Thickness, height and spacing of the walls are parameters which can be tuned depending on the specific application they are produced for.
Fabrication of the microstructured walls was done as described in [68]. In short, a PDMS mold obtained from a patterned silicon wafer was placed on the ceiling of a sticky-Slide $VI^{0.4}$ (ibidi, Munich, Germany) after having been both exposed to argon plasma for 30 sec. By capillary force-induced flow, the empty spaces are filled with a PEGDA solution containing 2 % of photo-initiator 2-hydroxy-t-methylpropiophenone (v/v), which cures under UV light exposure. Then, the PDMS mold has to be removed carefully, because the walls can occasionally be pulled off the surface, depending on the aspect ratio of the walls and on the strength of the binding of the PEGDA walls to the surface.
Then, the setup is put together as follows: The cells, placed on a standard polymeric coverslip (ibidi, Martinsried, Germany), are covered with a 350 µm thick, hydrogelic membrane before the pre-structured sticky-Slide is added on top. Then, medium can be added, which will flow through the spaces between the PEGDA walls and reach the cells by diffusion through the membrane (Fig. 3.4B, C).

To check if this fixation method does allow undisturbed growth of cells, gram-negative *E. coli* cells as well as gram-positive *B. subtilis* cells were put under PA hydrogels, were provided with LB-rich medium and were observed over time. Both organisms nicely grew within the setup and could be observed for 6 to 7 doublings while perfectly staying in the

focal plane all the time. This observation period is much longer than the one for PLL-fixed cells with 1 to 3 duplications, and it is only limited by the fact that the whole surface will be covered by bacteria at some point.

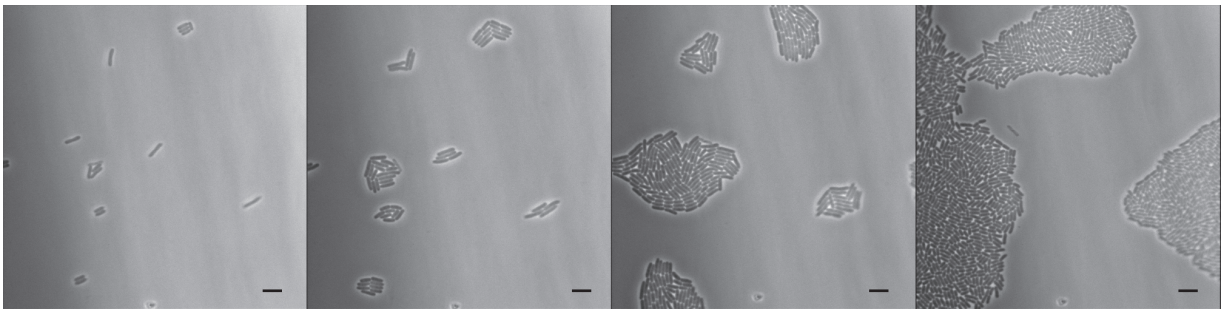

Figure 3.5.: Gram-negative cells fixed by a hydrogelic membrane.
E. coli cells are growing under a PA hydrogelic membrane of 350 µm height which is kept in place by 150 µm high PEGDA walls sticking to the top of the ibidi channel. Pictures are taken every 75 min. Scale bar: 5 µm.

In Fig. 3.5, single *E. coli* cells (strain MG1655) are grown under a PA hydrogel, which is fixed by 150 µm high PEGDA walls. These single cells can be observed forming colonies which cover the surface in a monolayer. Evaluation of the growth rate by the increase of the covered area in total yielded a mean doubling time of approximately (35 ± 2)min (mean value and standard deviation of several microcolonies). By counting the cell numbers for each image, a doubling time of (34 ± 4) min was obtained, which is in accordance with the area-based measurement and corresponds to fast growth reported in the literature [17].

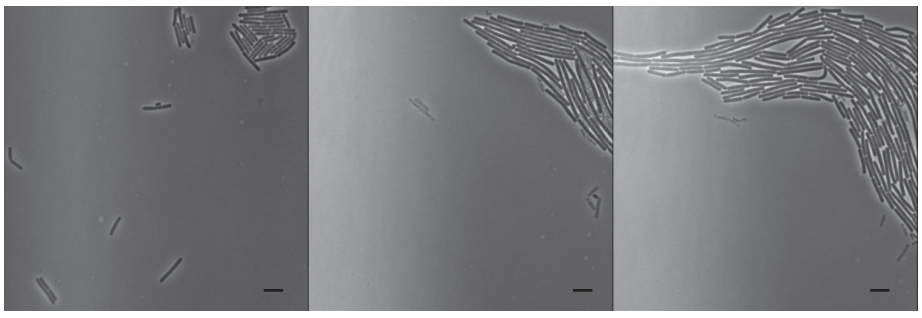

Figure 3.6.: Gram-positive cells fixed by a hydrogelic membrane.
Most of the *B. subtilis* cells under a PA hydrogelic membrane of 350 µm thickness are growing. The membrane is retained in place by 100 µm high PEGDA walls sticking to the top of the channel. Pictures are taken every 90 min. Scale bar: 5 µm.

Furthermore, gram-positive *B. subtilis* could also be grown in the setup described earlier. In Fig. 3.6, single *B. subtilis* cells (strain TMB1 172) are grown under a PA hydrogel, which is fixed by 100 µm high PEGDA structures. Cells form a monolayer while growing and stay in the x-y-plane. The doubling time was measured by the increase of the area,

which was covered by the bacteria over time, and equally by counting the cell number of each image. The value of (42 ± 4) min can typically be obtained for growth of *B. subtilis* in batch cultures.

To rate on which timescale nutrients will reach the bacteria under the hydrogel, the coefficient of diffusion is roughly estimated in the following. As a hydrogel, PA is mainly consisting of water. Thus, the diffusion coefficient of water is taken to estimate the time, nutrients take to reach the bacteria covered by a layer of 350 µm PA. Diffusion in water can generally be described by the Stokes-Einstein-Equation

$$D = \frac{k_B T}{6\pi\eta R_0} \tag{3.1}$$

with k_B being the Boltzmann coefficient, T the temperature, η the dynamic viscosity of water and R_0 the hydrodynamic radius of the diffusing substrates, which is roughly estimated to be in the order of 1 nm or smaller for hexoses. Then, the value for D is approximately $D = 2 \cdot 10^{-10}\,\mathrm{m^2/s}$, which is in good agreement with literature values for the diffusion of glucose in PA [69]. In consequence, diffusion through a 350 µm thick PA gel takes approximately the time $\tau = \frac{<r^2>}{6D} = 90\,\mathrm{s}$. This period should be kept in mind for shifts, when medium is changed.
Another aspect, which needs to be considered, is the effect of the pressure which is applied on the bacteria via the hydrogel and via the PEGDA structures on the ceiling of the microchannel. Taking literature's best suited value for the Young's modulus $E = 8.64\,\mathrm{kPa}$ (for a mixture of 7.5 % acrylamide with 0.3 % bis-acrylamide, see [70] and A.9), the pressure can be estimated to be

$$p = \frac{F}{A} = \frac{E\Delta l}{l_0} = \frac{8.64 \cdot 50}{350}\,\mathrm{kPa} = 1.2\,\mathrm{kPa} \tag{3.2}$$

with the force F per area A, and the change in height Δl in relation to the original height l_0. For *E. coli*, a pressure of approximately 500 MPa applied for several minutes leads in general to lethal damages [71]. Being five orders of magnitude below this lethal value, the pressure effect of the mechanical fixation method can most probably be neglected. Furthermore, the fact that growth was in the same order as measured for batch cultures supports the assumption that the fixation does not disturb the bacteria and that the provision with nutrients is also good.
Thus, the combination of PEGDA microstructured channels with elastomechanical fixation by a hydrogel is well suited for the observation of growth of gram-positive and gram-negative bacteria as both microorganisms tested within this work grew as fast as for batch conditions. Uncontrolled growth in z-direction is avoided, which allows much longer observation times than with PLL-fixed cells. As the method introduced here is integrated into commercially available microchannels, standard sample holders can be used without the need of further adjustment.

It turns out that the protocol of mechanical fixation of microorganisms integrated in ibidi slides works if no flow is applied. To enable the use of microfluidics, it could be desirable to improve two properties of the system. First, the binding of the PEGDA walls to the ceiling is tunable. Especially high walls ($> 100\,\mu m$) tended to turn over. Reduction of the aspect ratio of the height and the base area of the walls helped to stabilize them. But maybe, the strength of the binding between PEGDA and the polymeric surface of the channel can also be enhanced. Second, the immobilization of the bacteria could only be maintained without a constant flow of medium. It needs to be tested if more mechanical pressure applied through the hydrogel on the bacteria or a change in the hydrogel's geometry will enhance the fixation. With a larger hydrogel, the alignment with the borders of the channel could be optimized for example. Maybe even an overlap of the hydrogel and the borders will help to cut the bacteria or the hydrogel itself off from a mobilizing flow. Also the combination of PLL-based and elastomechanical fixation could improve the immobilization for gram-negative bacteria.

4. Phenotypic switching of the arabinose utilization system in single cells *

The arabinose utilization system, just as the lactose utilization system, ranks among the best studied sugar utilization systems in *E. coli*. Both systems are well characterized at the molecular level. While the lactose system is a classic example for negative transcription regulation, the arabinose is often used to study positive transcription regulation [73, 74]. Gene expression of the arabinose utilization system is induced by the pentose L-arabinose and all-or-nothing switch-like behaviour was observed and analyzed on the single-cell level [75, 76, 77]. In a previous study, gene expression dynamics was characterized on the single-cell level in a mutant strain unable to degrade arabinose by time-lapse fluorescence microscopy [12]. Analysis of these time-lapse data revealed significant heterogeneity in the time point of gene induction within a clonal population. This effect was called heterogeneous timing (see Section 2.5). Heterogeneity was found to be the more pronounced the smaller the concentration of external arabinose was, i.e. almost all cells simultaneously switched into the induced state at high concentrations of external arabinose while the timing of induction between single cells was highly variable at low concentrations. By theoretical analysis of the underlying regulatory network, variability in this induction timing could be linked to cell-to-cell variability in the number of arabinose transporters present at the time of sugar addition.
In a follow-up study, the effect of heterogeneous timing was shown to be a physiological behavior, as it was also observed in the native arabinose system [72]. Knowledge of this heterogeneous behavior during switching into the ON state raises the question of how the switching kinetics of induced cells back into the OFF state after sudden removal of external arabinose may look like. These kinetics are closely coupled to the depletion of intracellular arabinose, because this level accounts for the activation of the *ara* system via the regulator AraC. Internal arabinose can be depleted by degradation or by export, either active transport or passive diffusion.
In this Chapter, the switching kinetics from the ON into the OFF state is analyzed and the impact of intracellular arabinose depletion on this switching is investigated for arabinose degradation via the arabinose system and for a potential export protein.

*This chapter is based on the publication "Single-cell kinetics of phenotypic switching in the arabinose utilization system of *Escherichia coli*" [72].

4.1. The arabinose utilization system

The arabinose utilization system consists of several different genes coding for proteins for transport, metabolism and regulation. A schematic representation of the arabinose-dependent components and their interactions in the native system can be seen in Fig. 4.1A. To study the influence of arabinose degradation and a of potential export mechanism on the dynamics of the OFF switching, mutant strains were used with knockout of either only the gene *araBAD*, which is responsible for arabinose degradation (strain BW25113, Fig. 4.1B), or with knockout of *araBAD* and additionally of the gene *araJ*, whose function is still unknown (strain JW0386-1, Fig. 4.1C).

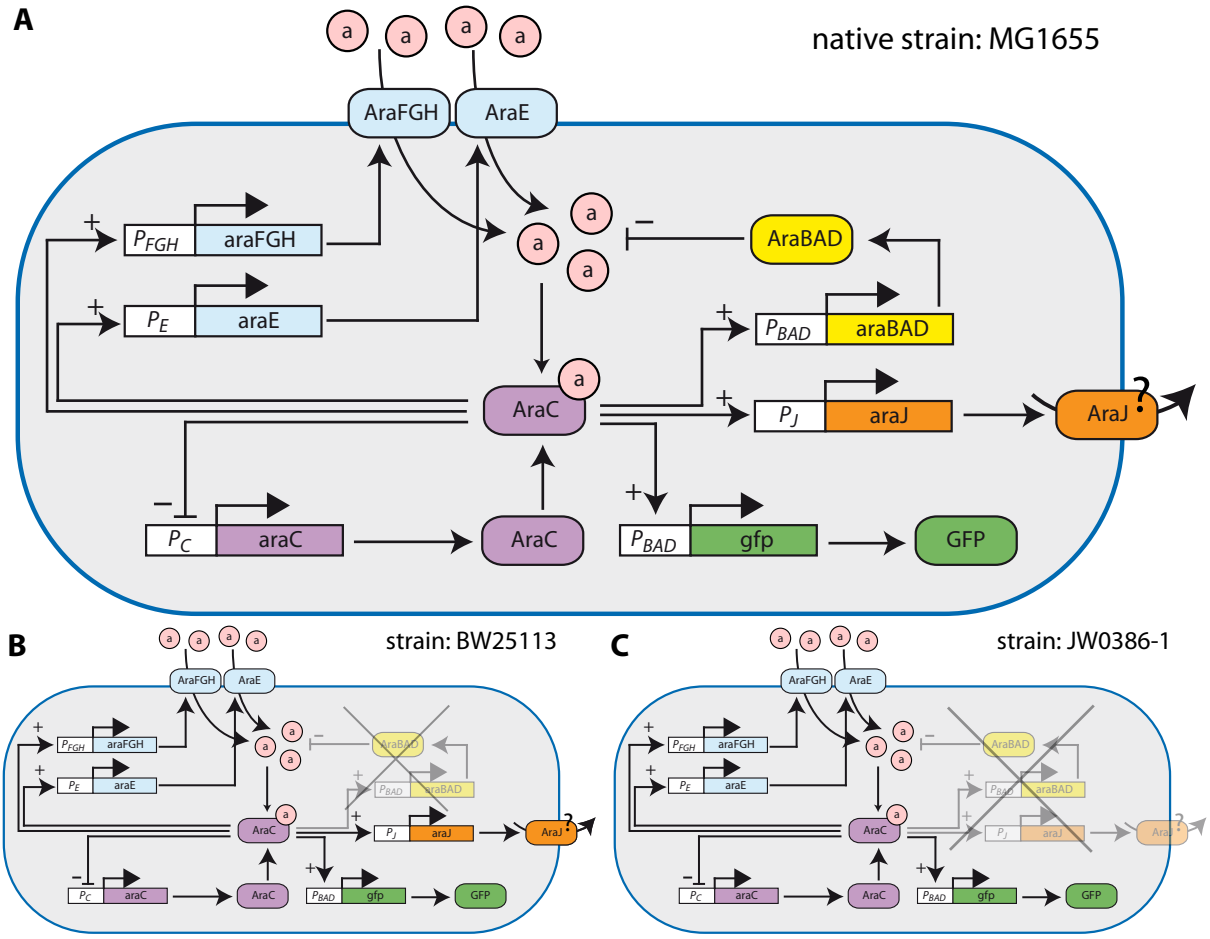

Figure 4.1.: The arabinose utilization system in *E. coli*.
A) In the native strain (MG1655), uptake proteins AraFGH and AraE (light blue) import the sugar arabinose (a, rose), which, when bound to the regulator AraC (purple), positively regulates all arabinose operons except its own. Via degradation by AraBAD, a negative feedback is exerted. The reporter *gfp* under the control of the same promoter as *araBAD* is integrated on plasmids. AraJ (orange) possibly acts as export protein. **B)** In strain BW25113, the gene encoding arabinose degradation *araBAD* is knocked out ($\Delta araBAD$). **C)** In strain JW036-1, *araJ* is knocked out in addition to *araBAD* ($\Delta araBAD$ $\Delta araJ$).

In more detail, the arabinose system consists of two import proteins, AraE and AraFGH, which specifically import arabinose. These two transporters differ in their affinity and capacity but operate interdependently [78]. At intermediate and at high sugar levels, the low-affinity, high-capacity transporter AraE was shown to be the dominating transporter [78]. Thus, only the transporter AraE will be considered as uptake protein within the model for switching dynamics used in this work.
Intracellular arabinose is degraded by AraBAD and can be bound by the regulator AraC. Arabinose-bound AraC stimulates initiation of mRNA synthesis from all arabinose-dependent promoters except from its own [79]. Thus, a positive feedback is build when the complex of imported arabinose and AraC activates expression of further transport proteins, which again import arabinose. In the absence of arabinose, AraC negatively regulates all these promoters, i.e. P_E, P_{FGH}, P_{BAD}, P_C, and P_J [80]. The later, *araJ*, is a poorly characterized arabinose-inducible gene, which displays sequence similarities with drug efflux enzymes [81, 82]. Thus, it might potentially serve as an efflux system to export intracellular arabinose [83].

4.2. Kinetics of gene expression in single cells after arabinose downshift

To characterize the switching kinetics of the arabinose system from the induced to the uninduced state, bacteria have been exposed to arabinose for 40 min. Then, arabinose was removed from the microfluidic chamber where bacteria were fixed on the surface and fresh, arabinose-free medium has been provided for another 60 min. External arabinose was provided at a saturating concentration, either at 0.2 % or at 0.5 %. During the whole time, gene expression dynamics of the reporter gene *gfp* under the control of P_{BAD} was recorded by fluorescence time-lapse microscopy. For direct comparison, gene expression dynamics was also recorded for cells that were continuously exposed to arabinose for 100 min. Exemplary time series are shown in Fig. 4.2 for bright field and fluorescence illumination. Within the bright field images, growth of single cells can be observed in the form of elongation of cells and division. By following the increase of the fluorescence signal in the fluorescence images, information is gained on the expression of proteins which are controlled by the arabinose regulation network. For better visualization of the increase of fluorescence, the contrast of the fluorescence images was changed after 30 min.

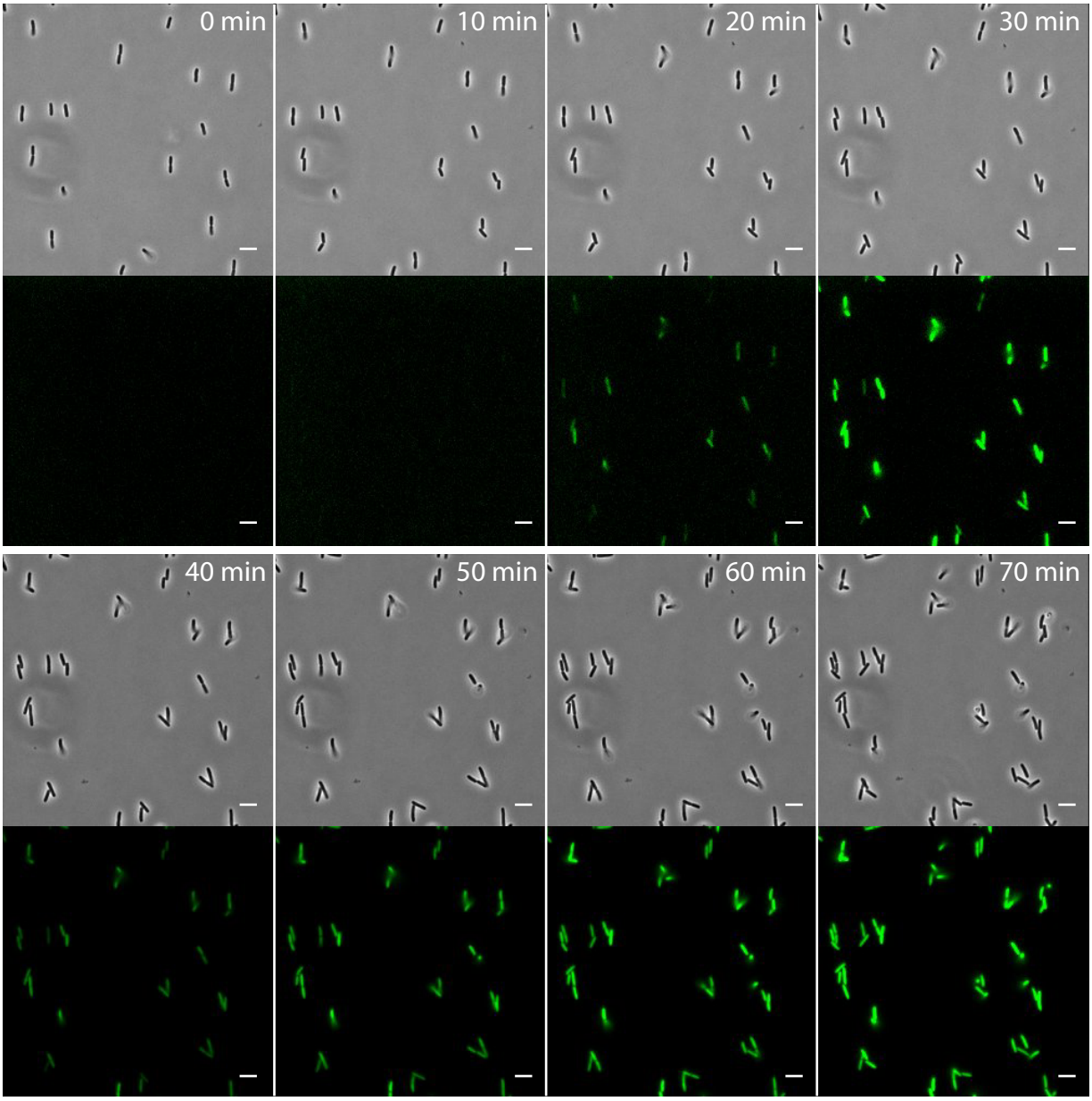

Figure 4.2.: Time series of bright field and fluorescence images.
Pictures were taken every 10 min and show growth of single cells as well as the increase in GFP fluorescence after induction with 0.2 % arabinose 3 min before the first image was taken. The contrast of the fluorescence images was changed after 30 min to enhance the visibility of the increase of the fluorescence. Scale bar: 5 µm.

Single-cell gene expression dynamics was measured in a strain unable to degrade arabinose for continuous arabinose supply as well as for a pulse of 40 min. Following the analysis described in Fig. 3.3, values of mean fluorescence were extracted for single cells and plotted against time. Fig. 4.3 shows measured data for single cells (black circles connected by thin black lines). Gene expression curves of single cells were fitted with a mathematical model (see Section 4.3, fits are thick gray lines in Fig. 4.3) in order to extract the dynamics

of the P_{BAD} promoter activity. While kinetics of the induction process for continuous supply of 0.5 % external arabinose is shown in Fig. 4.3A (upper panel), the respective activity of promoter P_{BAD} extracted by the fits can be seen in Fig. 4.3A (lower panel). Here, promoter activity switches from 0 to 1 homogeneously and fast in all cells. A similar behavior can be observed for the same strain when exposed to 0.5 % arabinose for 40 min: All cells start gene expression fast and homogeneously (Fig. 4.3B). However, after removal of arabinose at $t = 40$ min, the single-cell traces continue to increase for about 15 min until they reach maximal fluorescence and start to decrease slowly. The extracted promoter activity shows a fast switch from 1 to 0 with a median of the rate constant k estimated to be 2.2 min^{-1} (interquartile range (IQR) from 1.9 min^{-1} to 3.7 min^{-1}). Thus, transcription seems to be shut down within a few minutes. The model suggests that the time until the fluorescence reaches its maximum is mainly determined by the maturation time of GFP ($\langle \tau_m \rangle = 6.5$ min) [12]. The quick shut-off of gene expression should originate in a rapid decrease of intracellular arabinose concentration because the activity of the P_{BAD} promoter depends on the internal arabinose concentration. As strain BW25113 is unable to degrade arabinose, loss of internal arabinose needs to reflect any unknown, non-canonical catabolism or an export mechanism.

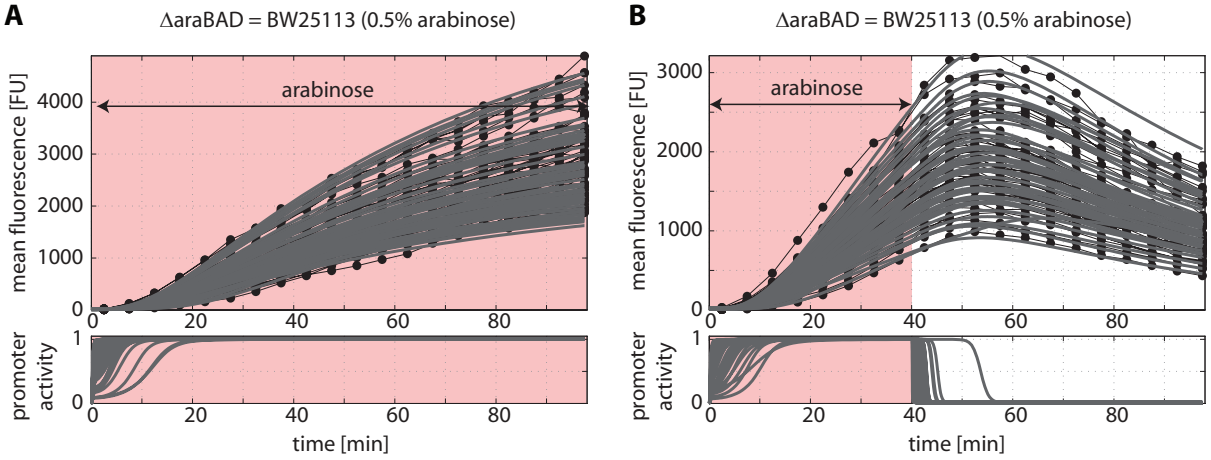

Figure 4.3.: Gene expression kinetics in single cells of a Δ*araBAD* strain (BW25113) for arabinose up- and downshift.
A) External arabinose (0.5 %) was added at time 0 and was provided for the next 100 min. During this time, mean fluorescence of single cells increases (black circles connected by thin black lines). Fits by the model (Section 4.3) to the data points are depicted in gray. In the lower panel, corresponding P_{BAD} promoter activity extracted from these fits is shown. **B)** External arabinose (0.5 %) was added at time 0 and removed after 40 min. Mean fluorescence of single cells starts to increase within a few minutes after induction and reaches its maximum value approximately 15 min after the removal of arabinose, before it starts to decrease slowly. Data points (black) and fits (gray) are shown. Promoter activity, shown in the lower panel, switches from 0 to 1 within a few minutes after addition of arabinose and quickly switches back to 0 after its removal. Graphics were adapted from [72].

To check whether the characteristics observed earlier is indeed physiological characteristics,

single-cell gene expression dynamics was measured in a strain with the native arabinose system (MG1655). On the one hand, the observed behavior of the native strain in Fig. 4.4 is quite similar to the one described before. After removal of external arabinose, fluorescence keeps rising for about 15 min, before it slowly drops down. The corresponding promoter activity shows a fast switch from 1 to 0 with a median of the rate constant k estimated to be 2.3 min^{-1} (IQR from 1.8 min^{-1} to 3.4 min^{-1}; see Fig. 4.4B). On the other hand, differences can be observed regarding initially switching from the OFF to the ON state. Here, heterogeneity in the timing of the switch of promoter activity is more pronounced than for the $\Delta araBAD$ mutant. As *araBAD* is expressed at a basal rate in the native strain, arabinose can be degraded at a slow rate immediately after being imported. This might plausibly explain a delay in the time until the internal arabinose level reaches the level necessary for gene activation.
As the shutdown dynamics does not vary significantly between the strain with native degradation and the strain without arabinose degradation, export mechanisms seem to be fundamental.

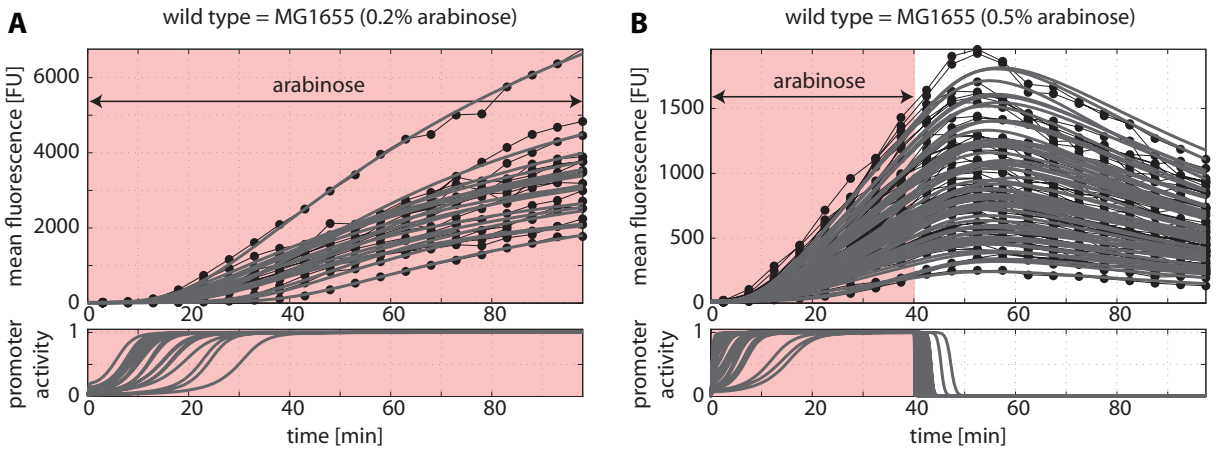

Figure 4.4.: Gene expression kinetics in single cells of the wild type strain (MG1655) for arabinose up- and downshift.
A) External arabinose (0.2 %) was added at time 0 and constantly provided for the next 100 min while mean fluorescence of single cells was measured every 5 min (black). Data was fitted (gray) with a mathematical model to extract the corresponding P_{BAD} promoter activity (lower panel). **B)** External arabinose (0.5 %) was added at time 0. Shortly after, the mean fluorescence of single cells started to increase. After 40 min, the arabinose was removed externally and mean fluorescence reached its maximum value approximately 15 min later. Data points (black) and fits (gray) are shown. Promoter activity switches from 0 to 1 within a few minutes after addition of arabinose and quickly switches back to 0 after removal of arabinose (lower panel). Graphics were adapted from [72].

To test to which extent the gene enconding a potential export protein, *araJ*, influences the switching kinetics of the arabinose system, single-cell gene expression dynamics was measured in a $\Delta araBAD\Delta araJ$ strain (JW0386-1). In this strain, switching from the OFF into the ON state was again found to be quite homogeneous and fast (see Fig. 4.5).

The slightly higher heterogeneity in the timing of the switching (Fig. 4.5A) compared to the timing of the switching in the strain with native *araJ* (Fig. 4.3A) might originate from the reduced arabinose concentration of 0.2 %. Regarding the downshift from the induced to the uninduced state, evaluation of the fits yielded a median of the rate constant for arabinose loss k of 1.4 min^{-1} (IQR from 0.8 to 2.0 min^{-1}). This value is only a little smaller than the values of both strains with intact *araJ*, indicating, if at all, only a very weak influence of AraJ. In conclusion, AraJ does not seem to be rate-limiting for depletion of internal arabinose in *E. coli*.

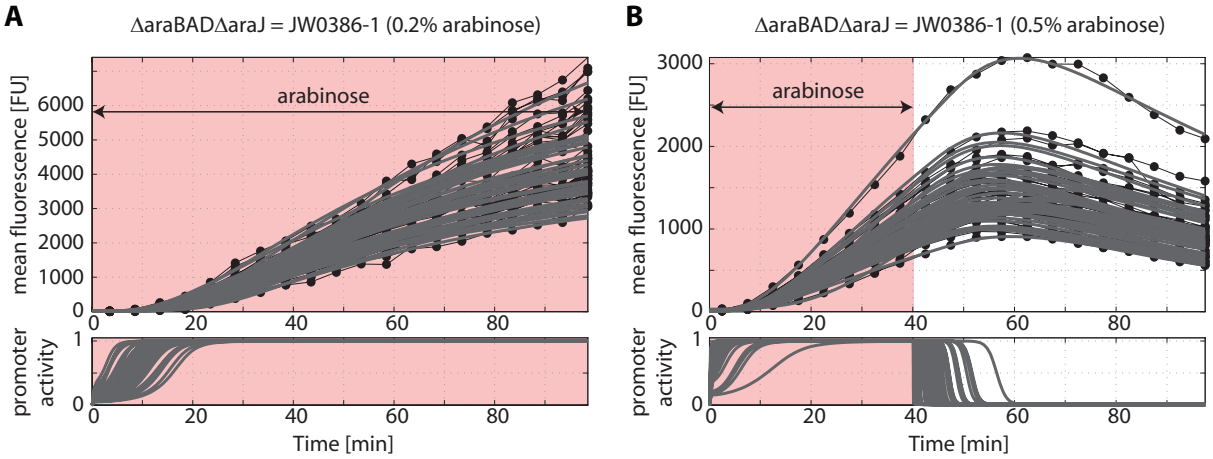

Figure 4.5.: Gene expression kinetics in single cells of a Δ*araBAD* Δ*araJ* strain (JW0386-1) for arabinose up- and downshift.
A) After addition of 0.2 % external arabinose at time 0, trajectories of mean fluorescence of single cells were measured (black) and fitted by the model (Section 4.3, gray lines) in order to extract the corresponding P_{BAD} promoter activity (lower panel). **B)** Mean fluorescence of single cells increases quickly after induction with 0.5 % arabinose and reaches its maximum value approximately 15 min after arabinose removal. Then, the signal starts to decrease slowly (data black and fits gray). Promoter activity, shown in the lower panel, quickly switches from 0 to 1 after addition of arabinose. After removal of arabinose, it switches back to 0 again. Graphics adapted from [72].

4.3. Mathematical model

To model the single-cell dynamics of internal arabinose concentration and gene regulation, a set of rate equations was used as described in [72].
The internal arabinose concentration, $a^{int}(t)$, increases with the concentration of arabinose transporters, $N(t)$, and the uptake rate per transporter, V_{upt}, as follows

$$\partial_t a^{int}(t) = V_{upt} N(t) - (k + \gamma) a^{int}(t) \tag{4.1a}$$

$$\partial_t a^{int}(t) = V_{upt} N(t) - (kN(t) + \gamma) a^{int}(t), \tag{4.1b}$$

where γ denotes the rate of cell growth, which dilutes the internal arabinose concentration and k denotes a rate constant summarizing all other possible processes of arabinose decrease. Examples for these processes are arabinose degradation by AraBAD or by any other non-canonical metabolic pathway, leakage of arabinose via the transporters AraE, AraFGH, or even via other transporters [84], as well as active export by sugar export systems. Eq. 4.1a and Eq. 4.1b are two alternative versions covering the extremes of loss processes which can either be independent of $N(t)$ or dependent on $N(t)$ (see Section 4.4 for further discussion).
The import of sugar is modeled following Michaelis-Menten kinetics by

$$V_{upt} = V_{max} \frac{a^{ex}}{K_M + a^{ex}}, \tag{4.2}$$

where V_{max} is the maximal transport rate of arabinose, K_M is the Michaelis-Menten constant, and a^{ex} is the concentration of arabinose that is present externally.
Transcription of *araBAD* was found to increase cubically with the internal arabinose concentration [85]. Due to the high comparability between the promoters P_E and P_{BAD} [79], the transcription rate ν_i for both promoters is modeled similarly as a Hill function with a Hill coefficient of 3

$$\nu_i = \nu_{0,i} + (\nu_{max,i} - \nu_{0,i}) \frac{(a^{int})^3}{K_a^3 + (a^{int})^3}, \tag{4.3}$$

where $\nu_{0,i}$ denotes the basal and $\nu_{max,i}$ the maximal transcription rate with $i \in \{e, g\}$ for promoter P_E and P_{BAD} (which drives *gfp* expression), respectively. K_a is the dissociation constant for arabinose binding. As AraC's negative regulation of its own expression results in homeostatic control of AraC concentration, the dynamics of *araC* expression is not considered explicitly [74]. Then, concentration of mRNA of AraE, $n(t)$, and of GFP, $g(t)$, obey the rate equations

$$\partial_t n(t) = \nu_e - (\lambda_e + \gamma) n(t) \tag{4.4a}$$

$$\partial_t g(t) = \nu_g - (\lambda_g + \gamma) g(t), \tag{4.4b}$$

where λ_e and λ_g denote the degradation rates of mRNA of AraE and GFP, respectively. Accordingly, concentration of the mature protein AraE, $N(t)$, follows

$$\partial_t N(t) = \mu_e n(t) - \gamma N(t), \tag{4.5}$$

where μ_e denotes the translation rate of AraE. Likewise, protein dynamics of immature

GFP, $I(t)$, as well as of mature GFP, $G(t)$, follow

$$\partial_t I(t) = \mu_g g(t) - (\tau_m^{-1} + \gamma) I(t) \tag{4.6a}$$

$$\partial_t G(t) = \tau_m^{-1} I(t) - (\tau_{bleach}^{-1} + \gamma) G(t), \tag{4.6b}$$

where μ_g denotes the translation rate of GFP, τ_m the maturation time of GFP (see Chapter 5 for further information), and τ_{bleach} the time constant of the process of GFP bleaching. In order to directly compare the model and the experiments, a scaling factor σ was introduced to convert protein concentration $G(t)$ into arbitrary fluorescence units $F(t)$ via $F(t) = \sigma G(t)$.
The parameters of the model were either estimated from the experimental data, e.g. for γ, or fixed to values taken from the literature (see Table A.4 for further details). Parameters $\nu_{0,e}$, $\nu_{max,g}$, and k were estimated by numerical solving of Eq. 4.1a - Eq. 4.6b with MATLAB (The MathWorks, Inc.).

4.4. Discussion

Taken together, all experiments with downshift of external arabinose from high concentration (0.5 % or 0.2 %) to no arabinose show that expression of the arabinose utilization system is turned off within the first minute after removal of external arabinose. As this behavior was found for a strain with the native arabinose system and for a strain unable to degrade arabinose ($\Delta araBAD$), as well as for a strain with knockout of a potential exporter of arabinose ($\Delta araJ$), internal depletion of arabinose does not seem to depend on degradation via AraBAD or on export via AraJ. However, investigation of the downshift behavior relies on the maturation of GFP ($\langle \tau_m \rangle = 6.5\,\text{min}$) [12], which is a relatively slow process compared to the estimated time constant of arabinose depletion ($\langle k^{-1} \rangle = 0.5\,\text{min}$). Thus, this time constant can only be seen as an upper limit of depletion of internal arabinose. The actual speed of arabinose depletion might even be faster than this estimated value.
Concerning potential export mechanisms of arabinose, the import proteins of the arabinose utilization system have to be taken into consideration as well. While AraFGH needs energy from ATP hydrolysis to actively import arabinose, which excludes export, AraE works as a chemiosmotic sugar H^+ symport system [78]. If cells in an arabinose-free medium contain high amounts of intracellular arabinose, a strong gradient arises, which drives arabinose outwards and possibly can no longer be balanced by an inward-directed proton gradient. Then, arabinose could leak out via AraE. Within the model, we also considered the extreme case, where all of the loss of internal arabinose occurs via the arabinose transporter AraE, see Eq. 4.1b. This alternative model is also compatible with the data and could explain the rapid transcriptional shutdown after arabinose removal as well as the heterogeneous timing of gene induction in a narrow parameter regime of

export rates. Over all, AraE-dependent export via Eq. 4.1b could not be distinguished from AraE-independent export via Eq. 4.1a. Hence, a depletion mechanism needs to be included in the model essentially to explain the data, but discrimination between constitutive or arabinose-induced depletion or a mixture of both is not possible with these experiments.

In the first place, to export a carbon source seems to be an energy-wasting mechanisms. But why is it reasonable for a cell to invest in an additional depletion mechanism besides catabolism? Sugar export systems have also been discussed in the context of toxic sugar analogues [86]. The uptake of such toxic substrates not only inhibits the uptake of the non-toxic sugar substrate but also can interfere with metabolic pathways and result in inhibition of growth [87]. For the non-metabolizable analogue of lactose, the thiomethylgalactoside (TMG), studies reported actual export from *Streptococcus pyogenes* and potential export from *E. coli*, due to the observation of fast switching from the ON to the OFF state of the *lac* operon after sudden removal of external TMG [88, 89]. In the case of the arabinose system, competitive inhibitors such as D-xylose and D-fucose can likely be uptaken via the arabinose permease system but have a highly reduced rate of metabolization compared to arabinose [84, 90]. When accumulating to high amounts in the absence of a suitable export mechanism, such substrates can become toxic (the dose makes the poison, as already Paracelsus said). Finally, arabinose could be exported by a member of the major facilitator superfamily [91]. This superfamily includes antibiotic resistance exporters and thus is engaged in the export of potentially toxic substrates.

5. Determination of the maturation time of mVenus and mCerulean on the single cell level

As already discussed in Fig. 2.1, fluorescent proteins need to undergo a maturation step to become fully functional. This maturation can take some time, ranging from several minutes up to several hours [10]. The maturation efficiency depends - among other parameters - on the availability of molecular oxygen and on the temperature [26]. Originating from the non-37 °C organism *Aequorea victoria*, some effort had to be made to create several variants of the original fluorescent protein and to optimize these variants with respect to the level of gene expression, brightness, photostability, and excitation and emission spectra so that they can be used as reporters in cells at 37 °C [26].
Because we aim at comparing expression of sugar utilization systems in the PTS by the help of the reporter proteins mVenus and mCerulean, knowledge of their maturation constants is of importance. As we are also interested in heterogeneity within a population, the variance of the maturation constants is of interest, as well. Thus, we measured the maturation times for both fluorescent proteins.
We used two reporter plasmids, the reporter plasmid pVS133 containing *mVenus* and the reporter plasmid pKES316 containing *mCerulean*, in strain MG1655 to determine the maturation times of mVenus and mCerulean, respectively. In both plasmids, the reporter is controlled by the *lac* promoter, which can be induced by the artificial inducer isopropyl-β-D-thiogalactopyranosid (IPTG). Following the protocol from Megerle et al., which was used to determine the maturation time of GFPmut3 to be $< \tau_m^{GFP} >= 6.5\,(\pm 0.6)\,\mathrm{min}$ [12], we inhibited transcription by the addition of 200 µg/ml chloramphenicol 30 min after induction with 2 mM IPTG and recorded the subsequent increase of the fluorescence signal in single cells every 4 min using time-lapse fluorescence microscopy. As chloramphenicol immediately blocks translation, further increase of the fluorescence signal after 30 min reflects the maturation dynamics of the remaining, initially non-fluorescent, proteins. By exponentially fitting the single-cell time-traces, maturation times τ_m were obtained. A subset of representative trajectories for mVenus and mCerulean is shown in Fig. 5.1A and Fig. 5.2A, respectively. Analysis of the distributions of these time constants in Fig. 5.1B and Fig. 5.2B yields an average maturation time of $\tau_m^{mVenus} = 14.0\,(\pm 3.1)\,\mathrm{min}$ for mVenus and an average maturation time of $\tau_m^{mCerulean} = 10.5\,(\pm 3.0)\,\mathrm{min}$ for mCerulean.

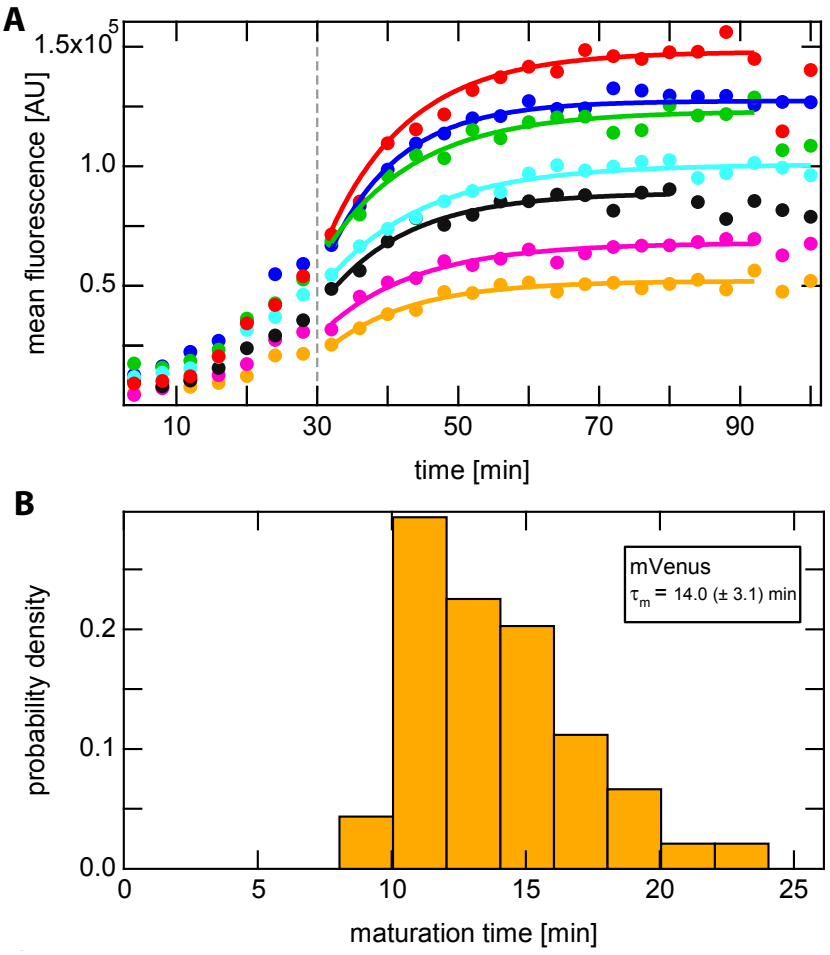

Figure 5.1.: Maturation kinetics of mVenus in single cells.
A) 30 min after induction of *mVenus* expression with 2 mM IPTG, protein synthesis was inhibited by the addition of 200 µg/ml chloramphenicol as indicated by a dashed, vertical line. Exponential fits to the measured data points are shown for each single cell in corresponding color. **B)** These exponential fits yield the distribution of the maturation time with average maturation time $\tau_m^{mVenus} = 14.0\,(\pm 3.1)$ min. Statistics was obtained from 44 cells.

Within the standard errors, both fluorescence proteins mature similarly fast. Hence, they are well suited for comparative examinations of two different sugar utilization systems.
In the literature, most data of maturation times is measured *in vitro*. The maturation process of a proper folded fluorescent protein most importantly consists of the formation of the chromophore, in which the steps of chromophore cyclization, oxidation and dehydration are involved. In general, oxidation is reported to be the rate limiting step [23]. Oxidation for *mVenus* was measured *in vitro* using a re-oxidation assay to be in the order between 2 min [31] and 10^2 min [92]. A comparison with our *in vivo* values is not reasonable, not only because of the broad distribution of these values found in the literature but also due to the absence of certain cytosolic compounds *in vitro* which might influence folding and maturation *in vivo* [92].

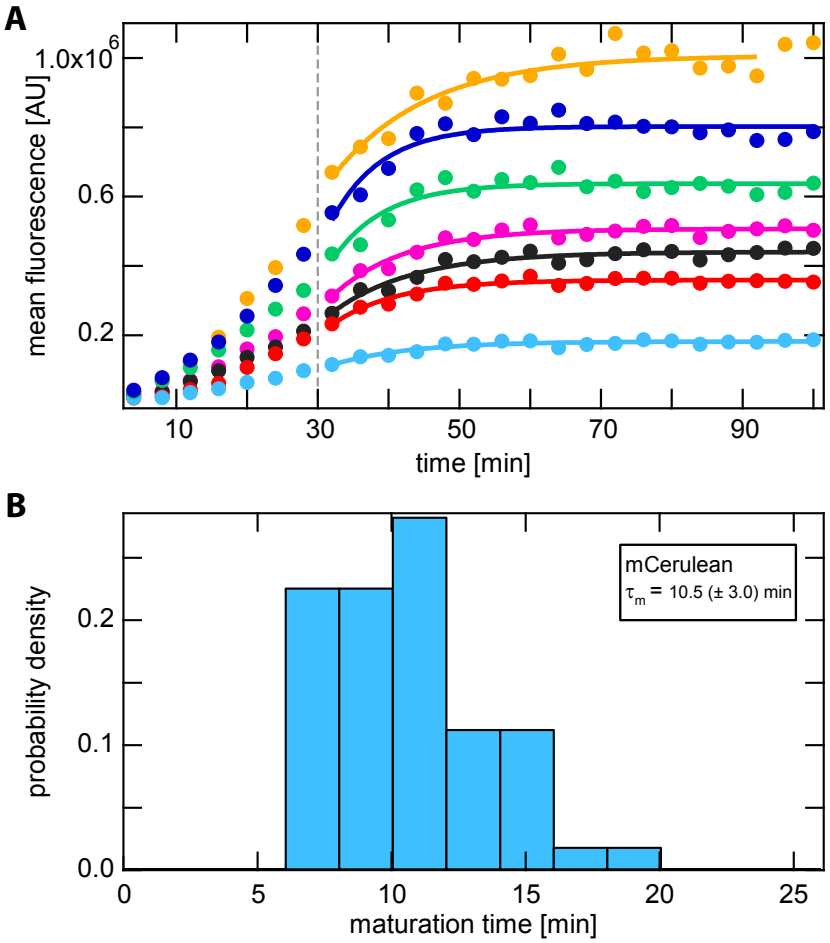

Figure 5.2.: Maturation kinetics of mCerulean in single cells.
A) Protein synthesis of mCerulean was inhibited by the addition of 200 µg/ml chloramphenicol 30 min after induction with 2 mM IPTG (see dashed, vertical line). For a few representative single cells, measured data points and exponential fits are shown. **B)** Fits were used to extract the maturation time of each cell. Distribution of the maturation times yields the average maturation time $\tau_m^{mCerulean} = 10.5\,(\pm 3.0)$ min. Statistics was obtained from 53 cells.

As no precise *in vivo* measurement could be found to compare the maturation times of *mVenus* and *mCerulean*, the data presented here is likely to be the first detailed measurement of maturation times for these fluorescent proteins.
For this work, another important finding is the similar cell-to-cell variation in maturation times for mVenus and mCerulean. Thus, both fluorescent proteins show the same level of heterogeneity in maturation. Similar maturation constants and similar variation are both relevant properties permitting the direct comparison of relative fluorescent levels, for example in a phase diagram taken at a certain time point.

6. Single-cell characterization of metabolic switching in the Phosphotransferase System of E. coli *

In the following, the PTS in general and the NAG and the sorbitol system in particular are introduced, growth on NAG and on sorbitol is presented, which was measured in batch solution and for immobilized microcolonies. Gene expression of both systmes was measured by the help of fluorescent proteins as reporters. The phase-diagram of gene expression in dependence of external sugar concentrations is discussed by the help of a mathematical model.

6.1. The Phospho-enol-pyruvate: Carbohydrate Phosphotransferase System

One of the main players in CCR (see Section 2.3) is the Phospho-enol-pyruvate (PEP): Carbohydrate Phosphotransferase System (PTS). In the following, the general structure of this global sugar utilization system with regulatory function will be introduced as well as two specific members studied in this work, the NAG and the sorbitol system.

6.1.1. The general structure of the PTS

The PTS is present in all eubacterial species, as for example in *B. subtilis*, *Salmonella enterica*, and *E. coli* [93, 94]. The PTS governs the import and metabolism of over 20 different sugars [95, 96, 97]. During import through the inner cell wall, all substrates transported by the PTS are modified by the addition of a phosphoryl group. The membrane-bound uptake enzymes are called enzymes II (EII) [96].
Usually, bacteria contain many different EIIs, each specialized in a specific sugar or sometimes also in a group of closely related sugars [94]. The EIIs consist of one to four different domains named A, B, C, and D. At least one of these domains is membrane-spanning

*This chapter is based on the publication "Single-cell characterization of metabolic switching in the sugar phosphotransferase system of *Escherichia coli*" [62].

and catalyzes the transport of the substrate it is specific for [95]. Mostly, the EIIA domain is freely diffusing in the cytoplasm, while the other domains are often fused to the membrane-spanning domain and build a complex which is located at the cytosolic side of the membrane [94]. To distinguish the EIIs, a three letter code is used as a superscript: $EIIA^{glc}$ stands for the glucose specific EIIA component. On the basis of their tertiary structure, EIIs are classified into different families. This classification differs in the literature, as some authors distinguish superfamilies and families slightly different than others [95, 96].
Nevertheless, the reaction of sugar import via EII is irreversible for all families. Thus, once the sugar has been transported through the membrane and the phosphor group has been added, it will not be exported via these enzymes again. In contrast, all other reactions comprise the transport of phosphoryl groups from PEP to EII by enzymes, which are not specific for a particular sugar, and are reversible. The first non-specific PTS enzyme involved in transfer of phosphoryl groups is enzyme I (EI) which is encoded on the *ptsI* gene [96]. EI recruits phosphoryl groups through the conversion of PEP to pyruvate. The second non-specific PTS enzyme is the histidine-containing protein (HPr) which is encoded on the *ptsH* gene. HPr transfers the phosphoryl group from EI towards the specific transporters EII [96]. See Fig. 6.1A for a scheme of this chain of phosphoryl transfer.
In the unphosphorylated state, the uptake enzymes II cannot efficiently import the substrate. Thus, the phosphoryl supply of the importers is a limiting factor for sugar uptake. Especially, if two or more different sugars are present, the sugar specific importers have to compete for phosphoryl provision at HPr, which becomes a bottleneck for phosphoryl supply. In this respect, the PTS can be seen as a model system of flux-limited regulation where several inputs are regulated in parallel by one dominant flux of phosphoryl groups (compare with Fig. 2.9) [16].

6.1.2. The NAG and the sorbitol utilization system

To elucidate metabolic switching in the PTS, two sugar utilization systems, the NAG and the sorbitol system were chosen because of the following reasons: First, both these systems are inducible by their respective sugar, consistent with a positive feedback mechanism [98, 99, 100]. Second, both systems are specific with respect to crosstalk in transport and degradation. The PTS regulatory network for the NAG and the sorbitol system is schematically shown in Fig. 6.1.

The NAG system

The monosaccharide NAG is a derivative of glucose with the chemical formula $C_8H_{15}NO_6$ (see Fig. 6.2A) and a molar weight of $m_M = 221.21\,\mathrm{g/mol}$. NAG is part of the bacterial cell wall building the peptidoglycan layer together with N-acetylmuramic acid and crosslinking oligopeptides (see Fig. 2.1C) [17]. Furthermore, NAG is an important component of the cell walls of most fungi and is part of the polymer chitin, which forms the outer wall of

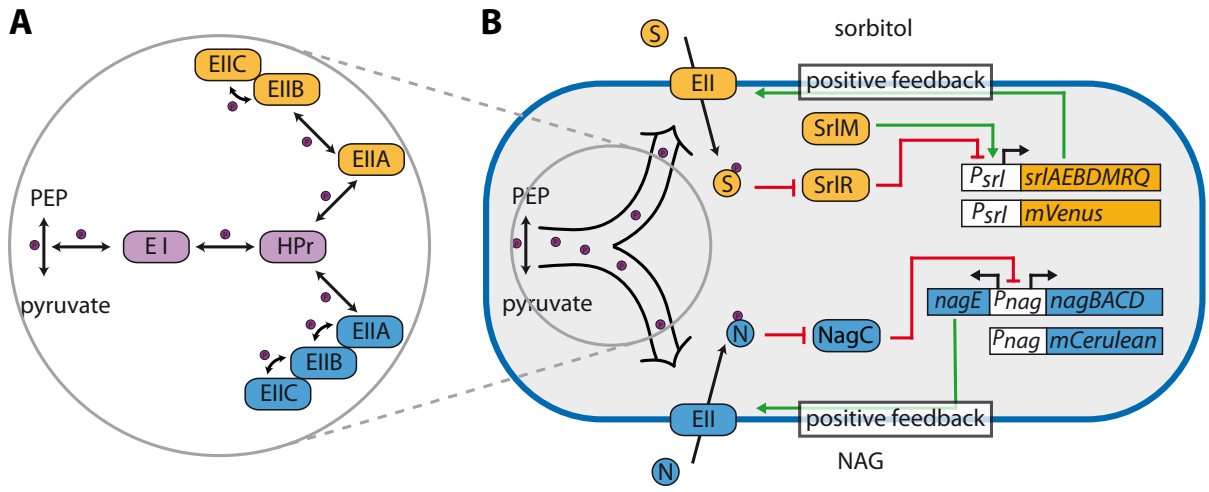

Figure 6.1.: Schematic view of PTS regulation in *E. coli*.
A) The phosphoryl flux in the PTS starts by the transfer of a phosphoryl group (purple) from PEP to EI, which is then handed over to HPr. Here, different EIIAs compete for phosphoryl supply to provide it to their EIIBC partners. **B)** The total phosphoryl flux from PEP branches into specific fluxes towards substrate-specific EIIs, here towards $EIIA^{srl}$ (orange) and $EIIA^{NAG}$ (blue). Each specific flux can initiate a positive feedback loop by its impact on the regulation of gene expression via activation of substrate-specific genes. Reporter genes *mVenus* and *mCerulean* are chromosomally integrated behind a copy of the sorbitol and of the NAG promoter, respectively. Figure adapted from [62] with permission from John Wiley & Sons, Inc.

insects [101, 102].
The PTS enzyme EII^{NAG} belongs to the glucose family. The *nag* regulon is located at 15.5 min on the *E. coli* map [103, 104]. It is a divergent regulon with co-regulation of the genes *nagE* and *nagBACD* [99]. The gene *nagE* codes for the permease and contains the EIIA, EIIB, and EIIC domains, which form a single polypeptide chain [93]. The gene *nagB* codes for a deaminase, *nagA* for a deacetylase, *nagC* for the NAG repressor, and *nagD* for a fairly general ribonucleotide monophosphatase [99, 100, 105]. In absence of the inducer NAG, the repressor NagC binds to an overlapping region of the transcription start sites of *nagE* and *nagB*, which results in the formation of a loop of DNA [100]. In the presence of phosphorylated NAG, derepression of the *nag* operon was observed [99]. Thus, in the NAG system, the repression of the binding of the repressor to its binding site leads to activation of the genes.

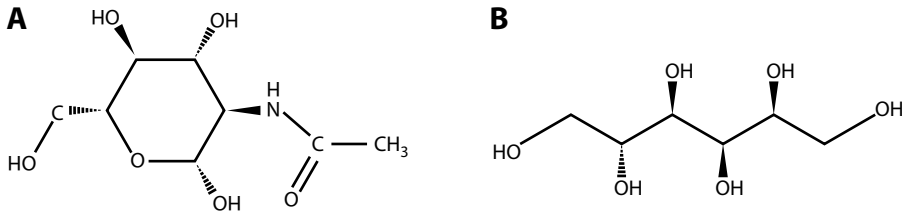

Figure 6.2.: Chemical structure of NAG and sorbitol.
A) NAG consists of 8 carbon atoms and belongs to the amino-sugars due to its nitrogen atom. **B)** As a member of the hexoses, sorbitol consists of 6 carbon atoms.

The sorbitol system

The sugar alcohol sorbitol, also known as glucitol, is also a derivative of glucose (by reduction of the aldehyd group). With the chemical formula $C_6H_{14}O_6$ (see Fig. 6.2), sorbitol has a molar weight of $m_M = 182.17\,\mathrm{g/mol}$. Sorbitol is an isomer of mannitol with a different orientation of the hydroxyl group on the second carbon but with very different chemical properties. Sorbitol is naturally occurring in many stone fruits and berries of trees belonging to the genus *Sorbus*.
The PTS enzymes EII^{srl} belong to the glucitol family of transporters [106]. The *srlAEBDMRQ* operon is located at 58 min on the *E. coli* chromosome [98, 107, 108]. The gene *srlABE* codes for the permease EII. The EIIA and EIIB domains are encoded in *srlB* and *srlE*, respectively. Unlike in all other enzyme II complexes characterized so far, the EIIC domain of the glucitol family is split into two parts encoded in the genes *srlA* and *srlE* [95, 109]. The EIIB domain of sorbitol is always fused to the N-terminus of one of the EIIC parts [110]. EIIA, on the contrary, is freely diffusible in the cytosol [95]. The gene *srlD* codes for an NADH-dependent dehydrogenase, *srlM* codes for an activator, and *srlR* codes for a repressor of the *srl* operon [111, 106, 98]. SrlR repression is inhibited by the inducer sorbitol. Thus, in the sorbitol system, the binding of SrlM and the unbinding of SrlR both activate gene expression.

6.2. Diauxic growth on a mixture of NAG and sorbitol

In order to gain information on the specific utilization strategy of *E. coli* in a mixture of NAG and sorbitol, growth on these substrates was analyzed for an MG1655-based strain (T1683). To that, 2 mM sorbitol in combination with several levels of NAG concentration were tested in batch culture, in which the initial concentration of the former substrate was kept constant while that of the latter substrate was varied. These measurements revealed diauxic growth with two distinct exponential growth phases separated by a ∼30 min lag phase, see Fig. 6.3A. The start of the lag phase shifted to later time points and higher optical density upon increase of the initial NAG concentration. Quantitatively, when the

level of initial NAG concentration was raised by a factor of two, the optical density of the lag phase increased correspondingly. This correlation between the NAG concentration and the first growth phase clearly indicates preferential utilization of NAG over sorbitol (Fig. 6.3A).

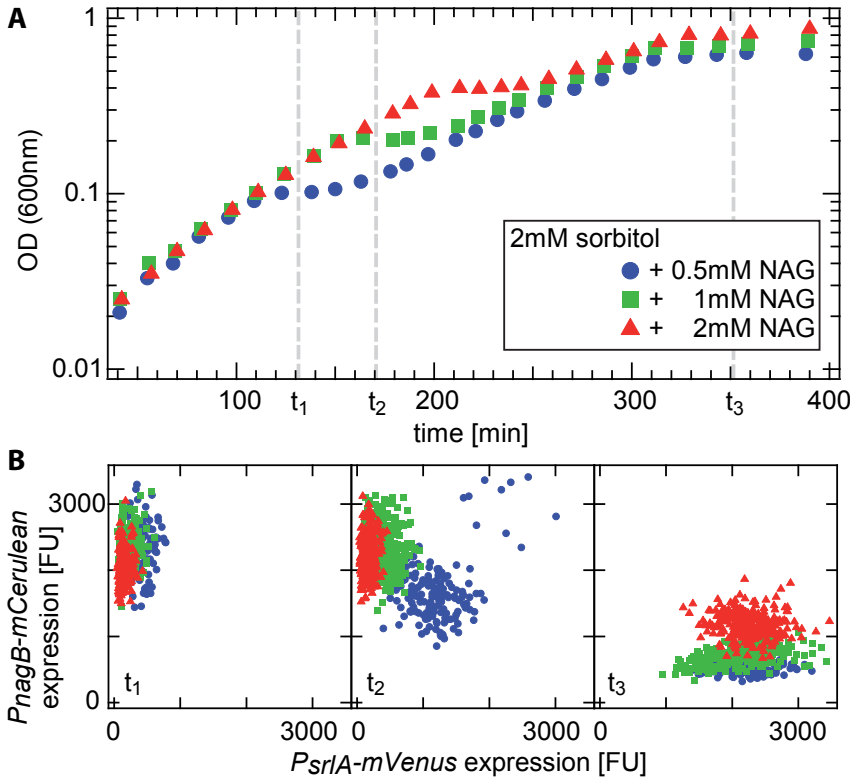

Figure 6.3.: Measurement of diauxic growth.
A) Growth measurements for bacteria cultured on the indicated mixtures of sorbitol and of NAG as carbon sources. Two distinct growth rates are separated by a lag phase of ~ 30 min, a characteristics which is signifcant for diauxic growth. With increasing initial NAG concentration, the start of this lag phase shifts in time. **B)** Correlation plot of $P_{srlA} - mVenus$ and $P_{nagB} - mCerulean$ gene expression measured at three different time points in the growth curve shown in **A**. At time t_1 - during the first growth phase - all cells express *mCerulean*, indicating exclusive utilization of NAG. At time t_2, cells in culture depicted in blue activate mVenus fluorescence, which monitors expression of the sorbitol system. At time t_3, all cells show mVenus levels above the basal level, while mCerulean levels are considerably decreased. Colors correspond to the sugar concentrations specified in **A**.
Numbers of cells evaluated: 75, 138, 168 (for t_1 blue, green, red); 168, 280, 337 (for t_2 blue, green, red); 169, 185, 269 (for t_3 blue, green, red). Figure taken from [62] is reprinted with permission from John Wiley & Sons, Inc.

To test whether NAG is indeed the preferred substrate during the first growth phase, growth on NAG alone was measured as well. Actually, the average doubling time on NAG alone is approximately the same as the one during the first growth phase (see Fig. 6.4), suggesting that sorbitol usage is minimal before depletion of NAG. Fig. 6.4 shows growth

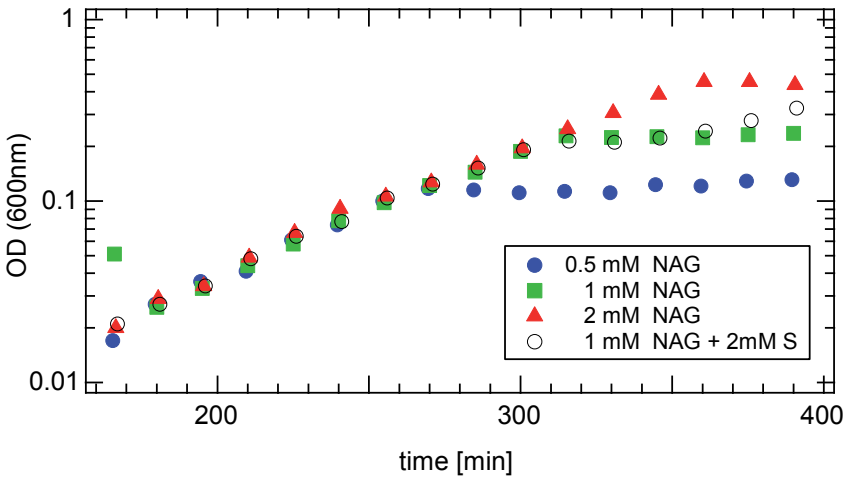

Figure 6.4.: Growth on NAG as sole carbon source.
Growth measurements for bacteria cultured on the indicated concentrations of NAG with or without sorbitol. Blue circle, green rectangle, and red triangle data correspond to NAG concentrations as in Fig. 6.3A, but without any sorbitol added. For comparison, black ring data represents a duplicate measurement of the green data in Fig. 6.3. During the first growth phase, all four cultures show similar doubling times, indicating that growth is essentially fueled by NAG alone even when sorbitol is present at the same time. Here, fitting of the three measurements of growth on NAG alone gives an average doubling time (with standard deviation) of (41 ± 3) min. Figure adapted from [62] with permission from John Wiley & Sons, Inc.

measurements on three different concentrations of NAG (0.5 mM, 1 mM and 2 mM). The recorded growth curves all show the same slope and reach different heights, corresponding to the individual NAG concentrations. In addition, the slope of all curves corresponds to the slope of a culture where NAG and sorbitol were both present as in Fig. 6.3. The mean doubling time of growth on NAG as sole carbon source extracted from Fig. 6.4 is (41 ± 3) min. This value is in accordance with the mean doubling time of the first growth phase of measurements with NAG and sorbitol of (38 ± 4) min (extracted from Fig. 6.3A and Fig. 6.4). In contrast, evaluation of the second growth phase in Fig. 6.3A yielded a mean doubling time of (73 ± 14) min.
The interpretation of preferential NAG utilization during the first growth phase is consistent with the expression behavior of the NAG and of the sorbitol utilization system, as probed with chromosomally integrated fluorescent reporters (Fig. 6.3B).
As a reporter for the NAG system, *mCerulean* was fused to an additional copy of the P_{nagB} promoter and for the sorbitol system, *mVenus* was fused to an additional copy of the P_{srlA} promoter, see Fig. 6.1, Chapter 3 and Appendix A.5 and A.6 for constructional detail. For cells sampled at different time points from the batch cultures, the single-cell fluorescence levels (per cell area) of both reporters were recorded and quantified (see Fig. 3.3). The three panels of Fig. 6.3B correspond to the three different time points along the diauxic growth curve of Fig. 6.3A. Each panel shows three fluorescence distributions, which cor-

respond to the three different NAG concentrations.
At time t_1, 130 min after dilution of the pre-culture, all three cultures show high fluorescence intensities of mCerulean between 1500 FU and 3500 FU, while the same cells do not raise in mVenus fluorescence above 1000 FU in agreement with the position being in the middle of the first growth phase or just at the beginning of the plateau in the case of the lowest NAG concentration (blue circles).
At time t_2 ($t_2 = 170$ min), the culture of the highest NAG concentration, still in the first exponential growth phase, shows similar fluorescence intensities as at time t_1 (red triangles in Fig. 6.3). At the same time, the culture of the lowest NAG concentration of 0.5 mM is significantly shifted towards lower mCerulean and higher mVenus fluorescence intensities. This trend can even be observed at much lower shape for the culture of intermediate NAG concentration (green rectangles).
Eventually, at time t_3 ($t_3 = 350$ min), all cultures have reached the final plateau after the second growth phase. Here, mVenus fluorescence values are between 1000 FU and 3500 FU for all cells in all cultures, while mCerulean fluorescence values are mainly found to be lower than 1000 FU, except for the culture with the highest NAG concentration (red triangles). This culture is the last to change from NAG utilization during the first growth phase to sorbitol consumption. As the decrease in mCerulean fluorescence is only caused by dilution through growth and not by active degradation, a shorter distance from the plateau corresponding to few doublings (red triangles) is reflected in fluorescence values which are less decreased than for a culture with a higher distance corresponding to more duplications (blue circles).
For reasons of comparison, growth was measured on a mixture of glucose and either NAG or sorbitol as well, showing a preferred use of glucose as expected (see Appendix A.2).

Together, only the NAG utilization system is significantly expressed (relative to the respective full induction level) before the diauxic shift. After the diauxic shift, the cells express only the sorbitol utilization system.
While these results show that, overall, NAG is preferred over sorbitol as a carbon source, they do not characterize the concentration-dependent competition between the two utilization systems. Once the preferred carbon source has reached the micromolar regime in a batch culture, it is very rapidly depleted, such that no detailed information can be obtained about the transition regime. However, this regime is essential for our understanding of the underlying regulatory strategy. Therefore, all further experiments were performed under a constant flow of medium with adjustable NAG and sorbitol concentrations using a microfluidic setup (Fig. 3.2).

6.3. Concentration-dependent microcolony growth on NAG or on sorbitol

With the microfluidic setup, the carbon-limited growth on micromolar concentrations of NAG as well as the carbon-limited growth on equally low concentrations of sorbitol were first characterized separately. Bacteria of the reporter strain (T1683) were pre-cultured in defined media with millimolar concentration of the respective carbon source and were transferred into the microfluidic channel. Then, fresh medium with a micromolar concentration of the same carbon source was constantly flushed by. Time-lapse movies in bright field illumination were recorded for each concentration to determine the growth rate from exponential fits to the total cell area of individual microcolonies (see Fig. 6.5A for exemplary traces at 20 µM sorbitol). Data of at least two independent experiments were averaged to obtain the mean growth rates of each external sugar concentration tested, which are plotted in Fig. 6.5B.

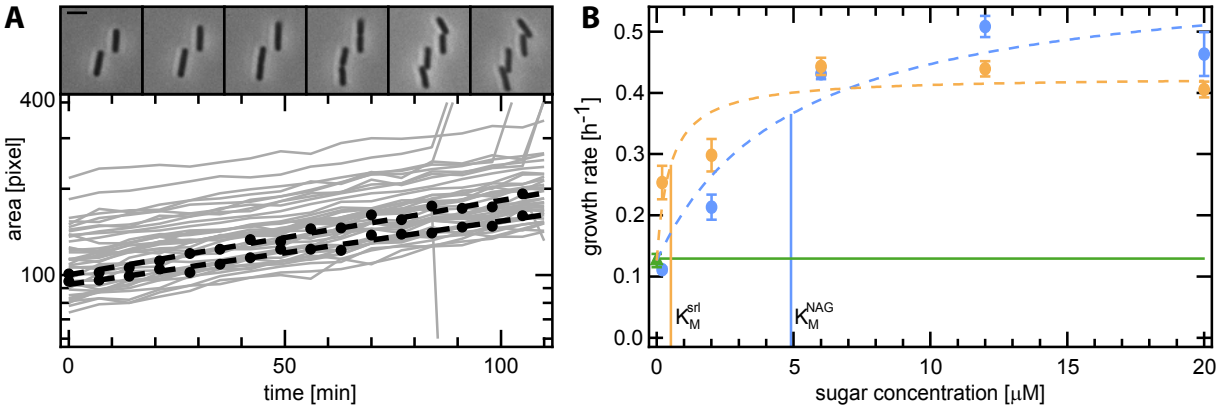

Figure 6.5.: Growth characteristics on NAG or on sorbitol
A) Time traces of the cell area of individual bacteria are shown. The black circles correspond to the cells in the bright field images at the top. The dashed lines represent fits to these data. Scale bar: 2 µm. **B)** Growth rates (mean values) are plotted as a function of NAG concentration (blue) and sorbitol concentration (orange). Data was obtained as in A and evaluated for microcolonies. The growth rate for cells perfused with minimal medium without any added carbon source is shown in green (green triangle with green line as threshold of growth to guide the eye). This background growth represents the lower limit of growth. Data points are fitted (dashed lines) with a Monod growth model (Eq. 6.1) to obtain the maximal growth rate λ_{max} as well as the concentration of half-maximal growth K_M. Mean and standard errors were derived from at least two independent experiments. Figure taken from [62] is reprinted with permission from John Wiley & Sons, Inc.

Consistently, these resulting growth rates are well fitted with a model of microbial growth described by Monod [39] of the form

$$\lambda(c) = \Delta\lambda \frac{c}{K_M + c} + \lambda_0 \tag{6.1}$$

(see dashed fits in Fig. 6.5B), where $\lambda(c)$ is the concentration-dependent growth rate, $\Delta\lambda$ is the maximal growth rate difference that can be gained by the added carbon source, c is the carbon source's concentration, K_M is the concentration of half-maximal growth increase, and λ_0 is the background growth rate under flow of medium without a carbon source added. In Fig. 6.5B, data measured on sorbitol is plotted in orange, data measured on NAG is plotted in blue. Fits of Eq. 6.1 to the data yield a maximal overall growth rate of $\lambda_{max}^{NAG} = \Delta\lambda^{NAG} + \lambda_0 = (0.60 \pm 0.11)\,\mathrm{h}^{-1}$ and a K_M of $K_M^{NAG} = (4.9 \pm 3.4)\,\mu\mathrm{M}$ for the NAG system, and $\lambda_{max}^{srl} = (0.42 \pm 0.04)\,\mathrm{h}^{-1}$ and $K_M^{srl} = (0.5 \pm 0.4)\,\mu\mathrm{M}$ for the sorbitol system (see dashed lines in Fig. 6.5B). A similar growth rate of $\lambda_{max}^{srl} = (0.46 \pm 0.01)\,\mathrm{h}^{-1}$ has previously been reported for wild type *E. coli* in N-C medium supplied with 20 mM sorbitol as carbon source [112]. NAG, on the contrary, belongs to the glucose family and glucose itself is well known to be a carbon source allowing for quite fast growth of *E. coli*. Measurements of batch culture growth on NAG yielded values comparable to growth on glucose [113]. Thus, a higher growth rate measured on NAG than on sorbitol is consistent with the literature.

The fact that a non-zero growth rate was measured even for medium without any carbon source added might seem puzzling at first sight. But apart from salts, the minimal medium M63 contains thiamine (1 g/ml), which might support a slow rate of residual growth in the absence of another carbon source. In addition, contaminants (such as trace amounts of organic carbon) in any of the ingredients could support growth. Indeed, residual growth was previously reported in buffer or even distilled water, where purifying the ingredients could not fully prevent cell growth [114]. The background growth rate $\lambda_0 = (0.13 \pm 0.01)\,\mathrm{h}^{-1}$ measured in this work is comparable to the "non-zero growth rate on contaminants" which recently was measured in a microfluidic setup in which the minimal Medium M9 was constantly replenished [115]. This suggests that a low rate of residual growth seems to be unavoidable in microfluidic setups. So far, the non-PTS substrate thiamine is not known to affect the competition between the two PTS systems, NAG and sorbitol, which are in the focus of this study. In addition, the source of residual growth is constantly replenished within the microfluidic device and should hence be constant across all conditions tested, i.e. all combinations of sugar concentrations. Thus, as little systematic bias as possible is introduced by the setup used here.

A comparison of the fits of the NAG and of the sorbitol data in Fig. 6.5B shows that the growth rate on NAG exceeds that on sorbitol at NAG concentrations of 10 µM and higher. However, while growth in this range of sugar concentrations is faster on NAG than on sorbitol, the growth rate on NAG alone drops below the growth rate on sorbitol alone once NAG approaches its K_M value in the range of micromolar single-digit. This change of local maximal growth indicates a potential change of substrate preferences at low sugar concentrations.

Likely, the inferred values for the constant K_M reflect the effective affinity of the import proteins for their respective substrate, since cells did enter the begin of the growth measurement in a fully induced state concerning this substrate. Thus, the sugar-specific

metabolic enzymes and also the transport systems are expected to be fully expressed so that copy numbers of these components should not be limiting.

6.4. Characterization of gene expression for mixtures of NAG and sorbitol

To characterize the expression of the competing sugar utilization systems, we quantified fluorescence of the reporters mCerulean ($P_{nagB} - mCerulean$) and mVenus ($P_{srlA} - mVenus$) for single cells fixed in the microfluidic chamber while perfused by medium containing various mixtures of the two substrates in the low micromolar range. Integration of the genes of two different fluorescent proteins, *mCerulean* and *mVenus*, as reporters into the chromosome of a MG1655-based *E. coli* strain was done in a collaboration with K. Schnetz. For the measurements of gene expression, bacteria were pre-cultured in defined M63 medium containing 0.5 % glycerol as sole carbon source. When cultures had reached an $OD_{600\,nm}$ of ∼0.1-0.3, cells were transferred into the microfluidic chamber. Immediately after, the carbon utilization systems were induced by flushing them with fresh medium containing NAG or sorbitol or a mixture of both - but no glycerol - at a constant flow rate. Preculturing in the non-PTS sugar glycerol was carried out to avoid biasing the competition between the sugar utilization systems by pre-inducing one of the probed systems.

6.4.1. Gene expression of the NAG system and of the sorbitol system

First, cells were induced with only a single sugar at a time and fluorescence signals of mCerulean and mVenus were quantified 120 min after induction. A representative distribution of a population's expression pattern is received by plotting the normalized number of cells against their mean intensity of the fluorescence signal (Fig. 6.6A, B). It became apparent that both promoters, the P_{nagB} and the P_{srlA}, can be activated by low micromolar sugar concentrations (at 1 µM NAG or sorbitol). However, comparison of the responses of the NAG and the sorbitol system revealed qualitative differences: While the response of the NAG system 120 min after induction is unimodal at all NAG concentrations tested with all cells of the population being either in the ON or in the OFF state (Fig. 6.6A), the response of the sorbitol system at the same time is bimodal for sorbitol concentrations from 1 to 20 µM (Fig. 6.6B). In this regime, most cells are strongly induced, while the remaining cells express the sorbitol system only at basal levels.

This bimodal behavior raises the question of the time evolution of these distributions, i.e. whether the proportion of induced and uninduced cells is changing over time. A quantitative analysis of single-cell gene expression data is not possible with the fixation method of PLL used here, because cells grow out of the focal plane after prolonged incubation. Nevertheless, qualitative analysis revealed similar fractions of sorbitol-ON cells at 120 min and

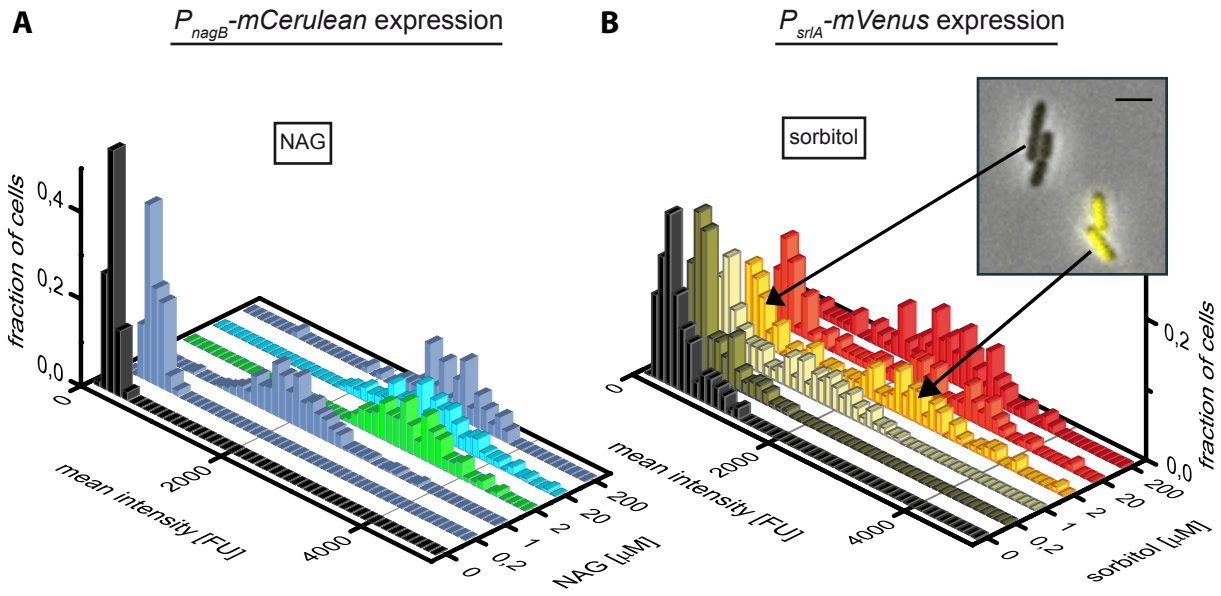

Figure 6.6.: Gene expression of the NAG and of the sorbitol system.
A) Gene expression of the NAG system in cells grown on NAG as sole carbon source was measured 120 min after induction for all concentrations (for 0 µM, the basal expression equals that at 0 min just before induction). A unimodal response can be observed for all concentrations tested. **B)** Gene expression of the sorbitol system in cells grown on sorbitol as sole carbon source was measured 120 min after induction. For most concentrations, the population of cells shows a bimodal behavior by splitting into two subpopulations. One subpopulation stays at basal expression levels while the other subpopulation switches to significantly higher expression levels. The basal expression level shown for 0 µM equals that at 0 min just before induction. The inlay shows an overlay of a fluorescence and a bright field image of bacteria which have been grown for 120 min on 2 µM external sorbitol. Scale bar: 2 µm.
Colors were chosen for better discrimination between different plots. For variation between replicate measurements, see Appendix A.2. Figure taken from [62] is reprinted with permission from John Wiley & Sons, Inc.

at 150 min and a significantly increased fraction at 270 min. 480 min after induction, cells not expressing the sorbitol utilization system were found only sporadically (see Fig. 6.7).

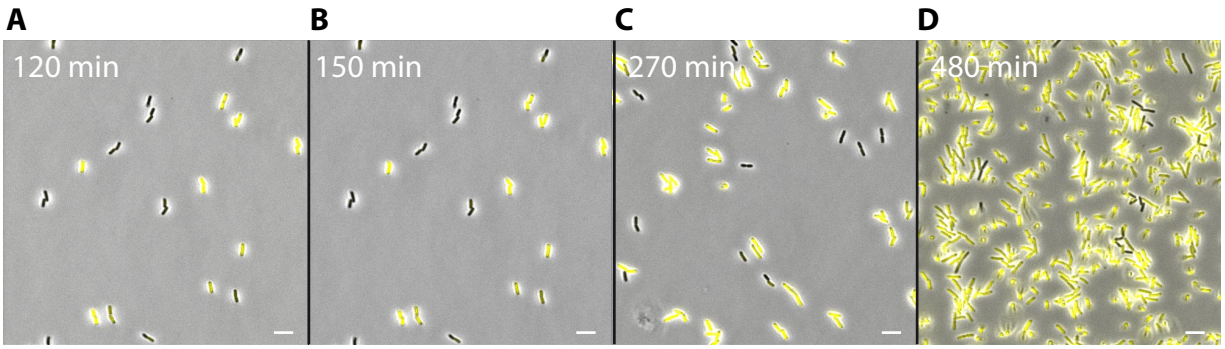

Figure 6.7.: Expression of *mVenus* over time.
A) The fraction of cells in the sorbitol-OFF state after 120 min of constant sorbitol supply (20 µM) and after **B)** 150 min of constant sorbitol supply is unchanged. **C)** Still, a non-negligible fraction of cells in the sorbitol-OFF state is found after 270 min of constant sorbitol supply (20 µM). Although these cells do not express the sorbitol system, cell division can also be observed. **D)** 480 min after induction with 2 µM NAG and 20 µM sorbitol, only very few cells are found in the sorbitol-OFF state. Most of the cells have activated the sorbitol system by that time. Scale bar: 5 µm.

Clearly, a highly variable time delay exists in the induction of the sorbitol system, which suggests that bimodality in the sorbitol system is only a transient phenomenon. Interestingly, this behavior is strikingly reminding of the heterogeneous time delay found in the induction of the arabinose utilization system (see Chapter 4) [12, 72]. In the arabinose system, non-linear positive feedback within the regulatory network can explain the heterogeneous time delay. Positive feedback is also part of the regulation of the sorbitol system. With the help of a simple theoretical model, it will subsequently be shown that different cooperativities involved in the regulation of the NAG and the sorbitol system can rationalize the differences in the behavior between these two systems (see Section 6.6).

6.4.2. Gene expression for mixtures of NAG and sorbitol

After the characterization of the response of the NAG and of the sorbitol system to their own substrates, the response of both sugar utilization systems to a mixture of both substrates is investigated next. Several experiments with 20 µM NAG and varying sorbitol concentrations showed that all cells always induced the NAG system (Fig. 6.8A), while simultaneous analysis of the same cells for the sorbitol reporter showed only basal expression (Fig. 6.8B). Thus, NAG at a concentration of 20 µM is clearly preferred over sorbitol and the expression of the sorbitol utilization system is inhibited by the expression of the NAG utilization system. This behavior corresponds to the behavior of diauxic growth

found in experiments with batch cultures (see Fig. 6.3).

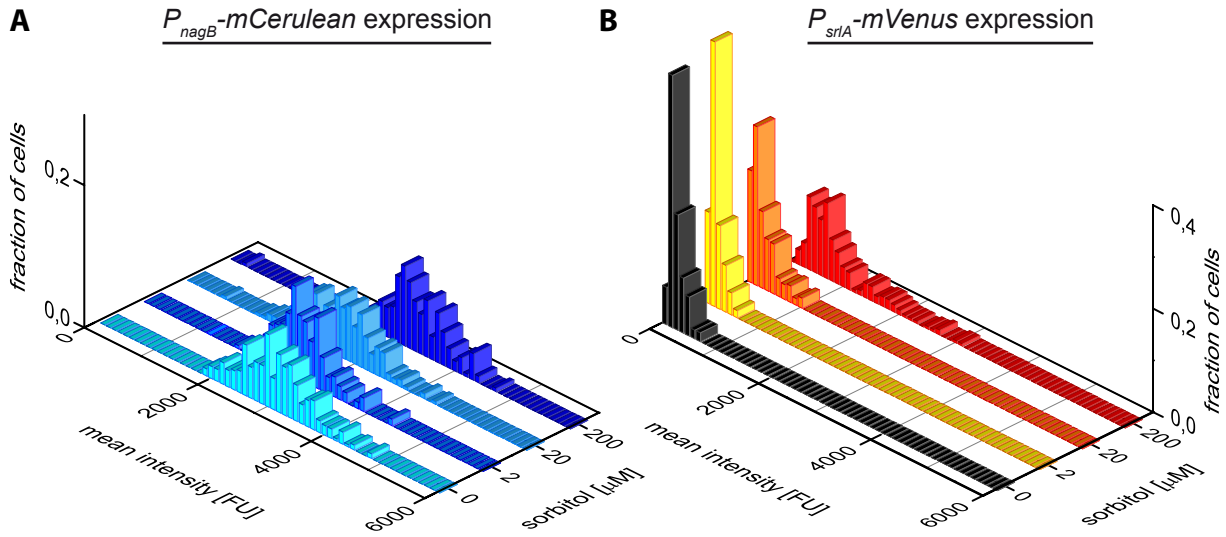

Figure 6.8.: Gene expression of the NAG and of the sorbitol system for 20 µM NAG and several concentrations of sorbitol.
A) Gene expression of the NAG system is shown 120 min after induction with 20 µM NAG and sorbitol. A unimodal response can be observed for all concentrations tested. Data for 0 µM sorbitol corresponds to data of 2 µM NAG in Fig. 6.6 of the same color (light blue). **B)** Analysis of gene expression of the sorbitol system for the same cells as in **A**. Fluorescence levels stay at the basal level, indicating a suppression of sorbitol expression. Colors were chosen for better discrimination between different plots. Figure adapted from [62] with permission from John Wiley & Sons, Inc.

Interestingly, this obvious dominance of the NAG over the sorbitol utilization system was no longer observed when cells were shifted to sugar mixtures containing a lower concentration of NAG (Fig. 6.9A). At 2 µM NAG and several concentrations of sorbitol, all cells still expressed the NAG system (Fig. 6.9A), giving rise to the unimodal behavior described before. At the same time, the same cells showed a bimodal expression pattern of the sorbitol system (Fig. 6.9B). Thus, each system displayed the same expression behavior as in the absence of the second sugar (see Fig. 6.6). Overall, cells showing co-expression of both sugar utilization systems and cells exclusively expressing the NAG system were found next to each other. However, no cells could be identified that only expressed the sorbitol system. Remarkably, this regime of co-expression of the genes of the NAG and of the sorbitol system persisted over three orders of magnitude of sorbitol concentration, from 2 µM to 200 µM external sorbitol concentration.

Exemplary images taken on the microscope for 2 µM NAG in combination with 20 µM sorbitol are shown in Fig. 6.10. The bright field image in Fig. 6.10A displays single cells during growth, as nearby daughter cells can be identified. Fig. 6.10B shows the same cells in fluorescence illumination filtered to excite mCerulean. Here, all cells which can be seen

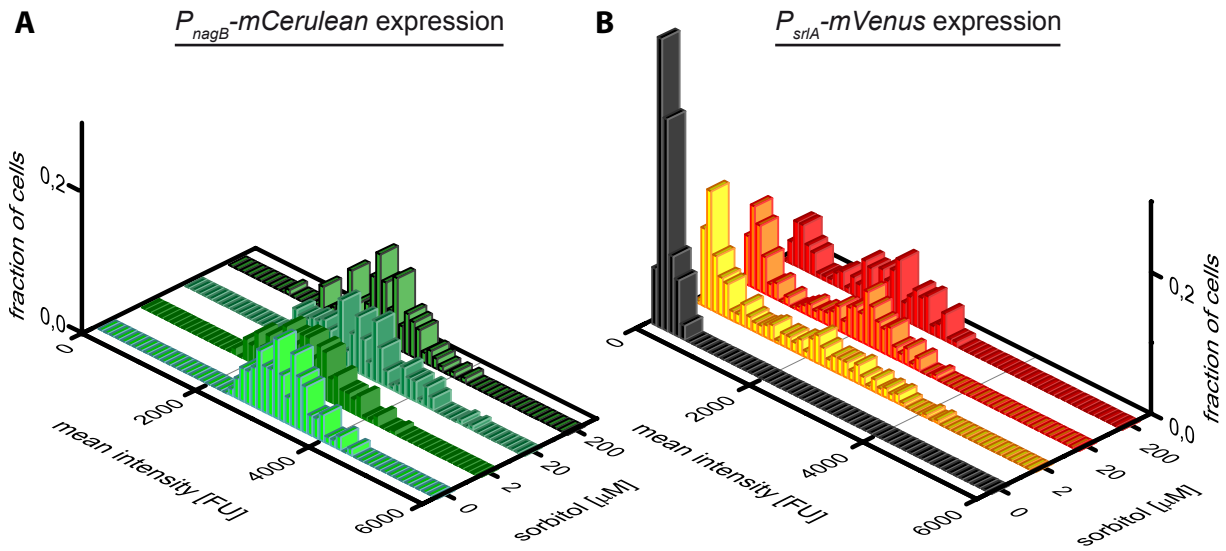

Figure 6.9.: Gene expression of the NAG and of the sorbitol system for 2 µM NAG and several concentrations of sorbitol.
A) Gene expression of the NAG system in cells grown on 2 µM NAG and different concentrations of sorbitol, as indicated, was measured 120 min after induction. A unimodal response can be observed for all concentrations tested. **B)** In the same populations as in **A**, gene expression of the sorbitol system 120 min after induction is bimodal. Scale bar: 2 µm. Colors were chosen for better discrimination between different plots. Figure adapted from [62] with permission from John Wiley & Sons, Inc.

in the bright field image appear as well, due to unimodal gene expression, and are colored in blue. Again the same cells have been imaged in fluorescence illumination filtered to excite mVenus in Fig. 6.10C. Here, cells are depicted in yellow, but as not all cells express the sorbitol system, the intensity of different cells varies. The red frame emphasizes 4 cells in close proximity, which clearly show similar expression levels in *mCerulean* but heterogeneous expression levels in *mVenus*. To illustrate co-expression in single cells, an overlay of the bright field and the fluorescence images is shown in Fig. 6.10D. Here, all cells co-expressing both systems appear green.

6.5. Experimental phase diagram of gene expression

All measurements of gene expression of the NAG and of the sorbitol utilization system are combined in an experimental phase diagram in Fig. 6.11. The behavior of the population is shown schematically for each combination of concentrations by the help of one ellipse, which is divided into 2 parts. The left half represents the sorbitol system and the right half represents the NAG system. The experimental phase diagram gives an overview over the metabolic preferences subject to the different combinations of NAG and sorbitol tested and reveals two qualitatively different phenotypic responses: one of hierarchical gene expression (blue area in Fig. 6.11) and one of simultaneous co-expression (gray area in Fig. 6.11).

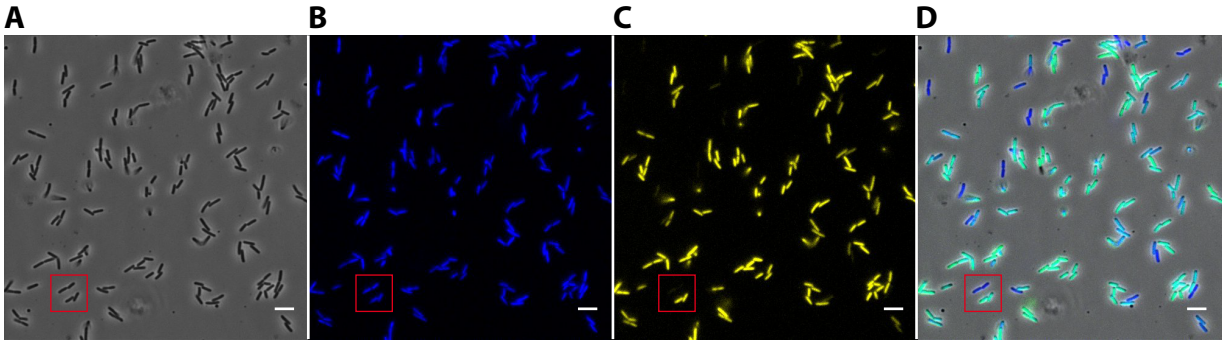

Figure 6.10.: Single cells 120 min after induction with 2 µM NAG and 20 µM sorbitol.
Single cells are shown **A)** in bright field illumination, **B)** in fluorescence illumination filtered for the expression of *mCerulean*, **C)** filtered for the expression of *mVenus*, and **D)** in an overlay of the first three. While all cells express the NAG system, a significant number of cells does not express the sorbitol system (see red frame for exemplary cells). Scale bar: 5 µm.

The former response is apparent at saturating concentrations of the dominant sugar NAG. Here, the available carbohydrates NAG and sorbitol are consumed in a sequential manner starting with NAG, irrespective of the concentration of the second available carbon source sorbitol. The later response of co-expression can be observed for lower concentrations of the dominant sugar NAG when a subset of the cells induces the sorbitol utilization system, i.e. the less preferred carbon source's utilization system, in addition to the induction of the NAG utilization system.

6.6. Deterministic model for flux-limited regulation

To get an idea of the regulatory principle, which might underlie the observed behavior of co-expression at low NAG concentrations and the transition to hierarchical gene expression at high NAG concentrations, a mathematical model, inspired by a previously published deterministic model for the PTS by Thattai and Shraiman [16], was established. Only the basic features of the sugar utilization systems were included into the coarse-grained modeling approach as the total set of enzymatic reactions and interactions in the PTS has not been quantitatively characterized up to date, which would be necessary to derive a detailed mathematical model. These most relevant features are the positive feedback of gene expression onto itself, the coupling of the sugar uptake to the phosphoryl flux, and the competition for phosphoryl flux between the systems.
In the following, deterministic differential equations are derived, which describe the dynamics of the protein expression levels of the NAG and of the sorbitol system, as well as the dynamics of the internal concentrations of the substrates NAG and sorbitol. The fixation of some of the parameters to values which were extracted from experimental data is explained and a simulated phase diagram is introduced and compared to the experimental

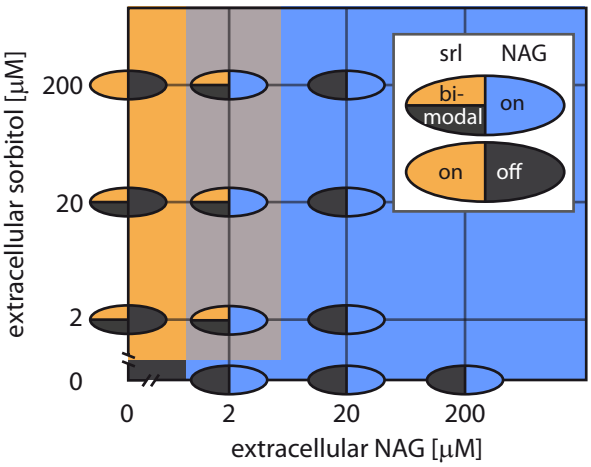

Figure 6.11.: Experimental phase diagram of gene expression of the NAG and of the sorbitol system for several combinations of these substrates.
External sorbitol concentration is plotted against external NAG concentration. At each combination of concentrations, the behavior of the cells is shown schematically by one cell representing the whole population: The left half of each ellipse represents the state of the sorbitol system and the right half that of the NAG system. The color code is: black = expression only at basal level, blue = induction of the NAG system, orange = induction of the sorbitol system (mostly bimodal). Two qualitatively different phenotypical responses are found: sole expression of the NAG system in the hierarchical regime (blue area) for 20 μM extracellular NAG and co-expression of both utilization systems (gray area) in the co-expression regime at 2 μM extracellular NAG. Figure taken from [62] is reprinted with permission from John Wiley & Sons, Inc.

one.

6.6.1. Derivation of the rate equations

In the context of this work, a theory was developed in collaboration with J. Gutiérrez, G. Fritz and U. Gerland in order to describe the dynamics of protein expression and substrate concentration levels for NAG and sorbitol inside a cell. Deterministic differential equations were devised to reflect the positive, autocatalytic feedback loops inherent in both systems due to the regulatory effect of intracellular substrate on the expression of the corresponding system (see Fig. 6.1) [98, 99]. Competition of the two sugar transport systems for limited phosphoryl flux, J_{max}, was introduced in a way that a high uptake rate of one sugar immediately reduces the effective import rate of the second sugar.

First, some details concerning the EII complexes in both systems have to be considered to derive rate equations describing the dynamics of the metabolic enzymes for the NAG and the sorbitol system. In the NAG system, the EII^{NAG} complex is transcribed from the gene *nagE*, which possesses all three domains (IIC-IIB-IIA) required for NAG transport in one single polypeptide chain [116]. In the sorbitol system, the EII^{srl} complex is transcribed

from separate genes, *srlA* for IIC, *srlE* for IIB, and *srlB* for IIA [98]. These genes are all organized in one single operon, allowing correlated expression of all EII^{srl} subunits. Due to the correlation of expression of all subunits in the NAG and in the sorbitol system, one free variable ϵ_i is considered to describe the protein level of the EII complex for each system. The subscript $i = 1, 2$ stands for NAG and sorbitol, respectively.
Then, the time evolution of the protein expression levels is described by

$$\frac{d\epsilon_i}{dt} = \nu_i + \alpha_i \frac{(S_i^{int})^{h_i}}{(K_i)^{h_i} + (S_i^{int})^{h_i}} - \epsilon_i \tag{6.2}$$

with three contributions: the constant basal rate of protein production, ν_i, reflecting the leakiness of the promoter in the absence of the inducer, active protein synthesis in the presence of intracellular sugar S_i^{int}, described by a Hill function with maximal expression rate α_i, with Hill coefficient h_i, and with internal sugar binding constant K_i, and finally protein dilution. As time is normalized to units of cell doubling time, this dilution in the last term has been set to unity.
Then, the intracellular level of substrate S_i^{int} increases with the level of uptake proteins ϵ_i as well as the uptake rate of these importers and decreases due to dilution. Active degradation has not been considered in the model, because it would only contribute as a constant factor to the dilution rate. To model the import of sugar accomplished by the EII complexes, transport according to Michaelis-Menten kinetics with a maximal uptake rate per enzyme V_{max_i} and a Michaelis-Menten constant K_{M_i} is assumed. However, to embed the effect of phosphoryl flux limitation into the dynamics of internal sugar levels, the uptake rate is reduced by a modulation factor γ, leading to the following equation

$$\frac{dS_i^{int}}{dt} = \epsilon_i V_{max_i} \frac{S_i^{ext}}{K_{M_i} + S_i^{ext}} \gamma(S_1^{ext}, S_2^{ext}, \epsilon_1, \epsilon_2) - S_i^{int}, \tag{6.3}$$

where S_i^{ext} is the external concentration of sugar i. The higher the uptake rates, the more pronounced should phosphoryl limitation within the PTS be, because each import of one sugar molecule dissipates one phosphoryl group. That is why the flux-limitation factor γ should depend on the overall phosphoryl demand given by the individual phosphoryl demand of each active system within the PTS. As it is a factor meant to measure relative limitation, γ should be a saturating function taking values between zero and one, for absolute and no limitation, respectively. Thus, the unregulated Michaelis-Menten uptake rates of the import enzymes were chosen to designate the phosphoryl demand from each sugar-specific system. In consequence, γ takes the form

$$\gamma(S_1^{ext}, S_2^{ext}, \epsilon_1, \epsilon_2) = \frac{J_{max}}{J_{max} + \epsilon_1 V_{max1} \frac{S_1^{ext}}{K_{M_1} + S_1^{ext}} + \epsilon_2 V_{max2} \frac{S_2^{ext}}{K_{M_2} + S_2^{ext}}} \tag{6.4}$$

with the normalization constant J_{max} describing the maximal phosphoryl flux through the PTS. Effectively, J_{max} operates as a threshold to approach flux limitation: As long as the demand for phosphoryl flux given by the sum of the Michaelis-Menten terms of both

systems stays much smaller than J_{max}, the flux-limitation factor γ is approximately unity and does not play a role in Eq. 6.3. Hence, the two systems transport their substrates independently of each other. However, once the demand for phosphoryl flux reaches the order of J_{max} or even higher values, γ drops below one and becomes non-negligible. Then, sugar uptake rates in Eq. 6.3 will be reduced.

6.6.2. Choice of parameters

The model consisting of the coupled differential equations Eq. 6.2 and Eq. 6.3 contains several free parameters. In order to restrict the model to a physiologically meaningful regime, some parameters were fixed to values determined in accordance with the experimental data. For a summary of all parameters, see Appendix A.5. In the following, the choices made are explained in detail.

Relative maximal gene expression α compared to basal gene expression ν was estimated by the expression patterns in Fig. 6.6. The expression patterns of the NAG and of the sorbitol system both revealed that the maximal protein expression is eightfold higher than the basal expression. Accordingly, due to normalization of the maximal and basal expression rate to $\nu_i + \alpha_i = 1$, the basal expression rate in both systems was set to $\nu_i = 0.125$ and the maximal expression rate was set to $\alpha_i = 0.875$.

The internal sugar binding constant K_i and the Hill coefficient h_i, both parameters describing the induction process, were chosen such that predictions of the model for the single sugar case $S_i^{ext} = 0$, $S_j^{ext} = 0$ $(i, j \in \{1, 2\}, i \neq j)$ match with the actual observations found experimentally in Fig. 6.6. The Hill coefficients h_i were assumed to be greater than 1, based on the consideration that cooperative interactions are likely to be involved in the regulation of the NAG and of the sorbitol promoter. For instance, a Hill coefficient of $h_{NAG} = 2$ is already sufficient to describe the unimodal, phenotypic response of the NAG utilization system, while a coefficient of $h_{srl} \geq 4$ is required to reproduce the bimodal induction pattern of the sorbitol system.

These differences in the cooperativities between the NAG and the sorbitol system might originate from their regulatory networks. Although the precise interactions of the regulators with their cognate targets are not well understood to date, it is known that NagC, when bound to its two operators at the same time, forms a DNA loop [99]. The sorbitol system comprises two regulators, which are both encoded in the *srl* operon: a sorbitol-dependent repressor SrlR and a sorbitol-independent activator GutM. These two regulators possibly compete for a single binding site in the operator region of P_{srlA} [98]. Additionally, it was suggested that SrlR occupies the operator site in the absence of sorbitol but is released in its presence, which is when GutM will be up-regulated and starts a positive feedback facilitating further high-level expression of the *gut* operon [98]. Besides, based on sequence similarities in the DNA-binding domains of *gutM* and *gutR* with other, oligomeric DNA-binding proteins, an oligomerization of both proteins was suggested to be required

for interactions with the DNA [98]. The combination of this competitive binding of SrlR and GutM to P_{srlA} and of positive feedback possibly explains the higher cooperativity in the sorbitol system than in the NAG system. Both regulatory principles are known to increase the sensitivity of regulatory elements towards their inputs [44, 45].
The next free parameters to examine are the ones characterizing the import kinetics of Michaelis-Menten type in Eq. 6.3, K_{M_i} and V_{max_i}. For an estimation of the Michaelis-Menten constants K_{M_i}, the values for K_M^{NAG} and K_M^{srl} were taken, which were obtained by fitting the hyperbolic Monod function to the data of growth under carbon limited conditions (see Fig. 6.5 and Eq. 6.1). This choice seems justifiable as these fitted values are likely to reflect the affinities of the import proteins for their respective substrate as mentioned before in Section 6.3. In turn, the maximal sugar uptake rates V_{max_i} were set to physiologically reasonable values. These lumped parameters were modulated in a way that the obtained intracellular sugar concentration reaches a level which is typical for other sugar utilization systems [84].

6.6.3. Simulated phase diagram

For a detailed analysis of the model, the steady-state case is considered. If cells have been grown under constant conditions for a sufficiently long period of time, the assumption of steady-state is reasonable. Then, the non-linear steady-state equations were solved numerically for several prominent values of J_{max} to construct computational phase diagrams for comparison with the experimental phase diagram in Fig. 6.11.
In steady-state, Eq. 6.2 and Eq. 6.3 take the form

$$\epsilon_i = \nu_i + \alpha_i \frac{(S_i^{int})^{h_i}}{(K_i)^{h_i} + (S_i^{int})^{h_i}} \tag{6.5}$$

and

$$S_i^{int} = \epsilon_i V_{max_i} \frac{S_i^{ext}}{K_{M_i} + S_i^{ext}} \gamma(S_1^{ext}, S_2^{ext}, \epsilon_1, \epsilon_2) \tag{6.6}$$

with enzyme concentrations ϵ_i in the interval $[\nu_i, 1]$ due to normalization to $1 = \epsilon_i^{max} = \nu_i + \alpha_i$. Eq. 6.5 and Eq. 6.6 together with Eq. 6.4 were solved numerically with the $MATLAB^{TM}$ routine *fsolve*. This routine was extended to analyze all fixed points which are located within the relevant dynamic range of the system, i.e. by analyzing the convergence of the set of possible initial conditions. Thereto, most parameters were fixed to values which were experimentally measured or to physiologically reliable values found in the literature as explained before (see Appendix A.5).

Variation of J_{max} in a range of 100 mM/(cell generation) (mM/cg) to 0.1 mM/cg results in quite different phase diagram characteristics. Starting with the highest value, corresponding to non-limiting conditions, undisturbed expression of both sugar utilization systems

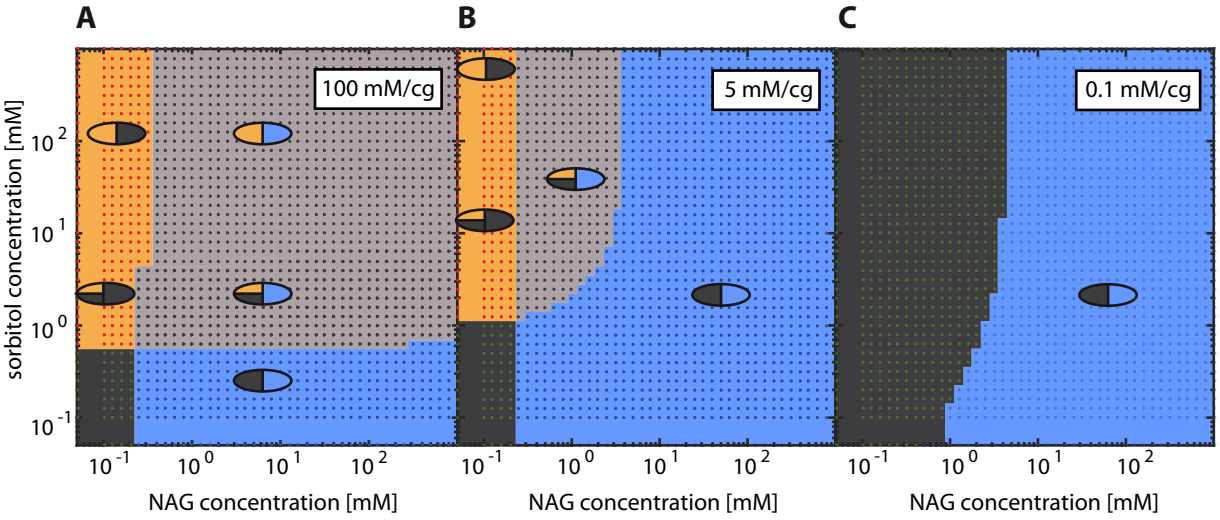

Figure 6.12.: Simulated phase diagram of gene expression of the NAG and of the sorbitol system for various values of J_{max}.
Each point represents the simulated expression state of the NAG and of the sorbitol system. For purposes of visualization, areas of the same phenotypes are highlighted in the same color and are schematically labeled with the same symbols as in Fig. 6.11.
A) For high values of $J_{max} = 100\,\mathrm{mM/cg}$, both systems are always expressed above their particular induction threshold and co-expression is observed. **B)** For lower values of $J_{max} = 5\,\mathrm{mM/cg}$, the sorbitol system is fully expressed at low NAG concentrations. At intermediate NAG concentrations, both systems are co-expressed. At high NAG concentrations, the NAG system suppresses the sorbitol system. **C)** For very low values of $J_{max} = 0.1\,\mathrm{mM/cg}$, the sorbitol system becomes fully suppressed and phosphoryl supply is even limiting for the fitter NAG system at low NAG concentrations. Figure taken from [62] is reprinted with permission from John Wiley & Sons, Inc.

was found, just as in the absence of the other sugar (Fig. 6.12A). No interaction between the systems could be detected. Switching from the OFF to the ON state was observed at 0.2 µM NAG for the NAG system. The sorbitol system switched at 0.5 µM sorbitol from the OFF state to a bimodal state with one part of the cells being ON and the other part staying in the OFF state. In the model, this qualitative difference develops from the differences in the strength of the positive feedback regulations: Stronger cooperativity in the sorbitol system (Hill coefficient $h_{srl} = 4$) than in the NAG system (Hill coefficient $h_{NAG} = 2$) leads to bimodal behavior. Overall, the model predicts co-expression of both sugar utilization systems for non-limiting flux conditions.
This co-expression pattern changed significantly when J_{max} was lowered by a factor of 20 to $J_{max} = 5\,\mathrm{mM/cg}$ (see Fig. 6.12B). At this lower phosphoryl flux, competition could be detected within the expression behavior most prominently at high NAG concentrations where the demand for phosphoryl is also high. Here, the model predicts a winner-take-all mode of behavior due to asymmetries in the rates of sugar uptake and of gene expression. In this winner-take-all mode, the NAG system is always in the ON state - even in a

concentration regime of external NAG in which the sorbitol system is in the bimodal ON state under non-limiting flux conditions (Fig. 6.12B; blue area). However, for lower NAG concentrations, this winner-take-all regime merges into a regime where both systems show co-expression (Fig. 6.12 gray area), similar to the experimental phase diagram in Fig. 6.11. Thus, within the model, the phosphoryl demand for uptake of both systems stays below the threshold J_{max} and competition begins when the total demand reaches the level of J_{max}. Interestingly, within the co-expression regime, even an increase in sorbitol levels to very high concentrations (10 mM) does not lead to efficient competition with the NAG system, a behavior which can also be seen in the experimental phase diagram (Fig. 6.11). The model explains this behavior by the saturation of the sorbitol transporters already at low substrate levels. Once the transporters operate at their effective uptake rate, they are not affected by a further increase in the external sorbitol concentration. Then, the demand for phosphoryl flux by the sorbitol system stays under the threshold for flux limitation and NAG can still be imported even at high sorbitol concentrations.
If J_{max} is further reduced, the co-expression regime will continue shrinking. Finally, the sorbitol system is totally suppressed at conditions of extremely limited phosphoryl flux ($J_{max} = 0.1\,\mathrm{mM/cg}$) and even the NAG system is found in the OFF state at low concentrations of external NAG (Fig. 6.12C).

6.6.4. Comparison of simulated and experimental phase diagram

Overall, the metabolic phase diagram simulated for $J_{max} = 5\,\mathrm{mM/cg}$ in Fig. 6.12B shows a striking resemblance with the experimental phase diagram in Fig. 6.11. In both diagrams, co-expression of the NAG and the sorbitol system is found for low concentrations of external NAG in combination with a broad range of external sorbitol concentrations. Furthermore, experiment and theory both reveal a regime of distinct dominance of the NAG system. At high NAG concentrations, the NAG utilization system is fully expressed, while the sorbitol system stays at the basal expression level. The precise value of J_{max} which reproduces the experimental phase diagram should not be over-interpreted. However, analysis of the effect of J_{max} within the model pointed out the prospects of such a parameter, which can serve as an important threshold for total phosphoryl flux. By tuning this threshold, a cell could in principle control metabolic switching between competing sugar utilization systems.

6.6.5. Distinctiveness of the model

As mentioned before, the model introduced in the last section was based on a previously published model by Thattai and Shraiman (TS model) [16]. Nevertheless, the model presented here differs in some key aspects from the TS model, more precisely in the integration of operon induction and phosphoryl demand.
First, operon induction, which is the increase of operon activity dependent on the intra-

cellular substrate concentration, is modeled by a Hill function here in contrast to the TS model, which considers a linear increase of the protein expression with the internal sugar concentration. The linear correlation was argued to arise from the fact that only low saturation levels of intracellular substrate should accumulate in the cell due to the rate-limiting step of re-phosphorylation of the sugar-specific PTS branches. However, this assumption might no longer be true in a regime of subsaturating external sugar concentrations. Then, due to the low availability of the sugar, the rate-limiting step might rather be the binding and translocation of the carbohydrate than the re-phosphorylation.
Second, the concentration of sugar-specific PTS enzymes quadratically contributes to the phosphoryl demand in the TS model. This correlation was argued to arise due to parallel expression of cytoplasmic EIIA and membrane-bound EIIBC, two subunits which are usually transcribed from the same operon leading to similar intracellular concentrations. However, there are PTSs where the EIIA and EIIBC subunits form a single polypeptide, as in the NAG system [116]. To gain generality, the phosphoryl demand of the sugar-specific PTS parts is therefore treated as Michaelis-Menten kinetics, which describes the unregulated uptake rate of the membrane-bound import enzymes.

6.7. Discussion

The analysis of phosphoryl flux-limited competition between the NAG and the sorbitol system, which was presented in this Chapter, has uncovered two distinct phenotypic responses: mixed expression of both systems and exclusive expression of the dominant NAG system. These responses were observed for several mixtures of the substrates NAG and sorbitol. While high concentration of external NAG triggered a hierarchical winner-take-all usage of this substrate, low concentration of external NAG led to stochastic co-utilization of NAG and sorbitol, a behavior which even prevailed when sorbitol was present at a saturating level. This saturating level was determined by growth studies under controlled microfluidic conditions where growth was measured in dependence of the constant concentration of external substrate. The concentration-dependent growth has a sigmoidal shape and reaches maximal growth for saturating concentrations of external sugar. The transition between exclusive expression and co-expression takes place at a concentration of external NAG, which no longer shows maximal growth for NAG when it is the single source of energy.
The behavior observed experimentally was reproduced by a deterministic mathematical model in the next step. This model incorporates the following features: induction via a Hill function, sugar uptake via Michaelis-Menten kinetics, and global competition for phosphoryl supply via a competition factor. In this factor γ, the maximal phosphoryl flux through the PTS, J_{max}, plays a dominant role, as the model reveals that the metabolic switch between the two utilization strategies (hierarchical expression and co-expression) depends on the supply situation by phosphoryl flux. When this supply is limiting, at low

J_{max}, only the dominant system gains phosphoryl groups which is manifested in the hierarchical usage. For excessive phosphoryl supply, at high J_{max}, several systems can satisfy their demand for phosphoryl groups, which leads to co-utilization.
Within the model, the apparent dominance of NAG utilization over sorbitol utilization in the presence of certain combinations of NAG and sorbitol concentrations was implemented through an asymmetry in the transport rates of the EII^{NAG} and EII^{srl} transporters and in the Michealis-Menten constants. The Michaelis-Menten constants were obtained from concentration dependent growth measurements. Such an asymmetry is plausible, since NAG and sorbitol belong to two different PTS families; hence, the EIIA domains of the two transporters differ significantly in their tertiary structure, while fulfilling the same function of phosphoryl transfer from HPr to EIIB [117]. It has been suggested that these differences in the mechanism of stabilizing the HPr-EIIA complex, and thus in their binding affinity, might be part of the complex mechanisms that control the hierarchical usage of carbohydrates [117].

Due to a lack of quantitative experimental information, the model does not explicitly account for the feedback from carbohydrate uptake and metabolism on J_{max}. Instead, the competition between the PTS sugar utilization systems was analyzed as a function of a tunable maximal phosphoryl flux through the PTS. However, changes in the PEP to pyruvate ratio, which correlates with metabolism, are known to affect the phosphorylation state of the PTS proteins [118, 119]. Thus, on a molecular level, it can be assumed that the PEP to pyruvate ratio determines J_{max}, as suggested previously [16]. Depending on the growth conditions, the PEP to pyruvate ratio varies with taking its highest values for nutrient poor environments [94, 118, 119, 120]. By our model, changes in J_{max} are predicted to shift the boundary between the hierarchical and the co-utilization regime. Indeed, starving cells, which have a high PEP to pyruvate ratio, were found to be able to co-utilize various sugars [94]. Similarly, co-utilization of multiple carbon sources seems to be a common strategy during growth on the low sugar concentrations often encountered in natural environments [121].

Thus, our model suggests that the maximal phosphoryl flux through the PTS could play a dominant role in the adaptation process of a cell's carbon utilization strategy in response to its present metabolic status. Of course, this adaptation is also regulated by other, well-described global regulation mechanisms such as the second messenger cAMP. The concentration of cAMP increases under carbon limitation and stimulates the basal expression of many carbon utilization systems via its receptor protein CRP [112]. Accordingly, the basal expression of P_{srlA} and P_{nagB} is also increased by cAMP-CRP under carbon limitation [98, 104]. Then, at a higher basal expression, induction of both systems upon inducer addition is facilitated, which suggests that bacteria use a dual strategy to adapt to carbon-limiting environmental conditions: On the one hand, an increased PEP to pyruvate ratio mitigates the shortage of phosphoryl flux through the core PTS and

thereby *permits* the co-expression of PTS utilization systems, while on the other hand an increased cAMP-CRP level rises the basal expression of all PTS systems and thereby *facilitates* co-utilization of multiple carbon sources.

7. Outlook

In this work, we analyzed ON and OFF processes of gene regulation in several sugar utilization systems by observing changes in gene expression after a switch of the concentration of the external sugar.
In the PTS, we found two different utilization strategies, a co-utilization and a hierarchical winner-take-all strategy. From the physiological perspective, both metabolic regulation strategies may be beneficial, depending on the environmental context. In times of feast, the maximization of the instantaneous growth rate should result in a selective advantage, which can be achieved by primary usage of the highest quality nutrient on offer [35, 122]. Contrarily, during times of famine, i. e. upon depletion of nutrients, selective advantages may arise if cells can gather all the remaining nutrients available in their environment [123]. Based on our results, we suggest that flux limitation in the PTS serves as an efficient and economical way of adapting the cells' metabolic strategy to prevailing mixed substrate conditions without the need for multitudinous regulatory interactions. Similarly, recent work has also suggested that intracellular metabolic fluxes could play an important regulatory role [13, 14, 15, 58].

While already insight on metabolic strategies could be gained by analyzing the phase-diagram of gene expression taken 120 minutes after the change of external nutrients, such a diagram is only a snapshot of a the dynamic process of metabolic adaptation. Thus, in the future, experimental time-lapse studies of metabolic switching in the PTS might unravel potential correlations in the timing of switching in a co-utilization case. Equally, the integration of temporal fluctuations of external conditions into the deterministic mathematical model could allow for the prediction of dynamic changes as it was recently presented in a dynamic optimization framework [124].

In the single sugar case of the arabinose utilization system, we analyzed the dynamics of gene expression after a removal of external sugar. We found fast shutdown of gene expression of the arabinose system, but could not identify the exact mechanism of internal sugar depletion. Thus, we suggest that sugar is either degraded by non-arabinose affiliated proteins or by export via AraE or by export systems, which are not part of the arabinose utilization system like members of the major facilitator superfamily [91]. In general, export mechanisms are thought to be crucial to get rid of toxic substrates or toxic amounts of harmless substrates[86, 87]. If export or more general, internal depletion, was a global mechanism, downshift studies in the PTS should also unravel fast shutdown of

gene expression.

In quickly fluctuating environments, the role of fast internal depletion can be questioned. Fast shutdown of gene expression of metabolic genes after external removal of the correspondent sugar helps to be prepared for investing energy and resources in the gene expression of metabolic genes of a new sugar source. In the case of fast fluctuations of one single sugar, this sugar can still be taken up and metabolized after the shutdown of gene expression due to the long lifetime of the stable proteins. Thus, a heterogeneous distribution of response times in the population is not necessary to spread survival chances.
In fluctuating environments however, memorizing recent sugar sources might be beneficial. Not long ago, two strategies of memory have been identified for the lactose system: phenotypic memory and responsive memory [125]. While responsive memory is described as a hysteretic behavior of persisting gene expression after removal of the inducer and enhances adaptation in short fluctuations faster than one generation, phenotypic memory is specified as the transmission of stable intracellular proteins, which reduce the lag phases after glucose consumption in cyclical fluctuations on the timescale of 1-10 generations [125]. How would such memory function interfere with regulation by flux-limitation as in the PTS? Perhaps, further switching strategies can be found on top of the hierarchical winner-take-all and the co-utilization strategy described here.

Recently, *E. coli* was successfully modified such that the diauxie between xylose and arabinose was eliminated and in consequence, the cells produce ethanol from hemicellulose sugars with much higher efficiency [126]. Another hemicellulose sugar, mannose, is part of the PTS [96]. As hemicellulosic biomass, one of the most abundant renewable biomass sources, consists of several different sugars, simultaneous conversion of all those sugars is the goal of the design of whole-cell biocatalysts. A deeper understanding of the principles underlying cross-regulation of sugar utilization systems such as in the PTS, is an important step towards this goal.
Altogether, the study presented here sheds new light on cellular decision-making in sugar utilization systems, and our findings might prove useful for optimization of the utilization of mixed carbon sources by industrial strains.

A. Appendix

A.1. Bacterial strains used in this work

strain	**characterization**	see
E. coli		
MG1655	wild type with native arabinose system	Chap. 4
BW25113	$\Delta araBAD$, native *araJ*	Chap. 4
JW0386-1	$\Delta araBAD$, $\Delta araJ$	Chap. 4
S3840	= MG1655	
T1064	= S3840 *nagBACD-norR-intergenic::* *(Frt-kanR-Frt* $P_{nagBACD}$ $SD_{10\epsilon}$-*mVenus*λtL3) wild type with *mVenus* under P_{nagB} integrated in the chromosome	A.4
T1682	= S3840 nag::KD3CmR_P_{nagB}-eSD-mCerulean(HB1) wild type with *mCerulean* under P_{nagB} integrated on the chromosome	A.4
T1683	= S3840 gutQ-norR-intergenic::Frt-P_{srlA}-mVenus + nag::KD3CmR_P_{nagB}-eSD-mCerulean(HB1) wild type with *mVenus* under P_{srlA} and *mCerulean* under P_{nagB} integrated on the chromosome	Chap. 6
B. subtilis		
TMB1 172	*B. subtilis* from [127]	Chap. 3.4

Table A.1.: In this work, the different strains listed here are used. With the *E. coli* strains, three different utilization systems are investigated: the arabinose (ara), the NAG and the sorbitol utilization system. Here, the different strains are listed with a short characterization.

A.2. Diauxic growth on a mixture of glucose and NAG or sorbitol

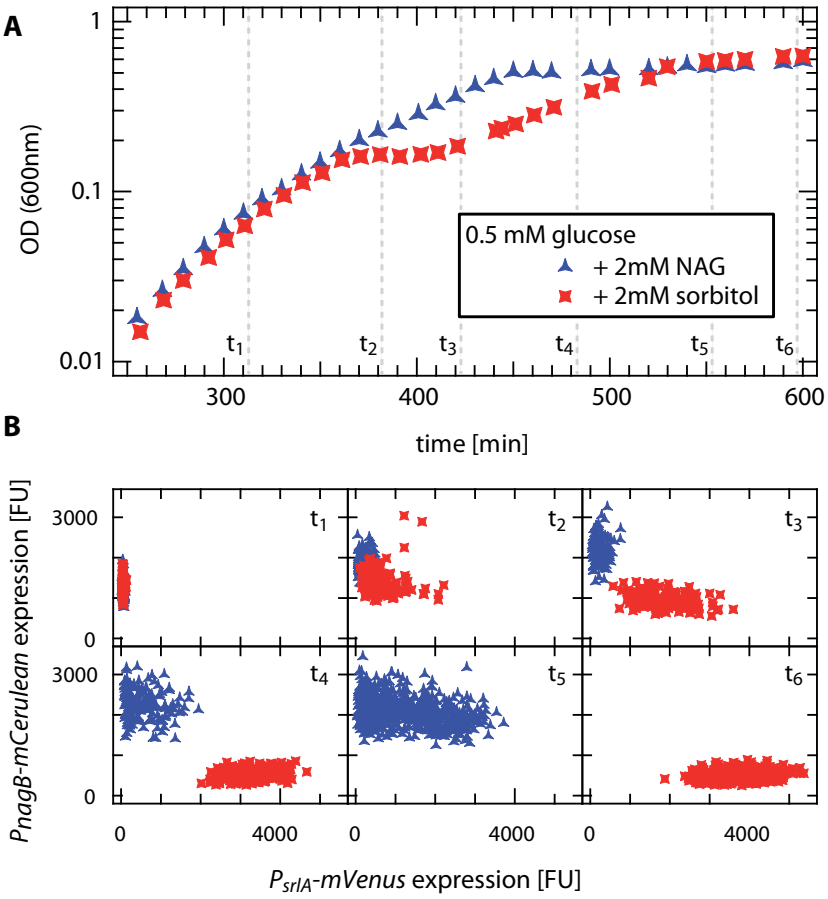

Figure A.1.: Growth on glucose in combination with NAG or sorbitol.
A) Growth measurements for bacteria cultured on 2 mM glucose with NAG (blue triangle) or with sorbitol (orange star). Until $t = 360$ min, both growth curves show similar slopes, indicating that growth is essentially fueled by glucose. In combination with sorbitol, clear diauxie is seen, in combination with NAG no lag phase is observable. This is in accordance with the fact that NAG belongs to the glucose family and similar growth rates have been reported on both sugars.
B) Gene expression of *PsrlA-mVenus* and *PnagB-mCerulean* was measured for single cells at several different time points as indicated by vertical lines in **A**. The start of expression of *PsrlA-mVenus* can be observed at t_2. At t_3 during the second exponential growth phase, high expression levels are reached (orange stars). For *PnagB-mCerulean*, the shift of expression values is less pronounced but also observable. At t_5, 100 min after reaching the final plateau of growth arrest, some cells express the sorbitol system although no sorbitol is present. Such behavior is an indication for starvation (regulated for example with cAMP, see Section 6.7).

A.3. Variation between replicate measurements of gene expression for 20 μM of NAG

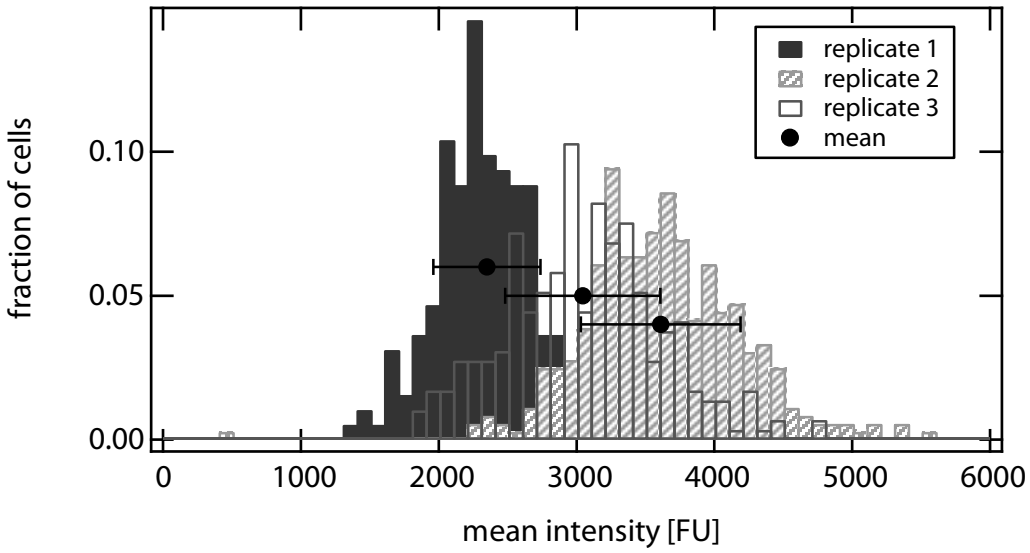

Figure A.2.: Day-to-day variation between replicate measurements.
Gene expression of $P_{nagB}-mCerulean$ was measured for 3 replicates on 3 different days. The concentration of external NAG was always 20 μM. Replicate 3 is identical to data of 20 μM in Fig. 6.6A. Mean and standard deviation is given for each replicate. These measurements show the normal day-to-day variation between replicates.

A.4. Influence of the different fluorescent proteins on gene expression

Integration of the genes of two different fluorescent proteins, *mCerulean* and *mVenus*, as reporters into the chromosome of a MG1655-based *E. coli* strain was done in a collaboration with K. Schnetz. To ensure that the measured results of gene expression patterns of NAG and sorbitol utilization systems are not hampered by the specific fluorescent reporters used for each system, expression of the NAG system was cross-checked in single-mutant strains containing either *mCerulean* (T1682) or *mVenus* (T1064) and compared with the results of the double-mutant strain (T1683) used for all further measurements (for further information on strains, see Appendix A.1).

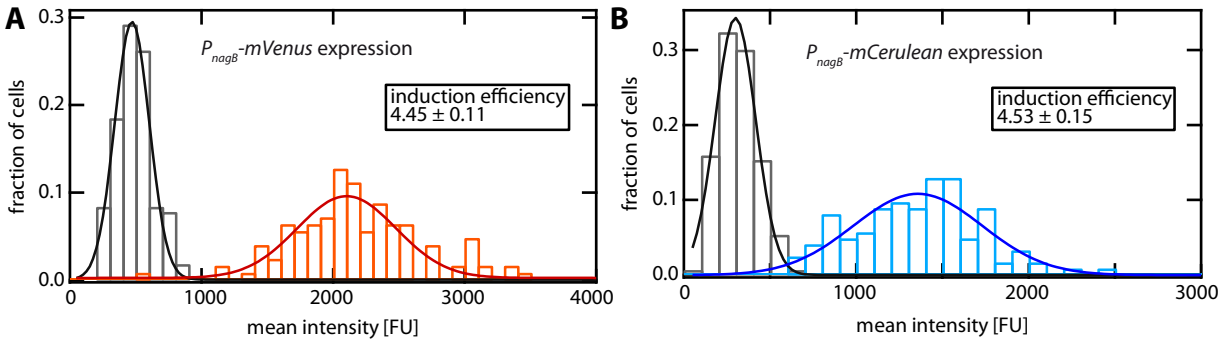

Figure A.3.: Comparison of P_{nagB} expression measured by the reporters *mVenus* and *mCerulean*.
A) Gene expression of P_{nagB}-*mVenus* in cells grown on 2 mM NAG for 45 min is shown in orange (strain T1064). **B.** Gene expression of P_{nagB}-*mCerulean* in cells grown on 2 mM NAG for 45 min is shown in blue (strain T1682).
Basal expression at time $t = 0$ min is always shown in black. Histograms are fitted by gaussians. The induction efficiency, which is the ratio of mean induced to mean basal fluorescence level, is identical for both fluorescence reporters within their standard deviations.

Gene expression of *mVenus* and *mCerulean*, both under the control of P_{nagB}, is depicted in Fig. A.3. While the absolute mean intensity of mVenus proteins is higher than the mean intensity of mCerulean proteins at basal expression (black data) as well as at induced expression (colored data), the ratio of induced to basal expression stays the same for both reporters. This induction efficiency is 4.45 ± 0.11 for P_{nagB}-*mVenus* and 4.53 ± 0.15 for P_{nagB}-*mCerulean*. In conclusion, the choice of the particular fluorescent protein does not measurably influence gene expression efficiency.

Next, it was tested whether differences in gene expression could be detected for the single reporter mutant (T1682) and a double reporter mutant (T1683), which carries P_{nagB}-*mCerulean* and P_{srlA}-*mVenus*. As can be seen in Fig. A.4, gene expression of P_{nagB}-*mCerulean* is very similar for both mutants. Thus, addition of a second reporter into

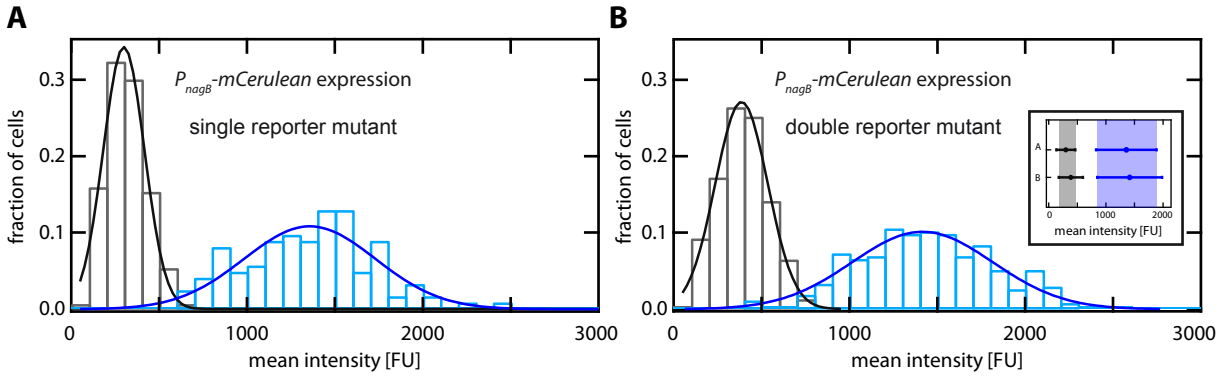

Figure A.4.: Comparison of P_{nagB} expression measured by the reporter mCerulean in a single and in a double reporter mutant.
A) Gene expression of P_{nagB}-*mCerulean* (strain T1682) and **B)** of P_{nagB}-*mCerulean* (strain T1683, which additionally carries a P_{srlA}-*mVenus* copy on its chromosome) in cells grown on 2 mM NAG for 45 min is shown in blue. Basal expression at time $t = 0$ min is always shown in black. Data is fitted by a Gaussian. The inlay illustrates that addition of the second reporter does not significantly change gene expression of P_{nagB}-*mCerulean* (mean and the standard deviation of **A** and **B**, colored areas are introduced to guide the eye).

the strain does not detectably influence expression of the first reporter under a different promoter.

A.5. Plasmids used in this study

Plasmids	Relevant features	Construction Reference
pBAD24gfp (*)	P_{BAD}-*GFPmut3*	[12]
pKD3	*Frt-cat-Frt oriR*γ *bla*	[128]
pKD13	*Frt-neo-Frt oriR*γ *bla*	[128]
pKES296	*PnagB SD10*$_{10\epsilon}$-*mVenus* in pKD13	A *PnagB* fragment was amplified with primers T391 and T400 and digested with SalI and EcoRI, and a *mVenus* fragment was amplified with primers T146 and T368 and digested with EcoRI and BamHI. Then, both fragments were cloned into the SalI+BamHI-digested plasmid pKD13.
pKES297	*PsrlA SD10*$_{10\epsilon}$-*mVenus* in pKD13	A *PsrlA* fragment was amplified with primers T401 and T402 and digested with SalI and EcoRI, and a *mVenus* fragment was amplified with primers T146 and T368 and digested with EcoRI and BamHI. Then, the two fragments were cloned into the SalI+BamHI-digested plasmid pKD13.
pKES323	*PnagB SD10* $_{10\epsilon}$-*mCerulean* in pKD13	The *mCerulean* fragment was amplified with primers T771 and T368, digested with NdeI and BamHI, and cloned into the NdeI+BamHI-digested plasmid pKES296.
pKES327	*PnagB SD10* $_{10\epsilon}$-*mCerulean* in pKD3	The *PnagB-mCerulean* SalI-BamHI fragment of plasmid pKES323 was cloned into the SalI+BamHI-digested plasmid pKD3.
pVS133	P_{lac}-*mVenus*	originally from Victor Surjik, Marburg
pKES316	P_{lac}-*mCerulean*	

Table A.2.: List of Plasmids used to produce the strains used in this work in collaboration with K. Schnetz, Köln, except (*) in collaboration with K. Jung, München.
Frt is the Flp recombinase target site, gene *neo* encodes kanamycin resistance, the *cat* gene encodes chloramphenicol resistance, the SD10$_{10\epsilon}$ enhanced ribosome binding site is derived from phage T7 gene 10 [129]. The plasmids pVS133 and pKES316 have been used to measure the maturation times of mVenus and mCerulean.

A.6. Oligonucleotides used in this study

Name	Sequence	Purpose
T146	ctgaagcttgctagctcgaggaattc*aataa ttttgtttaactttaagaaggagatatacat* ATGAGCAAGGGCGAGGAGC TG	Amplification of *mVenus* with $SD_{10\epsilon}$ (EcoRI)
T368	cgatggatccaattgtctagaTTACTT GTACAGCTCGTCCATGCC	Amplification of *mVenus* and *mCerulean* (BamHI)
T399	ctgagaattCTCAATAAGTAAAA TGTAAGCCGTTGG	Cloning of *nagBACD* promoter (EcoRI)
T400	ctgagtcgacTGTGAAAATTTAA TTCGTATCGCAAAT	Cloning of *nagBACD* promoter (SalI)
T401	tgacgaaTTCAGGATTTATTGT TTTATTACCAAACG	Cloning of *srlA* promoter (EcoRI)
T402	tcaggtcgacTCTGCATCACATT GTGCTGCG	Cloning of *srlA* promoter (SalI)
T543	gaggaattc*aataattttgtttaactttaaga aggagatatacat*ATGGTGAGCAA GGGCGAGG	Amplification of *mCerulean* with $SD_{10\epsilon}$ (EcoRI)
T771	tatacatATGGTCAGCAAGGGC GAGGAGCTATTTACCGGGG TGGTGCCCA	Amplification of *mCerulean* (NdeI)
T575	CGCATCAGGCAGTTTGGCG TTTGTCATCAGAGCCAACC AC**tcttcgtctgtttctactggtattggc**	Chromosomal integration of *PnagB-mCerulean*
T905	CGCATCAGGCAGTTTGGCG TTTGTCATCAGAGCCAACC AC**ttgtctagattacttgtacagctcgtcc**	Chromosomal integration of *PnagB-mCerulean*
T656	AATAAACCTGCAGGATTTC TATCAGGCCGGGATTATTT AA**gtgtaggctggagctgcttcg**	Chromosomal integration of *PsrlA-mVenus*
T566	CCTGCATCGGCTGGCGAAA CGTCTGGGATTGAAGGATT AA**tcttcgtctgtttctactggtattggc**	Chromosomal integration of *PsrlA-mVenus*

Table A.3.: List of Oligonucleotides used for the production of the PTS strains used in this work, collaboration with K. Schnetz, Köln. Taken from [62] with Permission from John Wiley & Sons, Inc.

Restriction sites are underlined, nucleotides in UPPER CASE match the template and genomic integration site. Nucleotides in **bold** lower case match the template plasmids pKES297 and pKES327, respectively. Nucleotides in lower case *italics* correspond to the enhanced Shine-Dalgarno sequence derived from phage T7 gene 10 [129].

A.7. Parameters used in the mathematical model for the arabinose system

parameter	value	origin	description
$\frac{log(2)}{\gamma}$	55 min for MG1655 56 min for BW25113 67 min for JW0386-1	measured experimentally for every strain	doubling time
V_{max}	2000 ara molecules /protein /min	estimated in [12]	arabinose uptake velocity
K_M	0.3 mM	fitted in narrow, physiological range [78]	Michaelis-Menten constant for arabinose uptake via AraE
K_a	50 µM	[85]	arabinose binding threshold
$\nu_{max,e}$	4.2 min^{-1}	inferred from [79]	maximal transcription rate of P_E
λ_e	0.347 min^{-1}	[79]	degradation rate of AraE mRNA
λ_g	0.116 min^{-1}	[130]	degradation rate of GFP mRNA
μ_e	10.4 min^{-1}	unknown; chosen to meet typical burst size of 30 [131]	translation rate of AraE
μ_g	3.5 min^{-1}	”	translation rate of GFP
τ_m	6.5 min	[12]	maturation time of GFP
τ_{bleach}	140 min	extracted from exponential fits to measured bleaching data	bleaching time of GFP
σ	0.01 RFU /area /protein	arbitrary	scaling factor for GFP concentration and fluorescence values

Table A.4.: List of parameters used for the mathematical modeling of switching of the arabinose (ara) system from the induced ON state into the uninduced OFF state.

A.8. Parameters used in the mathematical model for the PTS

parameter	NAG value	sorbitol value	origin	description
K_M[µM]	4.9 ± 3.4	0.5 ± 0.4	Fig. 6.5	Michaelis-Menten constant of sugar uptake
V_{max} [mM/cell generation]	5.0	3.5	adjusted to obtain physiologically reasonable concentrations of intracellular sugar, compared to the literature [84]	maximal sugar transport rate
h	2	4	adjusted to match switching behaviour in Fig. 6.6	Hill coefficient of promoter activity function
K [mM]	0.12	1.1	adjusted to match switching behaviour in Fig. 6.6	internal sugar binding constant
ν	0.125	0.125	fraction of basal/max expression in Fig. 6.6	normalized basal expression level
α	0.875	0.875	fraction of basal/max expression in Fig. 6.6	normalized maximal expression level

Table A.5.: List of parameters which are used to solve Eq. 6.2 and Eq. 6.3 in order to generate the theoretical phase diagram Fig. 6.12.

A.9. Protocols

Production of PA hydrogels
Mix acrylamid and bis-acrylamid in a ratio of 29:1 in a final concentration of 10 % in H_2O, ad 0.1 % of the radical starter ammonium peroxodisulfate (APS) and ad 0.1 % of tetramethylethylendiamine (TEMED), which will catalyze the polymerization process (v/v). After addition of TEMED, polymerization will start, which is why the solution quickly has to be pipetted into the mold. By covering the mold with a glass slide, dust pollution is avoided and a flat surface is generated. Let the solution fully polymerize for 2 hours. In solution, PA is genotoxic, when fully polymerized, it is no longer harmful for cells. By the help of tweezers, the hydrogels can easily be taken out of the mold when hardened. They can be stored in distilled H_2O until needed.

Production of PEGDA microstructures
Prepare thin layers (2 µm) of the PDMS molds (10:1 mixture of PDMS with curing agent) containing the desired structure of the walls. Cut the cured PDMS to the size of the ibidi channels: the PDMS should be slightly smaller in width but a little bit longer than the channels. Ensure that the small wall structures on the PDMS are open on both ends.
Pre-treat the sticky-Slide placed upside down with Argon plasma for 0.3 min at 3.0 power (Femto, diener electronic, Ebhausen, Germany) and immediately after bring the PDMS mold in contact with the ceiling of the slide. Working in a dust reduced environment would be preferable.
Mix PEGDA with 2 % of the photoinitiator 2-hydroxy-2- methylpropiophenone (Sigma-Aldrich, Munich, Germany) (v/v) in a small eppendorf tube and protect it from light by wrapping it in aluminium foil. To prepare the six channels of one sticky-Slide, 50 µl are enough. Flip the sticky-Slide back from upside down to the normal orientation and carefully put its uper and lower ends on raised holders (which can be cut from PDMS). The PDMS molds in the channels should not touch the ground in order to prevent detaching. Then, carefully place a drop of the PEGDA solution at the open wall structures. These empty structures in the PDMS will be filled with PEGDA by capillary force-induced flow. Flip the whole sticky-Slide upside down again and cure the polymer under UV light for 15 min. Carefully detach the PDMS molds and cure the PEGDA substrate further on over night at 50 °C.

A.10. Medium and chemicals

M63 Minimalmedium

The following recipe is taken from [132]:

For 1000 ml H_2O:	
KH_2PO_4	13.6 g
$(NH_4)_2SO_4$	2 g
$FeSO_4\,x\,7H_2O$	0.5 mg (1.8 µl from 1 M stock)
adjust pH to 7.0 with KOH	
autoclave	
add:	
1 ml $MgSO_4\,x\,7H_2O$ from 1 M stock (sterile)	
1 µg/ml thiamine from stock (1 mg/ml) (sterile)	
0.2 % caseinhydrolysate from 10 % stock (sterile)	
0.5 % glycerole (sterile) as carbon source	

Chemicals

H_2O bidest	Millipore, PureAqua
KH_2PO_4	Roth
$(NH_4)_2SO_4$	Roth
$FeSO_4\,x\,7H_2O$	Roth
$MgSO_4\,x\,7H_2O$	Roth
Agar	Roth
Agarose	Biozym
Caseinhydrolysate	Roth
Glycerol	Sigma-Aldrich
KOH	Roth
L(+)-Arabinose	Roth
LB-Medium (Lura/Miller)	Roth
Thiamine	Roth
Ampicillin	Roth
Chloramphenicol	AppliChem
Spectinomycin	Sigma-Aldrich
Glucose	Roth
NAG	Sigma-Aldrich
Sorbitol	Sigma-Aldrich

Acrylamide bis-Acrylamide	Sigma-Aldrich
TEMED	Roth
Silicone elastomer base and curing agent	Sylgard

List of publications

G. Fritz, J. A. Megerle, **S. A. Westermayer**, D. Brick, R. Heermann, K. Jung, J. O. Rädler, and U. Gerland. Single cell kinetics of phenotypic switching in the arabinose utilization system of *E. coli*. *PLoS One*, 9(2):e89532, 2014.

S. A. Westermayer, G. Fritz, J. Gutiérrez, J. A. Megerle, M. P. Weißl, K. Schnetz, U. Gerland, and J. O. Rädler. Single-cell characterization of metabolic switching in the sugar phosphotransferase system of *Escherichia coli*. *Mol Microbiol*, 100(3):472-485, 2016.

Bibliography

[1] S. Yoshida, K. Hiraga, T. Takehana, I. Taniguchi, H. Yamaji, Y. Maeda, K. Toyohara, K. Miyamoto, Y. Kimura, and K. Oda. A bacterium that degrades and assimilates poly(ethylene terephthalate). *Science*, 351(6278):1196–1199, 2016.

[2] P. Vinuselvi, M. K. Kim, S. K. Lee, and C. M. Ghim. Rewiring carbon catabolite repression for microbial cell factory. *BMB Rep*, 45(2):59–70, 2012.

[3] H. Kitano. Systems biology: A brief overview. *Science*, 295(5560):1662–1664, 2002.

[4] U. Alon. *An introduction to systems biology, Design principles of biological circuits.* Chapman & Hall/CRC, London, 2007.

[5] U. Alon. Biological networks: The tinkerer as an engineer. *Science*, 301(5641):1866–7, 2003.

[6] A. Raj and A. van Oudenaarden. Nature, nurture, or chance: Stochastic gene expression and its consequences. *Cell*, 135(2):216–26, 2008.

[7] A. Eldar and M. B. Elowitz. Functional roles for noise in genetic circuits. *Nature*, 467(7312):167–73, 2010.

[8] M. Acar, J. T. Mettetal, and A. van Oudenaarden. Stochastic switching as a survival strategy in fluctuating environments. *Nat Genet*, 40(4):471–5, 2008.

[9] V. Shahrezaei and P. S. Swain. The stochastic nature of biochemical networks. *Curr Opin Biotech*, 19(4):369–74, 2008.

[10] R. Y. Tsien. The green fluorescent protein. *Annu Rev Biochem*, 67:509–544, 1998.

[11] E. M. Ozbudak, M. Thattai, H. N. Lim, B. I. Shraiman, and A. v. Oudenaarden. Multistability in the lactose utilization network of *Escherichia coli*. *Nature*, 427:737–740, 2004.

[12] J. A. Megerle, G. Fritz, U. Gerland, K. Jung, and J. O. Rädler. Timing and dynamics of single cell gene expression in the arabinose utilization system. *Biophys J*, 95(4):2103–15, 2008.

[13] O. Kotte, J. B. Zaugg, and M. Heinemann. Bacterial adaptation through distributed sensing of metabolic fluxes. *Mol Syst Biol*, 6(355):1–9, 2010.

[14] D. H. E. W. Huberts, B. Niebel, and M. Heinemann. A flux-sensing mechanism could regulate the switch between respiration and fermentation. *Fems Yeast Res*, 12(2):118–128, 2012.

[15] K. Kochanowski, B. Volkmer, L. Gerosa, B. R. Haverkorn van Rijsewijk, A. Schmidt, and M. Heinemann. Functioning of a metabolic flux sensor in *Escherichia coli*. *Proc Natl Acad Sci USA*, 110(3):1130–1135, 2013.

[16] M. Thattai and B. I. Shraiman. Metabolic switching in the sugar phosphotransferase system of *Escherichia coli*. *Biophys J*, 85:744–754, 2003.

[17] M. T. Madigan, J. M. Martinko, D. A. Stahl, and D. P. Clark. *Brock Mikrobiologie*. Pearson Education, Inc., Upper Saddle River, N. J., 13th edition, 2013.

[18] S. N. Chatterjee and K. Chaudhuri. *Outer Membrane Vesicles of Bacteria*. SpringerBriefs in Microbiology, 2012.

[19] K. Colville, N. Tompkins, A. D. Rutenberg, and M. H. Jericho. Effects of poly(L-lysine) substrates on attached *Escherichia coli* bacteria. *Langmuir*, 26(4):2639–44, 2010.

[20] H. Strahl and L. W. Hamoen. Membrane potential is important for bacterial cell division. *Proc Natl Acad Sci U S A*, 107(27):12281–6, 2010.

[21] F. Crick. Central dogma of molecular biology. *Nature*, 227(8):561–563, 1970.

[22] R. Heim, D. C. Prasher, and R. Y. Tsien. Wavelength mutations and post-translational autoxidation of green fluorescent protein. *Proc Natl Acad Sci USA*, 91(26):12501–12504, 1994.

[23] B. G. Reid and G. C. Flynn. Chromophore formation in green fluorescent protein. *Biochemistry*, 36(22):6786–6791, 1997.

[24] O. Shimomura, F. H. Johnson, and Y. Saiga. Extraction, purification and properties of aequorin, a bioluminescent protein from luminous hydromedusan, *Aequorea*. *J Cell Compar Physl*, 59(3):223–239, 1962.

[25] K. Brejc, T. K. Sixma, P. A. Kitts, S. R. Kain, R. Y. Tsien, M. Ormö, and S. J. Remington. Structural basis for dual excitation and photoisomerization of the *Aequorea victoria* green fluorescent protein. *Proc Natl Acad Sci USA*, 94:2306–2311, 1997.

[26] N. C. Shaner, P. A. Steinbach, and R. Y. Tsien. A guide to choosing fluorescent proteins. *Nat Methods*, 2(12):905–9, 2005.

[27] G. H. Patterson, S. M. Knobel, W. D. Sharif, S. R. Kain, and D. W. Piston. Use of the green fluorescent protein and its mutants in quantitative fluorescence microscopy. *Biophys J*, 73(5):2782–2790, 1997.

[28] D. J. Stephens and V. J. Allan. Light microscopy techniques for live cell imaging. *Science*, 300(5616):82–86, 2003.

[29] R. A. Hoebe, C. H. Van Oven, Jr. Gadella, T. W., P. B. Dhonukshe, C. J. Van Noorden, and E. M. Manders. Controlled light-exposure microscopy reduces photobleaching and phototoxicity in fluorescence live-cell imaging. *Nat Biotechnol*, 25(2):249–53, 2007.

[30] B. P. Cormack, R. H. Valdivia, and S. Falkow. FACS-optimized mutants of the green fluorescent protein (GFP). *Gene*, 173:33–38, 1996.

[31] T. Nagai, K. Ibata, E.S. Park, M. Kubota, K. Mikoshiba, and A. Miyawaki. A variant of yellow fluorescent protein with fast and efficient maturation for cell-biological applications. *Nat Biotechnol*, 20:87–89, 2002.

[32] M. A. Rizzo, G. H. Springer, B. Granada, and D. W. Piston. An improved cyan fluorescent protein variant useful for fret. *Nat Biotechnol*, 22(4):445–449, 2004.

[33] `http://www.microscopyu.com`. Accessed: 2016-01-08.

[34] F. Morin and J. Monod. Sur l'expression analytique de la croissance des populations bactériennes. *Rev Sci*, 80((5)):227–229, 1942.

[35] B. Görke and J. Stülke. Carbon catabolite repression in bacteria: Many ways to make the most out of nutrients. *Nat Rev Microbiol*, 6(8):613–24, 2008.

[36] U. Lendenmann, H. Senn, M. Snozzi, and T. Egli. Dynamics of mixed substrate growth of *Escherichia coli* in batch culture: The transition between simultaneous and sequential utilisation of carbon substrates. *Acta Universitatis Carolinae Environmentalica*, 14:221–30, 2000.

[37] R. Hermsen, H. Okano, C. You, N. Werner, and T. Hwa. A growth-rate composition formula for the growth of *E. coli* on co-utilized carbon substrates. *Mol Syst Biol*, 11(4):801, 2015.

[38] T. Egli. How to live at very low substrate concentration. *Water Res*, 44(17):4826–37, 2010.

[39] J. Monod. The growth of bacterial cultures. *Annu Rev Microbiol*, 3:371–394, 1949.

[40] J. Monod. *Recherches sur la Croissance des Cultures Bactériennes*. Hermann, Paris, 1941.

[41] J. Monod. Enzymatic adaptation to allosteric transitions. *Science*, 154:475–483, 1966.

[42] F. Dienert. Sur la fermentation du galactose et sur l'accoutumance des levures à ce sucre. *Ann Inst Pasteur*, 14:139–189, 1900.

[43] J. Deutscher. The mechanisms of carbon catabolite repression in bacteria. *Curr Opin Microbiol*, 11(2):87–93, 2008.

[44] U. Alon. Network motifs: theory and experimental approaches. *Nat Rev Genet*, 8(6):450–461, 2007.

[45] L. Bintu, N. E. Buchler, H. G. Garcia, U. Gerland, T. Hwa, J. Kondev, and R. Phillips. Transcriptional regulation by the numbers: Models. *Curr Opin Genet Dev*, 15(2):116–24, 2005.

[46] J. Hasty, D. McMillen, and J. J. Collins. Engineered gene circuits. *Nature*, 420(6912):224–230, 2002.

[47] E. M. Ozbudak, M. Thattai, I. Kurtser, A. D. Grossman, and A. van Oudenaarden. Regulation of noise in the expression of a single gene. *Nat Genet*, 31(1):69–73, 2002.

[48] M. B. Elowitz, A. J. Levine, E. D. Siggia, and P. S. Swain. Stochastic gene expression in a single cell. *Science*, 297(5584):1183–6, 2002.

[49] I. Lestas, G. Vinnicombe, and J. Paulsson. Fundamental limits on the suppression of molecular fluctuations. *Nature*, 467(7312):174–178, 2010.

[50] P. J. Choi, L. Cai, K. Frieda, and X. S. Xie. A stochastic single-molecule event triggers phenotype switching of a bacterial cell. *Science*, 322(5900):442–6, 2008.

[51] E. Kussell and S. Leibler. Phenotypic diversity, population growth, and information in fluctuating environments. *Science*, 309(5743):2075–8, 2005.

[52] G. Fritz. *Strategies of bacterial gene expression: regulatory mechanisms and functional aspects*. Thesis, 2012.

[53] J. R. Karr, J. C. Sanghvi, D. N. Macklin, M. V. Gutschow, J. M. Jacobs, Jr. Bolival, B., N. Assad-Garcia, J. I. Glass, and M. W. Covert. A whole-cell computational model predicts phenotype from genotype. *Cell*, 150(2):389–401, 2012.

[54] J. M. Vilar, C. C. Guet, and S. Leibler. Modeling network dynamics: The *lac* operon, a case study. *J Cell Biol*, 161(3):471–6, 2003.

[55] R. Phillips, J. Kondev, and J. Theriot. *Physical Biology of the cell*. Garland Science, Taylor & Francis Group, LLC, New York, 2009.

[56] A. Martinez-Antonio, S. C. Janga, H. Salgado, and J. Collado-Vides. Internal-sensing machinery directs the activity of the regulatory network in *Escherichia coli*. *Trends Microbiol*, 14(1):22–27, 2006.

[57] L. Gerosa and U. Sauer. Regulation and control of metabolic fluxes in microbes. *Curr Opin Biotech*, 22(4):566–575, 2011.

[58] G. Fritz, S. Dintner, N. S. Treichel, J. Radeck, U. Gerland, T. Mascher, and S. Gebhard. A new way of sensing: Need-based activation of antibiotic resistance by a flux-sensing mechanism. *mBio*, 6(4):e00975, 2015.

[59] J. W. Lichtman and J. A. Conchello. Fluorescence microscopy. *Nat Methods*, 2(12):910–919, 2005.

[60] J. C. Locke and M. B. Elowitz. Using movies to analyse gene circuit dynamics in single cells. *Nat Rev Microbiol*, 7(5):383–92, 2009.

[61] A. D. Edelstein, M. A. Tsuchida, N. Amodaj, H. Pinkard, R. D. Vale, and N. Stuurman. Advanced methods of microscope control using μManager software. *J Biol Methods*, 1(2):1–10, 2014.

[62] S. A. Westermayer, G. Fritz, J. Gutiérrez, J. A. Megerle, M. P. Weißl, K. Schnetz, U. Gerland, and J. O. Rädler. Single-cell characterization of metabolic switching in the sugar phosphotransferase system of *Escherichia coli*. *Mol Microbiol*, 100(3):472–485, 2016.

[63] H. Lange, P. Taillandier, and J.-P. Riba. Effect of high shear stress on microbial viability. *J Chem Technol Biot*, 76:501–505, 2001.

[64] S. Youssef, S. Gude, and J. O. Rädler. Automated tracking in live-cell time-lapse movies. *Integr Biol (Camb)*, 3(11):1095–101, 2011.

[65] M. A. Unger. Monolithic microfabricated valves and pumps by multilayer soft lithography. *Science*, 288(5463):113–116, 2000.

[66] P. Nghe, S. Boulineau, S. Gude, P. Recouvreux, J. S. van Zon, and S. J. Tans. Microfabricated polyacrylamide devices for the controlled culture of growing cells and developing organisms. *PLoS One*, 8(9):e75537, 2013.

[67] A. K. Marel, M. Zorn, C. Klingner, R. Wedlich-Söldner, E. Frey, and J. O. Rädler. Flow and diffusion in channel-guided cell migration. *Biophys J*, 107(5):1054–64, 2014.

[68] A. K. Marel, S. Rappl, A. Piera Alberola, and J. O. Rädler. Arraying cell cultures using PEG-DMA micromolding in standard culture dishes. *Macromol Biosci*, 13(5):595–602, 2013.

[69] D. Yankov. Diffusion of glucose and maltose in polyacrylamide gel. *Enzyme Microb Tech*, 34(6):603–610, 2004.

[70] R. S. Fischer, K. A. Myers, M. L. Gardel, and C. M. Waterman. Stiffness-controlled three-dimensional extracellular matrices for high-resolution imaging of cell behavior. *Nat Protoc*, 7(11):2056–2066, 2012.

[71] M. Gänzle and Y. Liu. Mechanisms of pressure-mediated cell death and injury in *Escherichia coli*: from fundamentals to food applications. *Front Microbiol*, 6:599, 2015.

[72] G. Fritz, J. A. Megerle, S. A. Westermayer, D. Brick, R. Heermann, K. Jung, J. O. Rädler, and U. Gerland. Single cell kinetics of phenotypic switching in the arabinose utilization system of *E. coli*. *PLoS One*, 9(2):e89532, 2014.

[73] B. Müller-Hill. *The lac operon: a short history of a genetic paradigm*. New York, 1996.

[74] R. Schleif. Regulation of the l-arabinose operon of *Escherichia coli*. *Trends Genet*, 16(12):559–565, 2000.

[75] A. Novick and M. Weiner. Enzyme induction as an all-or-none phenomenon. *Proc Natl Acad Sci USA*, 43(7):553–566, 1957.

[76] D. A. Siegele and J. C. Hu. Gene expression from plasmids containing the *araBAD* promoter at subsaturating inducer concentrations represents mixed populations. *Microbiology*, 94:8168–8172, 1997.

[77] J. Mäkelä, M. Kandhavelu, S. M. D. Oliveira, J. G. Chandraseelan, J. Lloyd-Price, J. Peltonen, O. Yli-Harja, and A. S. Ribeiro. *In vivo* single-molecule kinetics of activation and subsequent activity of the arabinose promoter. *Nucleic Acids Res*, 41(13):6544–6552, 2013.

[78] K. R. Daruwalla, A. T. Paxton, and P. J. F. Henderson. Energization of the transport-systems for arabinose and comparison with galactose transport in *Escherichia coli*. *Biochem J*, 200(3):611–627, 1981.

[79] C. M. Johnson and R. F. Schleif. In vivo induction kinetics of the arabinose promoters in *Escherichia coli*. *J Bacteriol*, 177(12):3438–3442, 1995.

[80] E. Englesberg, D. Sheppard, C. Squires, and F. Meronk. An analysis of "revertants" of a deletion mutant in C gene of L-arabinose gene complex in *Escherichia coli* B/r: Isolation of initiator constitutive mutants (I^c). *J Mol Biol*, 43(2):281–298, 1969.

[81] T. Reeder and R. Schleif. Mapping, sequence, and apparent lack of function of *araJ*, a gene of the *Escherichia coli* arabinose regulon. *J Bacteriol*, 173(24):7765–7771, 1991.

[82] S. S. Pao, I. T. Paulsen, and M. H. Saier. Major facilitator superfamily. *Microbiol Mol Biol R*, 62(1):1–+, 1998.

[83] I. M. Keseler, C. Bonavides-Martinez, J. Collado-Vides, S. Gama-Castro, M. E. Hance, J. Ingraham, S. M. Paley, I. T. Paulsen, M. Peralta-Gil, J. Pick, A. Santos-Zavaleta, and R. D. Karp. Ecocyc: A comprehensive database resource for *Escherichia coli* k12. *Abstracts of the General Meeting of the American Society for Microbiology*, 105:548–549, 2005.

[84] C. P. Novotny and E. Engelsberg. The L-arabinose permease system in *Escherichia coli*. *Biochim Biophys Acta*, 117:217–230, 1966.

[85] R. Schleif. Induction of the L-arabinose operon. *J Mol Biol*, 46:197–199, 1969.

[86] J. Y. Liu, P. F. Miller, J. Willard, and E. R. Olson. Functional and biochemical characterization of *Escherichia coli* sugar efflux transporters. *J Biol Chem*, 274(33):22977–22984, 1999.

[87] B. Müller-Hill, L. Crapo, and W. Gilbert. Mutants that make more lac repressor. *Proc Natl Acad Sci USA*, 59(4):1259–1264, 1968.

[88] J. Reizer, M. J. Novotny, C. Panos, and M. H. Saier. Mechanism of inducer expulsion in *Streptococcus pyogenes* - a two-step process activated by ATP. *J Bacteriol*, 156(1):354–361, 1983.

[89] J. T. Mettetal, D. Muzzey, J. M. Pedraza, E. M. Ozbudak, and A. van Oudenaarden. Predicting stochastic gene expression dynamics in single cells. *Proc Natl Acad Sci USA*, 103(19):7304–7309, 2006.

[90] J. W. Patrick and N. Lee. Purification and properties of an L-arabinose isomerase from *Escherichia coli*. *J Biol Chem*, 243(16):4312–4318, 1968.

[91] S. Bost, F. Silva, and D. Belin. Transcriptional activation of *ydeA*, which encodes a member of the major facilitator superfamily, interferes with arabinose accumulation and induction of the *Escherichia coli* arabinose p_{BAD} promoter. *J Bacteriol*, 181(7):2185–2191, 1999.

[92] G. J. Kremers, J. Goedhart, E. B. van Munster, and T. W. J. Gadella Jr. Cyan and yellow super fluorescent proteins with improved brightness, protein folding, and FRET Förster radius. *Biochemistry*, 45(21):6570–6580, 2006.

[93] C. Siebold, K. Flükiger, R. Beutler, and B. Erni. Carbohydrate transporters of the bacterial phophoenolpyruvate: Sugar phosphotransferase system (PTS). *FEBS Lett*, 504:104–111, 2001.

[94] J. Deutscher, F. M. Ake, M. Derkaoui, A. C. Zebre, T. N. Cao, H. Bouraoui, T. Kentache, A. Mokhtari, E. Milohanic, and P. Joyet. The bacterial phosphoenolpyruvate:carbohydrate phosphotransferase system: Regulation by protein phosphorylation and phosphorylation-dependent protein-protein interactions. *Microbiol Mol Biol R*, 78(2):231–56, 2014.

[95] P. W. Postma, J. Lengeler, and G. R. Jacobson. Phosphoenolpyruvate:carbohydrate phosphotransferase systems of bacteria. *Microbiol Rev*, 57:543–594, 1993.

[96] J. Deutscher, C. Francke, and P. W. Postma. How phosphotransferase system-related protein phosphorylation regulates carbohydrate metabolism in bacteria. *Microbiol Mol Biol R*, 70(4):939–1031, 2006.

[97] S. Neumann, K. Grosse, and V. Sourjik. Chemotactic signaling via carbohydrate phosphotransferase systems in *Escherichia coli*. *Proc Natl Acad Sci U S A*, 109(30):12159–64, 2012.

[98] M. Yamada and M. H. Jr Saier. Positive and negative regulators for glucitol (*gut*) operon expression in *Escherichia coli*. *J Mol Biol*, 203:569–583, 1988.

[99] J. Plumbridge. Repression and induction of the *nag* regulon of *Escherichia coli* k-12: The roles of *nagC* and *nagA* in maintenance of the uninduced state. *Mol Microbiol*, 5:2053–2062, 1991.

[100] J. Plumbridge and A. Kolb. DNA loop formation between Nag repressor molecules bound to its two operator sites is necessary for repression of the *nag* regulon of *Escherichia coli in vivo*. *Mol Microbiol*, 10(5):973–891, 1993.

[101] G. Löffler, P. E. Petrides, and P. C. Heinrich. *Biochemie und Pathobiochemie*. Springer-Medizin-Verlag, Heidelberg, 8. edition, 2007.

[102] Riccardo A. A. Muzzarelli, Joseph Boudrant, Diederick Meyer, Nicola Manno, Marta DeMarchis, and Maurizio G. Paoletti. Current views on fungal chitin/chitosan, human chitinases, food preservation, glucans, pectins and inulin: A tribute to henri braconnot, precursor of the carbohydrate polymers science, on the chitin bicentennial. *Carbohyd Polym*, 87(2):995–1012, 2012.

[103] B. J. Bachmann. Linkage map of *Escherichia coli* k-12, Edition 7. *Microbiol Rev*, 47(2):180–230, 1983.

[104] J. A. Plumbridge. Induction of the nag regulon of *Escherichia coli* by N-acetylglucosamine and glucosamine: Role of the cyclic AMP-catabolite activator protein complex in expression of the regulon. *J Bacteriol*, 172:2728–2735, 1990.

[105] M. J. Rogers, T. Ohgi, J. Plumbridge, and D. Soll. Nucleotide sequences of the *Escherichia coli nagE* and *nagB* genes: The structural genes for the N-acetylglucosamine transport protein of the bacterial phosphoenolpyruvate: Sugar phosphotransferase system and for glucosamine-6-phosphate deaminase. *Gene*, 62(2):197–207, 1988.

[106] M. Yamada and M. H. Saier Jr. Physical and genetic characterization of the glucitol operon in *Escherichia coli*. *J Bacteriol*, 169(7):2990–2994, 1987.

[107] J. Lengeler. Nature and properties of hexitol transport-systems in *Escherichia coli*. *J Bacteriol*, 124(1):39–47, 1975.

[108] K. McEntee. Genetic analysis of the *Escherichia coli* k-12 *srl* region. *J Bacteriol*, 132(3):904–911, 1977.

[109] J. Reizer, W. J. Mitchell, N. Minton, J. Brehm, A. Reizer, and M. H. Jr Saier. Proposed topology of the glucitol permeases of *Escherichia coli* and *Clostridium acetobutylicum*. *Curr Microbiol*, 33:331–333, 1996.

[110] T. X. Nguyen, M. R. Yen, R. D. Barabote, and M. H. Saier Jr. Topological predictions for integral membrane permeases of the phosphoenolpyruvate:sugar phosphotransferase system. *J Mol Microb Biotech*, 11(6):345–60, 2006.

[111] M. J. Novotny, J. Reizer, F. Esch, and M. H. Saier. Purification and properties of D-mannitol-1-phosphate dehydrogenase and D-glucitol-6-phosphate dehydrogenase from *Escherichia coli*. *J Bacteriol*, 159(3):986–990, 1984.

[112] C. You, H. Okano, S. Hui, Z. Zhang, M. Kim, C. W. Gunderson, Y. P. Wang, P. Lenz, D. Yan, and T. Hwa. Coordination of bacterial proteome with metabolism by cyclic AMP signalling. *Nature*, 500(7462):301–6, 2013.

[113] L. I. Alvarez-Anorve, M. L. Calcagno, and J. Plumbridge. Why does *Escherichia coli* grow more slowly on glucosamine than on N-acetylglucosamine? Effects of enzyme levels and allosteric activation of GlcN6P deaminase (NagB) on growth rates. *J Bacteriol*, 187(9):2974–82, 2005.

[114] E. I. Garvie. The growth of *Escherichia coli* in buffer substrate and distilled water. *J Bacteriol*, 69:393–398, 1955.

[115] S. Boulineau, F. Tostevin, D. J. Kiviet, P. R. ten Wolde, P. Nghe, and S. J. Tans. Single-cell dynamics reveals sustained growth during diauxic shifts. *PLoS One*, 8(4):e61686, 2013.

[116] K. G. Peri and E. B. Waygood. Sequence of cloned enzyme $II^{N-acetylglucosamine}$ of the phosphoenolpyruvate:N-acetylglucosamine phosphotransferase system of *Escherichia coli*. *Biochemistry*, 27(16):6054–61, 1988.

[117] R L. M. van Montfort, T. Pijning, K. H. Kalk, I. Hangyi, M. L. C. E. Kouwijzer, G. T. Robillard, and B. W. Dijkstra. The structure of the *Escherichia coli* phosphotransferase $IIA^{mannitol}$ reveals a novel fold with two conformations of the active site. *Curr Biol*, 6:377–388, 1998.

[118] B. M. Hogema, J. C. Arents, R. Bader, K. Eijkemans, H. Yoshida, H. Takahashi, H. Alba, and P. W. Postma. Inducer exclusion in *Escherichia coli* by non-PTS substrates: The role of the PEP to pyruvate ratio in determining the phosphorylation state of enzyme IIA^{Glc}. *Mol Microbiol*, 30(3):487–498, 1998.

[119] K. Bettenbrock, S. Fischer, A. Kremling, K. Jahreis, T. Sauter, and E. D. Gilles. A quantitative approach to catabolite repression in *Escherichia coli*. *J Biol Chem*, 281(5):2578–84, 2006.

[120] A. Kremling, S. Fischer, T. Sauter, K. Bettenbrock, and E. D. Gilles. Time hierarchies in the *Escherichia coli* carbohydrate uptake and metabolism. *Biosystems*, 73(1):57–71, 2004.

[121] T. Egli, U. Lendenmann, and M. Snozzi. Kinetics of microbial growth with mixtures of carbon sources. *Antonie van Leeuwenhoek*, 63:289–298, 1993.

[122] G. Aidelberg, B. D. Towbin, D. Rothschild, E. Dekel, A. Bren, and U. Alon. Hierarchy of non-glucose sugars in *Escherichia coli*. *BMC Syst Biol*, 8(1):1, 2014.

[123] T. Ferenci. Hungry bacteria - definition and properties of a nutritional state. *Environ Microbiol*, 3(10):605–611, 2001.

[124] S. Waldherr, D. A. Oyarzun, and A. Bockmayr. Dynamic optimization of metabolic networks coupled with gene expression. *J Theor Biol*, 365:469–85, 2015.

[125] G. Lambert and E. Kussell. Memory and fitness optimization of bacteria under fluctuating environments. *PloS One Genetics*, 10(9):e1004556, 2014.

[126] D. Groff, P. I. Benke, T. S. Batth, G. Bokinsky, C. J. Petzold, P. D. Adams, and J. D. Keasling. Supplementation of intracellular XylR leads to coutilization of hemicellulose sugars. *Appl Environ Microbiol*, 78(7):2221–2229, 2012.

[127] A. A. Toymentseva, K. Schrecke, M. R. Sharipova, and T. Mascher. The LIKE system, a novel protein expression toolbox for *Bacillus subtilis* based on the *liaI* promoter. *Microb Cell Fact*, 11, 2012.

[128] K. A. Datsenko and B. L. Wanner. One-step inactivation of chromosomal genes in *Escherichia coli* k-12 using PCR products. *Proc Natl Acad Sci USA*, 97(12):6640–6645, 2000.

[129] P. O. Olins and S. H. Rangwala. A novel sequence element derived from bacteriophage T7 mRNA acts as an enhancer of translation of the *lacZ* gene in *Escherichia coli*. *J Biol Chem*, 264(29):16973–16976, 1989.

[130] C. D. Smolke, T. A. Carrier, and J. D. Keasling. Coordinated, differential expression of two genes through directed mRNA cleavage and stabilization by secondary structures. *Appl Environ Microbiol*, 66(12):5399–5405, 2000.

[131] M. Thattai and A. van Oudenaarden. Intrinsic noise in gene regulatory networks. *Proc Natl Acad Sci USA*, 98(15):8614–8619, 2001.

[132] J. H. Miller. *Experiments in molecular genetics*. Experiments in Molecular Genetics. 1972.

Ein herzliches Dankeschön an ...

Prof. Dr. Joachim Rädler, meinen Doktorvater, für die Unterstützung und Förderung während dieser Arbeit. Dir ist es immer wieder gelungen meinen Blick auf den Gesamtzusammenhang zu lenken, wenn ich Gefahr lief ihn in Details vertieft aus den Augen zu verlieren. Danke auch für die Möglichkeit sehr selbständig zu arbeiten, mit allen damit verbundenen Freiheiten.

Prof. Dr. Ulrich Gerland, für die wichtige Betreuung dieser Arbeit von theoretischer Seite, insbesondere für die Unterstützung meines Masterstudenten Joaquín sowie dafür, dass du stets Zeit für meine Fragen gefunden hast.
Prof. Dr. Karin Schnetz und **Prof. Dr. Kirsten Jung** für hilfreiche Diskussionen zu den biologischen Fragestellungen dieser Arbeit sowie für die Herstellung zahlreicher Mutanten.
Dr. Judith Megerle für die hervorragende Projektübergabe und Betreuung in meine Selbständigkeit hinein.
Dr. Georg Fritz für wesentliche Beiträge von theoretischer Seite. Herzlichen Dank auch besonders für deine motivierende Führung auf dem Weg durch die "paper-Wüste".
Dr. Madeleine Leisner für das Wissen um eine offene Tür und so manche freundliche Hilfe.

Joaquín Gutiérrez für die große Bereicherung meiner Arbeit im Rahmen seiner Masterarbeit. Vielen Dank auch an **Laura Lechtenberg, Mira Weißl und Merlin Klotz**, die durch ihre Bachelorarbeiten alle einen wichtigen Beitrag geleistet haben.
Andreas Mader und die ganze Crew aus dem Mikrobiologie Labor für ein gut organisiertes Labor, in dem das Arbeiten selbst an vollen Tagen immer Spaß gemacht hat.
Sara Kesel außerdem für gesprächsreiche Bewegung an kalten Tagen zum Heißgetränk unserer Wahl.

Margarete Meixner, Andrea Cooke, Gerlinde Schwake, Max Albert, Susanne Kempter und Charlott Leu dafür, dass sie alle den Lehrstuhl am Laufen halten und ich mich bei diversen organisatorischen oder technischen Problemen immer an sie wenden konnte. **Susanne Rappl** noch einen besonderen Dank für die Mikrostrukturierungsarbeit mit Laura im Reinraum.

mein altes Büro, ich habe die Zeit der lebhaften Diskussionen, der roten Karten und des Spruchs des Tages mit euch sehr genossen. Einen besonderen Dank an **Tobias Preiß**, den amtierenden Büromethusalem, für deine unglaubliche Hilfsbereitschaft und stets freundschaftliche Geduld bei allen praktischen Problemen.
mein neues Büro für die angenehme und produktive Arbeitsathmosphäre mit einem guten Schuß anregender Diskussionen. **Felix Segerer** für deine konstruktive Kritik bei Bilderfragen, witzig und charmant, immer verknüpft mit qualifizierter Hilfe bei (fast) allen Herausforderungen, die der Illustrator so bietet.
alle Mitglieder des LS Rädler für ein äußerst positives Arbeitsklima, zahllose freundliche Worte auf den Gängen und gemeinsame teambildende Aktivitäten.

alle Damen (und Herren) der Aktiven Pause, insbesondere den Versuchskaninchen der ersten Stunde. Das motivierende, gemeinsame Training mit euch hat mich auf die Trainerlaufbahn gebracht. Hier auch noch einen speziellen Dank an Joachim für seine wohlwollende Haltung der Aktiven Pause gegenüber und dem **CeNS Team** für die Beherbergung in ihrem Seminarraum an dachterrassenungeeigneten Tagen. **Luisa Kneer** nicht nur für unzählige, lebendige Mittagspausen. Es ist schön, dass du den Weg an den Lehrstuhl gefunden hast. Für einen gruppenübergreifenden Austausch Dank auch den gesamten **Rennrädlern**, allen voran den humorvollen Kapitänen **Carolin Leonhardt** und **Stefan Fischer**. Mit euch läuft es sich auch lachend durch den Regen.
alle kritischen Korrekturleser (Carolin, Svenja, Sara, Mirjam, Marianne, Peter und Barbara).

meine Freunde und meine Familie für euren Rückhalt in allen Lebenslagen. Ich bin glücklich, dass ich euch habe!